ISSN
2395-6992

International Journal of Engineering Research & Science

www.ijoer.com
www.adpublications.org

Volume-4! Issue-6! June, 2018 www.ijoer.com ! info@ijoer.com

Preface

We would like to present, with great pleasure, the inaugural volume-4, Issue-6, June 2018, of a scholarly journal, *International Journal of Engineering Research & Science*. This journal is part of the AD Publications series *in the field of Engineering, Mathematics, Physics, Chemistry and science Research Development*, and is devoted to the gamut of Engineering and Science issues, from theoretical aspects to application-dependent studies and the validation of emerging technologies.

This journal was envisioned and founded to represent the growing needs of Engineering and Science as an emerging and increasingly vital field, now widely recognized as an integral part of scientific and technical investigations. Its mission is to become a voice of the Engineering and Science community, addressing researchers and practitioners in below areas

Chemical Engineering	
Biomolecular Engineering	Materials Engineering
Molecular Engineering	Process Engineering
Corrosion Engineering	
Civil Engineering	
Environmental Engineering	Geotechnical Engineering
Structural Engineering	Mining Engineering
Transport Engineering	Water resources Engineering
Electrical Engineering	
Power System Engineering	Optical Engineering
Mechanical Engineering	
Acoustical Engineering	Manufacturing Engineering
Optomechanical Engineering	Thermal Engineering
Power plant Engineering	Energy Engineering
Sports Engineering	Vehicle Engineering
Software Engineering	
Computer-aided Engineering	Cryptographic Engineering
Teletraffic Engineering	Web Engineering
System Engineering	
Mathematics	
Arithmetic	Algebra
Number theory	Field theory and polynomials
Analysis	Combinatorics
Geometry and topology	Topology
Probability and Statistics	Computational Science
Physical Science	Operational Research
Physics	
Nuclear and particle physics	Atomic, molecular, and optical physics
Condensed matter physics	Astrophysics
Applied Physics	Modern physics
Philosophy	Core theories

Chemistry	
Analytical chemistry	Biochemistry
Inorganic chemistry	Materials chemistry
Neurochemistry	Nuclear chemistry
Organic chemistry	Physical chemistry
Other Engineering Areas	
Aerospace Engineering	Agricultural Engineering
Applied Engineering	Biomedical Engineering
Biological Engineering	Building services Engineering
Energy Engineering	Railway Engineering
Industrial Engineering	Mechatronics Engineering
Management Engineering	Military Engineering
Petroleum Engineering	Nuclear Engineering
Textile Engineering	Nano Engineering
Algorithm and Computational Complexity	Artificial Intelligence
Electronics & Communication Engineering	Image Processing
Information Retrieval	Low Power VLSI Design
Neural Networks	Plastic Engineering

Each article in this issue provides an example of a concrete industrial application or a case study of the presented methodology to amplify the impact of the contribution. We are very thankful to everybody within that community who supported the idea of creating a new Research with IJOER. We are certain that this issue will be followed by many others, reporting new developments in the Engineering and Science field. This issue would not have been possible without the great support of the Reviewer, Editorial Board members and also with our Advisory Board Members, and we would like to express our sincere thanks to all of them. We would also like to express our gratitude to the editorial staff of AD Publications, who supported us at every stage of the project. It is our hope that this fine collection of articles will be a valuable resource for *IJOER* readers and will stimulate further research into the vibrant area of Engineering and Science Research.

Mukesh Arora

(Chief Editor)

Board Members

Dr. S.R.Boselin Prabhu

Ph.D, Wireless Sensor Networks, M.E. Network Engineering, Excellent Professional Achievement Award Winner from Society of Professional Engineers Biography Included in Marquis Who's Who in the World (Academic Year 2015 and 2016). Currently Serving as Assistant Professor in the department of ECE in SVS College of Engineering, Coimbatore.

Dr. Maheshwar Shrestha

Postdoctoral Research Fellow in DEPT. OF ELE ENGG & COMP SCI, SDSU, Brookings, SD Ph.D, M.Sc. in Electrical Engineering from SOUTH DAKOTA STATE UNIVERSITY, Brookings, SD.

Zairi Ismael Rizman

Senior Lecturer, Faculty of Electrical Engineering, Universiti Teknologi MARA (UiTM) (Terengganu) Malaysia Master (Science) in Microelectronics (2005), Universiti Kebangsaan Malaysia (UKM), Malaysia. Bachelor (Hons.) and Diploma in Electrical Engineering (Communication) (2002), UiTM Shah Alam, Malaysia

Dr. D. Amaranatha Reddy

Ph.D.(Postdocteral Fellow,Pusan National University, South Korea), M.Sc., B.Sc. : Physics.

Dr. Dibya Prakash Rai

Post Doctoral Fellow (PDF), M.Sc.,B.Sc., Working as Assistant Professor in Department of Physics in Pachhuncga University College, Mizoram, India.

Dr. Pankaj Kumar Pal

Ph.D R/S, ECE Deptt., IIT-Roorkee.

Dr. P. Thangam

BE(Computer Hardware & Software), ME(CSE), PhD in Information & Communication Engineering, currently serving as Associate Professor in the Department of Computer Science and Engineering of Coimbatore Institute of Engineering and Technology.

Dr. Pradeep K. Sharma

PhD., M.Phil, M.Sc, B.Sc, in Physics, MBA in System Management, Presently working as Provost and Associate Professor & Head of Department for Physics in University of Engineering & Management, Jaipur.

Dr. R. Devi Priya

Ph.D (CSE),Anna University Chennai in 2013, M.E, B.E (CSE) from Kongu Engineering College, currently working in the Department of Computer Science and Engineering in Kongu Engineering College, Tamil Nadu, India.

Dr. Sandeep

Post-doctoral fellow, Principal Investigator, Young Scientist Scheme Project (DST-SERB), Department of Physics, Mizoram University, Aizawl Mizoram, India- 796001.

Mr. Abilash

MTech in VLSI, BTech in Electronics & Telecommunication engineering through A.M.I.E.T.E from Central Electronics Engineering Research Institute (C.E.E.R.I) Pilani, Industrial Electronics from ATI-EPI Hyderabad, IEEE course in Mechatronics, CSHAM from Birla Institute Of Professional Studies.

Mr. Varun Shukla

M.Tech in ECE from RGPV (Awarded with silver Medal By President of India), Assistant Professor, Dept. of ECE, PSIT, Kanpur.

Mr. Shrikant Harle

Presently working as a Assistant Professor in Civil Engineering field of Prof. Ram Meghe College of Engineering and Management, Amravati. He was Senior Design Engineer (Larsen & Toubro Limited, India).

Table of Contents

Numerical Treatment of the Stochastic Advection-Diffusion Equation Using the Spectral Stochastic Techniques

Maha hamed[1], I. L. El-Kalla[2], Beih. S. El-desouky[3], Mohamed A. El-Beltagy[4]

[1,3]Department of Mathematics, faculty of science, Mansoura university, Mansoura , Egypt
[2]Department of Engineering Mathematics & Physics, Faculty of Engineering, Mansoura University, Egypt
[4]Department of Engineering Mathematics & Physics, Faculty of Engineering, Cairo University, Giza, Egypt

Abstract— *Stochastic advection diffusion equation (SADE) with multiplicative stochastic input is a practical mathematical model for different physical phenomena. In this paper, SADE will be studied using two spectral stochastic techniques. The first is the Wiener chaos expansion (WCE) technique and the second is the Wiener-Hermite expansion with perturbation (WHEP) technique. These techniques convert the SADE into a system of deterministic partial differential equation (DPDE) that can be solved using a deterministic numerical method which is suitable for the periodic boundary conditions. Convergence analysis is discussed and some of the second order moments are compared. The numerical results demonstrate the efficiency of both techniques. The WCE technique is more accuracy than the WHEP technique. The diffusion and advection coefficient and the intensity of Gaussian white noise play important roles in the SADE solution. The study shows that the WCE technique is more practical to get the closed form mean solution while the WHEP technique gets the mean solution in the form of an infinite series.*

Keywords— Advection diffusion equation, Multiplicative random input, Wiener-Hermite expansion, Wiener-Chaos expansion, Periodic boundary conditions.

I. INTRODUCTION

Numerical models have received a great attention in sciences and engineering in the recent years for modeling the differential equations. These models work on reducing the cost and time of computation especially for the physical phenomena that contain uncertain input. This phenomena can be studied by converting it into mathematical models of stochastic differential equations (SDE) and we can use the numerical methods [1,2] for overcoming these problems.

Numerical methods have been developed for simulating SDE such as moment equations, probability density method [3], etc. These methods are complicated in solving the nonlinear SDEs so the spectral decomposition techniques have received much attention in the recent years. The spectral decomposition technique was first suggested by the great mathematician Norbert Wiener [4]. Wiener constructed an orthonormal random basis for expanding homogeneous chaos depending on white noise, and used it to study problems in statistical mechanics [5]. The Hermite polynomial has been used to obtain the solution of SDE. Mecham et al. [6] suggested the Wiener-Hermite expansion to study turbulence solution of Burger equation. In nonlinear stochastic differential equations, there exist always difficulties of solving the resultant set of deterministic integro-differential equations. The deterministic integro-differential equations got from the applications of a set of comprehensive averages on the stochastic integro-differential equation obtained after the direct application of WHE. Many authors introduced different methods to face these obstacles. Among them, the WHEP technique [7] was introduced using the perturbation technique to solve perturbed nonlinear problems. M. El-Tawil and his co-workers [7-11] used the WHE together with the perturbation theory (WHEP technique) to solve a perturbed nonlinear stochastic differential equation. The WHEP technique is generalized to handle n^{th} order polynomial nonlinearities, general order of WHE and general number of corrections [8].

Cameron and martin [12] was developed a more explicit and intuitive formulation for the Hermite polynomial, which was called the Wiener-Chaos expansion. Their development is based on an explicit discretization of the white noise process through its Fourier expansion. This approach is much easier to understand and more convenient to use, and hence replaced Wiener's original formulation. Fourier chaos expansion has become a useful tool in stochastic analysis involving Brownian motion [13]. Rozovskii et al. [14-16] derived Wiener chaos propagator equations for several important the stochastic partial differential equations (SPDEs) driven by Brownian motion forcing. Lototsky et al. [17, 18] proposed a new numerical method for solving the Zakai equation based on its Wiener chaos expansion. Using Fourier-Hermite expansion for modeling non-Gaussian processes is also investigated [19, 20]. Babuska et al. [21], Schwab et al. [22] and Keese el al. [23] developed

and generalized Ghanem's approach for solving stochastic elliptic equations. Xiu and Karniadakis [24] generalized the Hermite polynomial expansion and used it to study flow-structure interactions. Zhang et al. [25] combined moment perturbation method with polynomial chaos expansion, and used it to study the saturation flows in heterogeneous porous media.

The main goal of this paper is to use two stochastic spectral techniques, WCE and WHEP for solving the stochastic advection diffusion equation with multiplicative white noise and periodic boundary conditions. The two techniques convert SPDE into a system of DPDE. The DPDE can be solved using a proposed Eigen function expansion in both cases of WCE and WHEP techniques. The results will be studied through the mean and variance solutions.

This paper is organized as follows:

The formulation of the SADE is outlined in section 2. The WCE technique is explained in section 3. In section 4, the algorithm of WHEP technique is introduced. In section 5 and 6, we apply the WCE and WHEP techniques respectively; the convergence analysis of the WCE is studied. The proposed method for solving the resulting DPDEs; the numerical solutions of the WCE and WHEP techniques are introduced in section 7. The comparison and discussion of the results of the two techniques are in section 8. Finally, the conclusions are given in Section 9.

II. STOCHASTIC ADVECTION DIFFUSION EQUATION

SADE represents the transporting that occurs in fluids through the combination of advection process and diffusion process .Consider the SADE in Stratonovich sense with multiplicative stochastic force described by white noise and periodic boundary conditions as [27]:

$$\begin{aligned} &du(x,t) = \mu \frac{\partial^2}{\partial x^2} u(x,t)dt + \sigma \frac{\partial}{\partial x} u(x,t) \circ dW_t, \quad t > 0, \\ &u(0,x) = \sin(x), \quad x \in (0, 2\pi), \end{aligned} \tag{2.1}$$

which can be written in the Ito sense as:

$$\begin{aligned} &du(x,t) = \gamma \frac{\partial^2}{\partial x^2} u(x,t)dt + \sigma \frac{\partial}{\partial x} u(x,t)dW_t, \quad t > 0, \\ &u(0,x) = \sin(x), \quad x \in (0, 2\pi), \end{aligned} \tag{2.2}$$

where $u(x,t)$ represents the concentration of mass transfer; $\mu \geq 0$ represents the diffusion coefficient; $\sigma > 0$, $\gamma = \mu + \frac{\sigma^2}{2}$ and W_t is the one dimensional Brownian motion.

This model has exact solution [27] as:

$$u(x,t) = e^{-\mu t} \sin(x + \sigma W(t)). \tag{2.3}$$

The first order moment $E[u(x,t)]$ and the second order moment $E[u(x,t)]^2$ are:

$$\begin{aligned} &E[u(x,t)] = e^{-\gamma t} \sin(x), \\ &E[u(x,t)]^2 = e^{-2\mu t} \left(\frac{1}{2} - \frac{1}{2} e^{-2\sigma^2 t} \cos(2x) \right), \end{aligned} \tag{2.4}$$

So the solution admits the Wiener chaos expansion because of finite second moment.

III. WIENER CHAOS EXPANSION TECHNIQUE

For SPDE with random force in form of Brownian motion (BM) and for fixed time $T > 0$, we consider an orthnormal basis in Hilbert space $L^2([0,T])$ to be the trigonometric functions [16]:

$$m_1(t)=\sqrt{\frac{1}{T}},\quad m_i(t)=\sqrt{\frac{2}{T}}\cos\left(\frac{(i-1)\pi t}{T}\right),\quad i>1,\ 0\le t\le T.$$

Also define the standard Gaussian random variables ζ_i (GRVs) and the Brownian motion $W_t=W(t)$ as follows:

$$\zeta_i=\int_0^t m_i(s)dW_S,\qquad W(t)=\sum_{i=1}^{\infty}\zeta_i\int_0^t m_i(s)ds. \tag{3.1}$$

The convergence in mean square sense [26] in the interval $[0,T]$ is:

$$E[W(t)-\sum_{i=1}^{N}\zeta_i\int_0^t m_i(\tau)d\tau]^2<\frac{T}{\pi N},\quad 0\le t\le T\ .$$

According to [12], the solution function $u(x,t)$ can be expanded as follows:

$$u(x,t)=\sum_{\alpha\in\Im}u_\alpha(x,t)T_\alpha(\zeta),\quad u_\alpha=E[uT_\alpha(\zeta)]=E[uT_\alpha(t)], \tag{3.2}$$

where the multi-indices $\Im=\{\alpha=(\alpha_i,i\ge1),\ \alpha_i\in\{0,1,2,...\};|\alpha|=\sum_{i=1}^{\infty}\alpha_i<\infty\}$ and $T_\alpha(\zeta)=\prod_{i=1}^{\infty}H_{\alpha_i}(\zeta_i)$ where $H_n(x)$ is the normalized n^{th} order Hermite polynomial and T_α are called Wick polynomials of order α. Also $T_\alpha(t)$ is the Wick polynomials filtered by the σ-algebra F_t^W, Recall that $T_\alpha(t)$ is a martingale and satisfies the differential equation [26]:

$$dT_\alpha(t)=\sum_{i\ge1}\sqrt{\alpha_i}m_i(t)T_{\bar\alpha(i)}\,dW_t, \tag{3.3}$$

where multi-index $\bar\alpha_i(j)=\begin{cases}\alpha_j, & j\ne i,\\ \alpha_{i-1}, & j=i.\end{cases}$.

Wick polynomials form a complete orthonormal basis in the Hilbet space. The expectation of two wich polynomials T_α,T_β is $E[T_\alpha T_\beta]=\delta_{\alpha,\beta}$.

Truncating the expansion (3.2) up to polynomial of order N and using only K GRVs retains $\frac{(K+N)!}{N!(K)!}$ coefficients [26].

The truncated multi-indices will be $\Im_{K,N}=\{\alpha=(\alpha_1,\dots\alpha_K),\ \alpha_i\in\{0,1,2,...\};|\alpha|=\sum_{i=1}^{K}\alpha_i\le N\}$. Then the truncated WCE can be denoted as:

$$u_{K,N}(x,t)=\sum_{\alpha\in\Im_{K,N}}u_\alpha(x,t)T_\alpha(\zeta). \tag{3.4}$$

The mean and variance of the truncate solution function $u_{K,N}(x,t)$ are computed as:

$$E[u_{K,N}(x,t;\omega)]=u_0(x,t),$$

$$\mathrm{var}[u_{K,N}(x,t;\omega)]=\sum_{\alpha\in\Im_{K,N},\alpha\ne0}|u_\alpha(x,t)|^2.$$

IV. WIENER HERMITE EXPANSION

As a consequence of the completeness of the Wiener-Hermite set [28] any arbitrary stochastic process can be expanded in terms of the Wiener-Hermite polynomial set $H^{(n)}(t_1,...,t_n)$. This expansion converges to the original stochastic process with probability one.

The stochastic solution process $u(x,t;w)$ can be expanded as, [7]:

$$u(x,t;\omega) = u^{(0)}(x,t) + \sum_{k=1}^{\infty} \int_{R^k} u^{(k)}(x,t;t_1,...,t_k) H^{(k)}(t_1,...,t_k)\, d\tau_k , \tag{4.1}$$

where $d\tau_k = dt_1 dt_2 .... dt_k$ and $\int_{R^k}$ is a *k*-dimensional integral over the disposable variables $t_1, t_2, ..., t_k$. The functional $H^{(n)}(t_1, t_2, ...t_n)$ is the nth order Wiener-Hermite time independent functional and $u^{(i)}(x,t;t_1,t_2,...t_i);\ i \geq 0$ are the deterministic kernel of the WHE.

The Wiener-Hermite functionals $H^{(n)}$ form a complete set with $H^{(0)} = 1$ and $H^{(1)}(t) = \dfrac{dW}{dt}$ is the white noise. The $H^{(n)}$ functions are statistically orthnormal, i.e.

$$\begin{aligned} &E\left[H^{(i)} \right] = 0 \quad \forall\, i \geq 1, \\ &E\left[H^{(i)} H^{(j)} \right] = 0 \quad \forall i \neq j. \end{aligned} \tag{4.2}$$

The solution will be practically truncated with $(m+1)$ terms and the expectation and variance of the truncated solution will be:

$$\begin{aligned} &E[u(x,t;\omega)] = u^{(0)}(x,t), \\ &\text{var}[u(x,t;\omega)] = \sum_{k=1}^{m} k! \int_{R^k} \left(u^{(k)}(x,t;t_1,...,t_k) \right)^2 d\tau_k . \end{aligned}$$

In the nonlinear SPDE or the multiplicative SPDE, it is difficult to solve the deterministic differential-integral equation system of the kernels results from the application of the WHE. This difficulty is due to the resulting system is a coupled differential-integral system and we can overcome this by using the perturbation technique.

In the perturbation technique the solution is a power series of small parameter σ. Set of simple equations are expanded as [29]:

$$u^{(k)} = \sum_{i=0}^{NC} \sigma^i u_i^{(k)},\ k \geq 0, \tag{4.3}$$

where NC is the number of corrections. For m order WHE, the statistical properties of the relatively solution will be calculated as:

$$\begin{aligned} &E[u(x,t;\omega)] = \sum_{i=0}^{NC} \sigma^i u_i^{(0)}(x,t), \\ &\text{var}[u(x,t;\omega)] = \sum_{k=1}^{m} k! \int_{R^k} \left(\sum_{i=0}^{NC} \sigma^i u_i^{(k)}(x,t;t_1,...,t_k) \right)^2 d\tau_k . \end{aligned} \tag{4.4}$$

V. APPLICATION OF WCE

To get the WCE of SADE (2.2); consider the differential form:

$$d[uT_\alpha] = du.T_\alpha + u.dT_\alpha + du.dT_\alpha,$$

using equations (2.2) and (3.3) to get:

$$\begin{aligned} d[uT_\alpha] = &\left(\gamma \frac{\partial^2}{\partial x^2} u(x,t)dt + \sigma \frac{\partial}{\partial x} u(x,t)dW_t \right) T_\alpha + u\left(\sum_{i\geq 1} \sqrt{\alpha_i}\, m_i(t) T_{\overline{\alpha(i)}}\, dW_t \right) + \\ &\left(\gamma \frac{\partial^2}{\partial x^2} u(x,t)dt + \sigma \frac{\partial}{\partial x} u(x,t)dW_t \right).\left(\sum_{i\geq 1} \sqrt{\alpha_i}\, m_i(t) T_{\overline{\alpha(i)}}\, dW_t \right). \end{aligned} \tag{5.1}$$

Taking the expectation for both sides of (5.1), the terms involving Ito integrals will disappear since they are mean zero. Then we will get,

$$d[u_\alpha(x,t)] = \left(\gamma \frac{\partial^2}{\partial x^2} u_\alpha(x,t)dt \right) + \sigma \left(\sum_{i\geq 1} \sqrt{\alpha_i}\, m_i(t) \frac{\partial}{\partial x} u_{\overline{\alpha(i)}}(x,t) \right), \tag{5.2}$$

with the initial condition $u_\alpha(x,0) = \begin{cases} \sin(x), & \alpha=0, \\ 0, & \alpha\neq 0. \end{cases}$.

Theorem:

The SADE (2.1) which has exact solution $u(x,t)$ and the truncated solution $u_{K,N}(x,t)$; the estimated error will take the form:

$$E\left|u(x,t) - u_{K,N}(x,t)\right| \leq Ce^{-\mu t}\left(\frac{\sigma T}{K} + \frac{(\sigma\, T)^{N+1}}{(N+1)!}\right).$$

Proof:

according to [27], since $u(x,t) = \theta(x+\sigma W(t),t)$, and $W(t) = \sum_{i=1}^{\infty} \zeta_i \int_0^t m_i(s)ds = \frac{t}{\sqrt{T}}\zeta_1 + \sum_{i=2}^{\infty} \zeta_i \frac{\sqrt{2T}}{(i-1)\pi} \sin\left(\frac{(i-1)\pi t}{T}\right)$, let

$W(t) = W_K + W_S,$

$W_K = \frac{t}{\sqrt{T}}\zeta_1 + \sum_{i=2}^{K} \zeta_i \frac{\sqrt{2T}}{(i-1)\pi} \sin\left(\frac{(i-1)\pi t}{T}\right)$ and $W_S = \sum_{i=K+1}^{\infty} \zeta_i \frac{\sqrt{2T}}{(i-1)\pi} \sin\left(\frac{(i-1)\pi t}{T}\right)$ where W_K and W_S are orthogonal. After that we can expand the solution $\theta(x+\sigma W_K + \sigma W_S, t)$ by Taylor's series with respect to W_K and W_S respectively, to get:

$$u(x,t) = \theta(x,t) + \sum_{m=1}^{N} \frac{(\sigma W_K)^m}{m!} \frac{\partial^m}{\partial x^m}\theta(x,t) + \frac{\partial}{\partial x}\theta(x+\sigma W_K + \eta_1, t)\sigma w_S + \frac{(\sigma W_K)^{N+1}}{(\mathrm{N}+1)!} \frac{\partial^{N+1}}{\partial x^{N+1}}\theta(x+\eta_2, t).$$

Truncating the solution with respect to order N and K GRVs to get:

$$u_{K,N}(x,t) = \theta(x,t) + \sum_{m=1}^{N} \frac{(\sigma W_K)^m}{m!} \frac{\partial^m}{\partial x}\theta(x,t),$$

then we have $E\left|u(x,t) - u_{K,N}(x,t)\right| \leq C_1 \sigma E\left|W_S^2\right| + C_{N+1} \frac{\sigma^{N+1}}{(N+1)!} E\left|W_K^{2N+2}\right|,$

where $C_n = \sup_x \left|\frac{\partial}{\partial x}\theta(x,t)\right|,$

then $E\left|W_S^2\right| \le \frac{2T}{\pi^2}\sum_{i=K+1}^{\infty}\frac{1}{(K-1)^2}\sin^2(\frac{(i-1)\pi t}{T}) < \frac{2T}{\pi^2 K}$,

$E\left|W_K^{2N+2}\right| = (E\left|W_K^2\right|)^{N+1}(2N+1)!! < (E\left|W^2\right|)^{N+1}(2N+1)!!$,

where $(2N+1)!! = (2N+1)(2N-1).....1$,

then,

$$E\left|u(x,t)-u_{K,N}(x,t)\right| \le Ce^{-\mu t}(\frac{\sigma T}{K}+\frac{(\sigma\ T)^{N+1}}{(N+1)!}). \tag{5.3}$$

This means that, the error between the approximate solution and the exact solution decays by increasing the number K of GRVs, the order of polynomial chaos N and diffusion coefficient μ. Also decreasing the advection coefficient σ and the time interval T increases the convergence between the exact and the WCE approximation.

VI. APPLICATION OF WHE

The first two terms in expansion (4.1) are the Gaussian part of the solution. This part is not sufficient for the accurate solution of SADE. The second order WHE is applied to the SADE (2.2) to get:

$$\frac{\partial}{\partial t}u^{(0)}(x,t)+\int_0^t\frac{\partial}{\partial t}u^{(1)}(x,t;t_1)H^{(1)}(t_1)dt_1+\int_0^t\int_0^t\frac{\partial}{\partial t}u^{(2)}(x,t;t_1,t_2)H^{(2)}(t_1,t_2)dt_1dt_2 =$$
$$\gamma\left[\frac{\partial^2}{\partial x^2}u^{(0)}(x,t)+\int_0^t\frac{\partial^2}{\partial x^2}u^{(1)}(x,t;t_1)H^{(1)}(t_1)dt_1+\int_0^t\int_0^t\frac{\partial^2}{\partial x^2}u^{(2)}(x,t;t_1,t_2)H^{(2)}(t_1,t_2)dt_1dt_2\right]+$$
$$\sigma n(t)\left[\frac{\partial}{\partial x}u^{(0)}(x,t)+\int_0^t\frac{\partial}{\partial x}u^{(1)}(x,t;t_1)H^{(1)}(t_1)dt_1+\int_0^t\int_0^t\frac{\partial}{\partial x}u^{(2)}(x,t;t_1,t_2)H^{(2)}(t_1,t_2)dt_1dt_2\right],$$
$$u^{(0)}(x,0)=\sin(x),\ u^{(1)}(x,0;t_1)=u^{(2)}(x,0;t_1,t_2)=0. \tag{6.1}$$

Multiplying both sides of (6.1) with $H^{(0)}, H^{(1)}(t_1)$ and $H^{(2)}(t_1,t_2)$ respectively and taking the expectation to get:

$$\frac{\partial}{\partial t}u^{(0)}(x,t)=\gamma\frac{\partial^2}{\partial x^2}u^{(0)}(x,t)+\sigma\frac{\partial}{\partial x}u^{(1)}(x,t;t). \tag{6.2}$$

$$\frac{\partial}{\partial t}u^{(1)}(x,t;t_1)=\gamma\frac{\partial^2}{\partial x^2}u^{(1)}(x,t;t_1)+\sigma\frac{\partial}{\partial x}u^{(0)}(x,t)\delta(t-t_1)+2\sigma\frac{\partial}{\partial x}u^{(2)}(x,t;t,t_1). \tag{6.3}$$

$$\frac{\partial}{\partial t}u^{(2)}(x,t;t_1,t_2)=\gamma\frac{\partial^2}{\partial x^2}u^{(2)}(x,t;t_1,t_2)+\frac{1}{2}\sigma\frac{\partial}{\partial x}u^{(1)}(x,t;t_1)\delta(t-t_2)+\frac{1}{2}\sigma\frac{\partial}{\partial x}u^{(1)}(x,t;t_2)\delta(t-t_1). \tag{6.4}$$

The deterministic systems appear when applying WCE and WHE are coupled integro-differential system of equations that are not easy to solve. In the following section, we will suggest a numerical technique to solve the deterministic systems (5.2) and (6.2-6.4) with periodic boundary conditions.

VII. THE NUMERICAL TECHNIQUE USING THE PRINCIPAL OF EIGEN FUNCTION EXPANSION

We introduce a numerical technique for solving the DPDE resulting from the application of the WCE and WHEP techniques. Here we implement the usual Eigen function [30] to be suitable for solving the resulting system of differential equations with periodic boundary conditions. The solution $u(x,t)$ can be written as an Eigen function expansion as:

$$u(x,t)=\sum_{n=0}^{\infty}\left[C_n^1 e^{-an^2t}+\int_0^t e^{-an^2(t-s)}F_n^1(s)\,ds\right]\cos(nx)+\sum_{n=1}^{\infty}\left[C_n^2 e^{-an^2t}+\int_0^t e^{-an^2(t-s)}F_n^2(s)\,ds\right]\sin(nx), \tag{7.1}$$

where,

$$\begin{aligned} C_0^1&=\frac{1}{L}\int_0^L f(x)\,dx, & F_0^1&=\frac{1}{L}\int_0^L F(x,t)\,dx,\\ C_n^1&=\frac{2}{L}\int_0^L f(x)\cos(nx)\,dx, \quad , & F_n^1&=\frac{2}{L}\int_0^L F(x,t)\cos(nx)\,dx,\\ C_n^2&=\frac{2}{L}\int_0^L f(x)\sin(nx)\,dx, & F_n^2&=\frac{2}{L}\int_0^L F(x,t)\sin(nx)\,dx. \end{aligned} \tag{7.2}$$

The proof of formulae (7.1) is explained in Appendix A.

The system of propagators (5.2) can be re-written using the Eigen function expansion (7.1) as:

$$u_\alpha(x,t)=\sum_{n=0}^{\infty}\left[C_n^1 e^{-an^2t}+\int_0^t e^{-an^2(t-s)}F_n^1(s)\,ds\right]\cos(nx)+\sum_{n=1}^{\infty}\left[C_n^2 e^{-an^2t}+\int_0^t e^{-an^2(t-s)}F_n^2(s)\,ds\right]\sin(nx). \tag{7.3}$$

For $|\alpha|=0$ we get:

$$\frac{\partial}{\partial t}u(x,t)=\gamma\frac{\partial^2}{\partial x^2}u(x,t),\quad u_0(x,0)=\sin(x),$$

which results in:

$$u_\alpha(x,t)=e^{-\gamma t}\sin(x). \tag{7.4}$$

For $|\alpha|=1,\ \alpha_1=1,\ \alpha_i=0$ we get:

$$\frac{\partial}{\partial t}u(x,t)=\gamma\frac{\partial^2}{\partial x^2}u(x,t)+\sigma m_1(t)\frac{\partial}{\partial x}u_{|\alpha|=0}(x,t),\quad u_\alpha(x,0)=0,$$

which results in:

$$u_\alpha(x,t)=\frac{\sigma t}{\sqrt{T}}e^{-\gamma t}\cos(x). \tag{7.5}$$

For $|\alpha|=1,\ \alpha_i=1,\ \alpha_1=0,\ i>1$ we get:

$$\frac{\partial}{\partial t}u(x,t)=\gamma\frac{\partial^2}{\partial x^2}u(x,t)+\sigma m_i(t)\frac{\partial}{\partial x}u_{|\alpha|=0}(x,t),\quad u_\alpha(x,0)=0,$$

which results in:

$$u_\alpha(x,t)=\frac{\sigma\sqrt{2}}{\pi k\sqrt{T}}e^{-\gamma t}\sin(k\pi t)\cos(x),\ k=(i-1)/T. \tag{7.6}$$

For $|\alpha| = 2,\ \alpha_1 = 2,\ \alpha_i = 0,\ i > 1$ we get:

$$\frac{\partial}{\partial t}u(x,t) = \gamma \frac{\partial^2}{\partial x^2}u(x,t) + \sigma m_1(t)\frac{\partial}{\partial x}u_{|\alpha|=1,\alpha_1=1}(x,t), \quad u_\alpha(x,0) = 0,$$

which results in:

$$u_\alpha(x,t) = \frac{-\sigma^2 t^2}{\sqrt{2}\,T} e^{-\gamma t}\sin(x). \tag{7.7}$$

For $|\alpha| = 2,\ \alpha_1 = 0,\ \alpha_i = 2,\ i > 1$ we get:

$$\frac{\partial}{\partial t}u(x,t) = \gamma \frac{\partial^2}{\partial x^2}u(x,t) + \sqrt{2}\sigma m_i(t)\frac{\partial}{\partial x}u_{|\alpha|=1,\alpha_i=1}(x,t), \quad u_\alpha(x,0) = 0,$$

which results in:

$$u_\alpha(x,t) = \frac{-\sqrt{2}\,\sigma^2}{T\,\pi^2 k^2} e^{-\gamma t}\sin^2(k\pi t)\sin(x). \tag{7.8}$$

For $|\alpha| = 2,\ \alpha_1 = 1,\ \alpha_i = 1,\ i > 1$ we get:

$$\frac{\partial}{\partial t}u(x,t) = \gamma \frac{\partial^2}{\partial x^2}u(x,t) + \sigma m_1(t)\frac{\partial}{\partial x}u_{|\alpha|=1,\alpha_i=1}(x,t) + \sigma m_i(t)\frac{\partial}{\partial x}u_{|\alpha|=1,\alpha_1=1}(x,t), \quad u_\alpha(x,0) = 0,$$

which results in:

$$u_\alpha(x,t) = \frac{-\sqrt{2}\,\sigma^2 t}{T\,\pi\ k} e^{-\gamma t}\sin(k\pi t)\ \sin(x). \tag{7.9}$$

For $|\alpha| = 2,\ \alpha_i = 1,\ \alpha_l = 1,\ i, l > 1$ we get:

$$\frac{\partial}{\partial t}u(x,t) = \gamma \frac{\partial^2}{\partial x^2}u(x,t) + \sigma m_i(t)\frac{\partial}{\partial x}u_{|\alpha|=1,\alpha j=1}(x,t) + \sigma mj(t)\frac{\partial}{\partial x}u_{|\alpha|=1,\alpha_i=1}(x,t),\ u_\alpha(x,0) = 0;\ i, j > 1,\ i < j,$$

which results in:

$$u_\alpha(x,t) = \frac{-2\sigma^2}{T\,\pi^2 k\,k_2} e^{-\gamma t}\sin(k\pi t)\sin(k_2\pi s)\sin(x), \quad k_2 = j - 1/T. \tag{7.10}$$

Then we have:

$$u_0 = e^{-\gamma t}\sin(x),$$

$$u_{|\alpha|=1} = \frac{\sigma}{\sqrt{T}} e^{-\gamma t}\cos(x)\left[t + \frac{\sqrt{2}}{\pi k}\sin(k\pi t)\right],\ k = (i-1)/T,$$

$$u_{|\alpha|=2} = \frac{-\sigma^2}{T} e^{-\gamma t}\sin(x)\left[\frac{t^2}{\sqrt{2}} + \frac{\sqrt{2}\,t}{\pi\ k}\sin(k\pi t) + \frac{2}{\pi^2 k\,k_2}\sin(k\pi t)\sin(k_2\pi t) + \frac{\sqrt{2}}{\pi^2 k^2}\sin^2(k\pi t)\right],$$

$$, k_2 = j - 1/T.$$

The WHE differential equations (6.2), (6.3) and (6.4) can be solved using perturbation technique [7]. We can use the perturbation technique about advection coefficient σ combining with the Eigen function expansion (7.1) to calculate the first, second, third and fourth corrections.

Compare the coefficients of σ^0 :

$$\frac{\partial}{\partial t}u_0^0(x,t)-\mu\frac{\partial^2}{\partial x^2}u_0^0(x,t)=0,\quad u_0^0(x,0)=\sin(x),$$

to get $u_0^0(x,t)=e^{-\mu t}\sin(x),$ (7.11)

$$\frac{\partial}{\partial t}u_0^1(x,t;t_1)-\mu\frac{\partial^2}{\partial x^2}u_0^1(x,t;t_1)=0,\quad u_0^1(x,0;t_1)=0,$$

to get $u_0^1(x,t;t_1)=0,$ (7.12)

$$\frac{\partial}{\partial t}u_0^2(x,t;t_1,t_2)-\mu\frac{\partial^2}{\partial x^2}u_0^2(x,t;t_1,t_2)=0,\quad u_0^2(x,0;t_1,t_2)=0,$$

to get $u_0^2(x,t;t_1,t_2)=0.$ (7.13)

Compare the coefficients of σ^1 :

$$\frac{\partial}{\partial t}u_1^0(x,t)-\mu\frac{\partial^2}{\partial x^2}u_1^0(x,t)=\frac{\partial}{\partial x}u_0^1(x,t;t),\quad u_1^0(x,0)=0,$$

to get $u_1^0(x,t)=0,$ (7.14)

$$\frac{\partial}{\partial t}u_1^1(x,t;t_1)-\mu\frac{\partial^2}{\partial x^2}u_1^1(x,t;t_1)=\delta(t-t_1)\frac{\partial}{\partial x}u_0^0(x,t)+2\frac{\partial}{\partial x}u_0^2(x,t;t,t_1),\quad u_1^1(x,0;t_1)=0,$$

to get $u_1^1(x,t;t_1)=e^{-\mu t}\cos(x),$ (7.15)

$$\frac{\partial}{\partial t}u_1^2(x,t;t_1,t_2)-\mu\frac{\partial^2}{\partial x^2}u_1^2(x,t;t_1,t_2)=\frac{1}{2}\delta(t-t_2)\frac{\partial}{\partial x}u_0^1(x,t;t_1)+\frac{1}{2}\delta(t-t_1)\frac{\partial}{\partial x}u_0^1(x,t;t_2),$$
$$u_1^2(x,0;t_1,t_2)=0,$$

to get $u_1^2(x,t;t_1,t_2)=0.$ (7.16)

Compare the coefficients of σ^2 :

$$\frac{\partial}{\partial t}u_2^0(x,t)-\mu\frac{\partial^2}{\partial x^2}u_2^0(x,t)=\frac{1}{2}\frac{\partial^2}{\partial x^2}u_0^0(x,t)+\frac{\partial}{\partial x}u_1^1(x,t;t),\quad u_2^0(x,0)=0,$$

to get $u_2^0(x,t)=\frac{-3}{2}t\,e^{-\mu t}\sin(x),$ (7.17)

$$\frac{\partial}{\partial t}u_2^1(x,t;t_1)-\mu\frac{\partial^2}{\partial x^2}u_2^1(x,t;t_1)=\frac{1}{2}\frac{\partial^2}{\partial x^2}u_0^1(x,t;t_1)+\delta(t-t_1)\frac{\partial}{\partial x}u_1^0(x,t)+2\frac{\partial}{\partial x}u_1^2(x,t;t,t_1),$$
$$u_2^1(x,0;t_1)=0,$$

to get $u_2^1(x,t;t_1)=0,$ (7.18)

$$\frac{\partial}{\partial t}u_2^2(x,t;t_1,t_2)-\mu\frac{\partial^2}{\partial x^2}u_2^2(x,t;t_1,t_2)=\frac{1}{2}\frac{\partial^2}{\partial x^2}u_0^2(x,t;t_1,t_2)+\frac{1}{2}\delta(t-t_2)\frac{\partial}{\partial x}u_1^1(x,t;t_1)$$
$$+\frac{1}{2}\delta(t-t_1)\frac{\partial}{\partial x}u_1^1(x,t;t_2),\qquad u_2^2(x,0;t_1,t_2)=0,$$

to get $u_2^2(x,t;t_1,t_2)=-e^{-\mu t}\sin(x).$ (7.19)

Compare the coefficients of σ^3 :

$$\frac{\partial}{\partial t}u_3^0(x,t)-\mu\frac{\partial^2}{\partial x^2}u_3^0(x,t)=\frac{1}{2}\frac{\partial^2}{\partial x^2}u_1^0(x,t)+\frac{\partial}{\partial x}u_2^1(x,t;t),\quad u_3^0(x,0)=0,$$

to get $u_3^0(x,t)=0,$ (7.20)

$$\frac{\partial}{\partial t}u_3^1(x,t;t_1)-\mu\frac{\partial^2}{\partial x^2}u_3^1(x,t;t_1)=\frac{1}{2}\frac{\partial^2}{\partial x^2}u_1^1(x,t;t_1)+\delta(t-t_1)\frac{\partial}{\partial x}u_2^0(x,t)+2\frac{\partial}{\partial x}u_2^2(x,t;t,t_1),\quad u_3^1(x,0;t_1)=0,$$

to get $u_3^1(x,t;t_1)=-\frac{5}{2}t\,e^{-\mu t}\cos(x)-\frac{3}{2}t_1\,e^{-\mu t}\cos(x),$ (7.21)

$$\frac{\partial}{\partial t}u_3^2(x,t;t_1,t_2)-\mu\frac{\partial^2}{\partial x^2}u_3^2(x,t;t_1,t_2)=\frac{1}{2}\frac{\partial^2}{\partial x^2}u_1^2(x,t;t_1,t_2)+\frac{1}{2}\delta(t-t_2)\frac{\partial}{\partial x}u_2^1(x,t;t_1),$$
$$+\frac{1}{2}\delta(t-t_1)\frac{\partial}{\partial x}u_2^1(x,t;t_2),\qquad u_3^2(x,0;t_1,t_2)=0,$$

to get $u_3^2(x,t;t_1,t_2)=0.$ (7.22)

Compare the coefficients of σ^4 :

$$\frac{\partial}{\partial t}u_4^0(x,t)-\mu\frac{\partial^2}{\partial x^2}u_4^0(x,t)=\frac{1}{2}\frac{\partial^2}{\partial x^2}u_2^0(x,t)+\frac{\partial}{\partial x}u_3^1(x,t;t),\quad u_4^0(x,0)=0,$$

to get $u_4^0(x,t)=\frac{19}{8}t^2e^{-\mu t}\sin(x),$ (7.23)

$$\frac{\partial}{\partial t}u_4^1(x,t;t_1)-\mu\frac{\partial^2}{\partial x^2}u_4^1(x,t;t_1)=\frac{1}{2}\frac{\partial^2}{\partial x^2}u_2^1(x,t;t_1)+\delta(t-t_1)\frac{\partial}{\partial x}u_3^0(x,t)+2\frac{\partial}{\partial x}u_3^2(x,t;t,t_1),$$

to get $u_4^1(x,0;t_1)=0,\quad u_4^1(x,t;t_1)=0,$ (7.24)

$$\frac{\partial}{\partial t}u_4^2(x,t;t_1,t_2)-\mu\frac{\partial^2}{\partial x^2}u_4^2(x,t;t_1,t_2)=\frac{1}{2}\frac{\partial^2}{\partial x^2}u_2^2(x,t;t_1,t_2)+\frac{1}{2}\delta(t-t_2)\frac{\partial}{\partial x}u_3^1(x,t;t_1)$$
$$+\frac{1}{2}\delta(t-t_1)\frac{\partial}{\partial x}u_3^1(x,t;t_2),\qquad u_4^2(x,0;t_1,t_2)=0,$$

to get $u_4^2(x,t;t_1,t_2)=\frac{1}{2}te^{-\mu t}\sin(x)+2t_2e^{-\mu t}\sin(x)+2t_1e^{-\mu t}\sin(x).$ (7.25)

Then we have

$$u^{(0)}(x,t) = e^{-\mu t}\sin(x)(1-\frac{3}{2}\sigma^2 t+\frac{19}{8}\sigma^4 t^2),$$
$$u^{(1)}(x,t) = \sigma e^{-\mu t}\cos(x)\left(1-\frac{5}{2}\sigma^2(t+\frac{3}{5}t_1)\right), \quad (7.26)$$
$$u^{(2)}(x,t) = \sigma^2 e^{-\mu t}\sin(x)\left(-1+0.5\sigma^2\left(t+4t_1+4t_2\right)\right).$$

Then the mean and the variance are:

$$E[u(x,t)] = u^{(0)}(x,t) = e^{-\mu t}\sin(x)(1-\frac{3}{2}\sigma^2 t+\frac{19}{8}\sigma^4 t^2),$$
$$\text{var}(u(x,t)) = \int_0^t [u^{(1)}(x,t;t_1)]^2 dt_1 + 2\int_0^t\int_0^t [u^{(2)}(x,t;t_1,t_2)]^2 dt_1 dt_2, \quad (7.27)$$
$$= \sigma^2 e^{-2\mu t}\cos^2(x)\left(t-\frac{13}{2}\sigma^2 t^2+\frac{43}{4}\sigma^4 t^3\right)+2\sigma^4 e^{-2\mu t}\sin^2(x)\left(\frac{t^2}{2}-\frac{5}{2}\sigma^2 t^3+\frac{83}{24}\sigma^4 t^4\right).$$

The WHEP technique gives the mean and the variance of the solution in the form of an infinite series in σ. Since σ represents the perturbation parameter in the WHEP technique, decreasing this parameter gives a good convergence.

VIII. NUMERICAL RESULTS

In order to examine the efficiency of the proposed methods, comparisons between the approximate solutions and the exact solution of the SADE are simulated through the following figures. We also introduce some discussion about the effect of the diffusion coefficient and advection coefficient.

We take $T = 5$ and 50 Gaussian random variable. As shown in Figs (1-22), we can note, the approximate solution of the two methods and the exact solution are in satisfactory agreement with each other under some convergence conditions. The convergence of the WCE is enhanced by increasing the number of Gaussian random variables K. The convergence of the WHEP is enhanced by decreasing the perturbation parameter σ which represents the advection and also white noise coefficient.

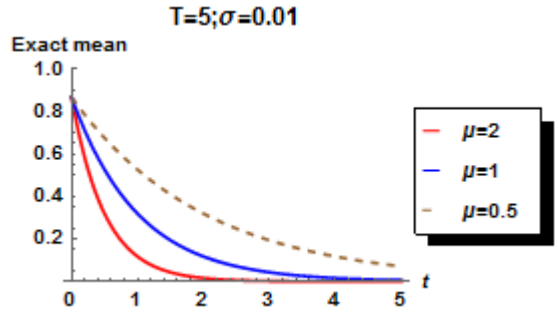

FIG 1. The exact mean at $x = \pi/3$ for different values of μ.

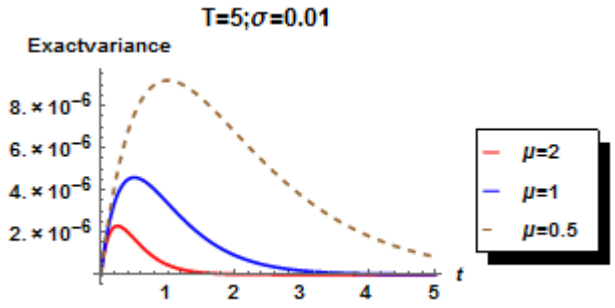

FIG 2. The exact variance at $x = \pi/3$ for different values of μ.

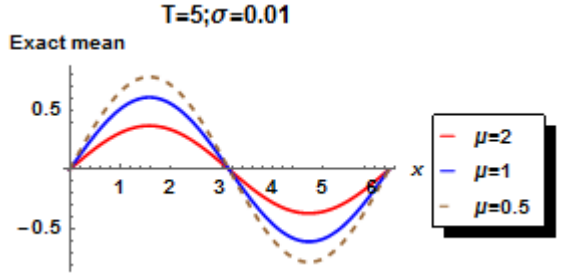

FIG 3. The exact mean at $t = 0.5$ for different values of μ.

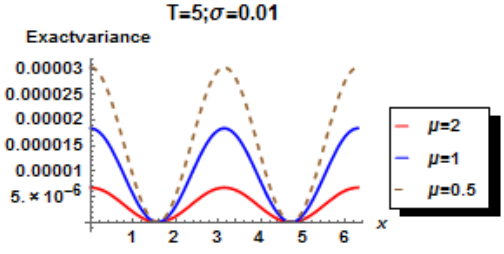

FIG 4. The exact variance at $t = 0.5$ for different values of μ.

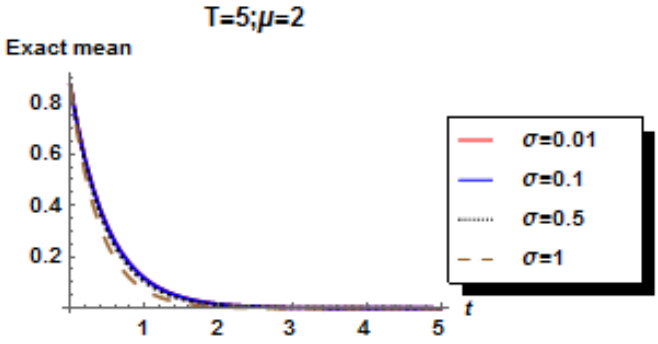

FIG 5. The exact mean at $x = \pi/3$ for different values of σ .

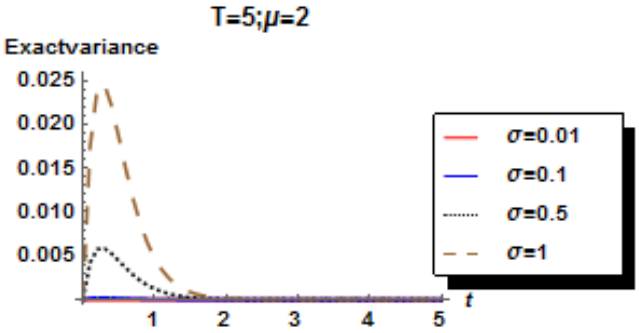

FIG 6. The exact variance at $x = \pi/3$ for different values of σ .

First, we examine the effect of the diffusion coefficient μ and the advection coefficient σ on the exact solution with respect to the convergence rate (5.3) in Figs (1 - 6). Studying those figures, we can note that, for fixed point x, the decaying exponential function $e^{-\mu t}$ affects the solution. The mean solution and the variance solution decay faster with time at large values of diffusion coefficient μ. The larger the diffusion, the vanished faster the variance over time is. For fixed point t, the effect of the sinusoidal function appears on the behavior of the solution. As the diffusion coefficient μ increases, the variance decreases with time.

We investigate the effect of the advection coefficient σ on the solution of the mass transfer in Figs (5, 6). Examining those figures we found that, as the coefficient σ increases, the solution decreases and vanishes with the time. As the coefficient σ decreases, the variance also decreases. So choosing large value of μ and small value of σ is appropriate for good convergence of the approximate solution.

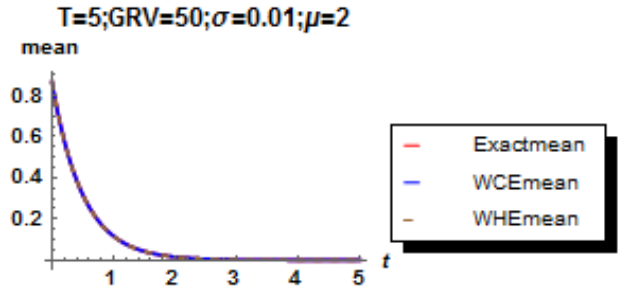

FIG 7. Second order means response for the exact, WCE and WHEP. Comparison between the three means at $x = \pi/3$.

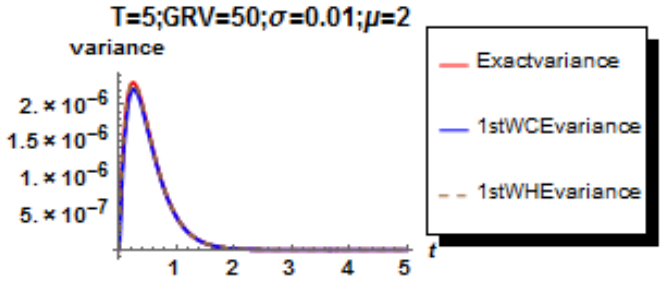

FIG 8. First order response variances for the exact, WCE and WHEP. Comparison between the three variances at $x = \pi/3$.

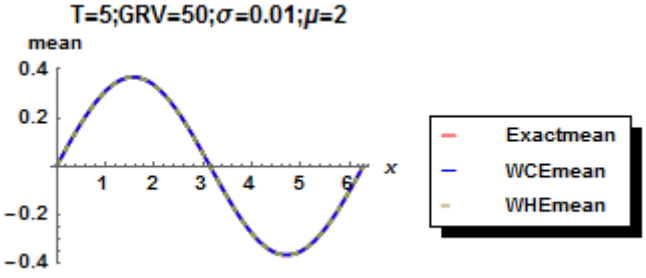

FIG 9. Second order means response for the exact, WCE and WHEP. Comparison between the three means at $t = 0.5$.

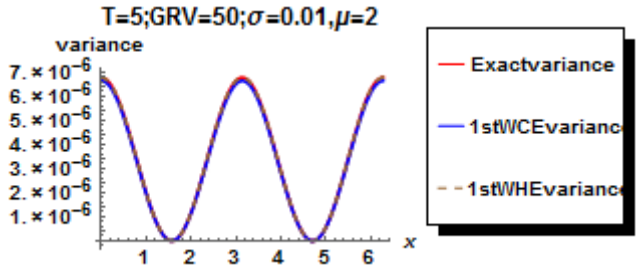

FIG 10. First order response variances for the exact, WCE and WHEP. Comparison between the three variances at $t = 0.5$.

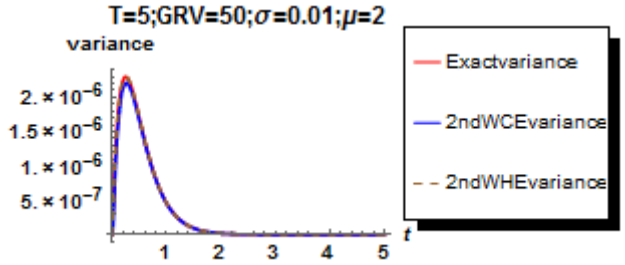

FIG 11. Second order response variances for the exact, WCE and WHEP. Comparison between the three variances at $x = \pi / 3$ **.**

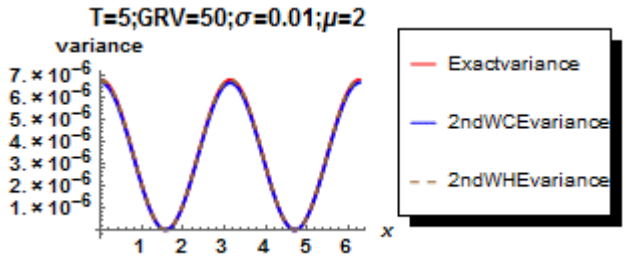

FIG 12. Second order response variances for the exact, WCE and WHEP. Comparison between the three variances at $t = 0.5$ **.**

The comparison between the exact solution and both approximate solutions of the WCE and WHEP techniques are shown in Figs (7-11). Examining those figures elucidate a satisfactory agreement between the exact solution and the approximate solutions either in mean or variance.

The effect of increasing the magnitude of the advection term σu_x is examined in Figs (13-16). We can note that increasing σ makes a deviation between the exact solution and the approximate solutions especially in the case of using the WHEP technique. This deviation is a result of using the WHEP technique which gives a mean solution and variance in the form of an infinite series in σ and t.

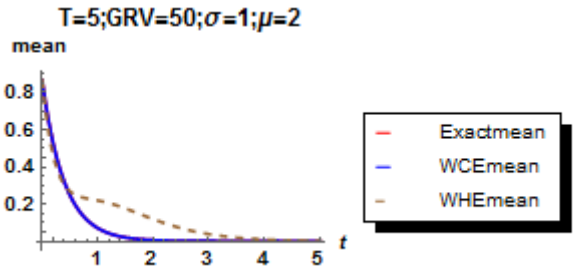

FIG 13. Second order means response for the exact, WCE and WHEP. Comparison between the three means at $x = \pi / 3, \sigma = 1$ **.**

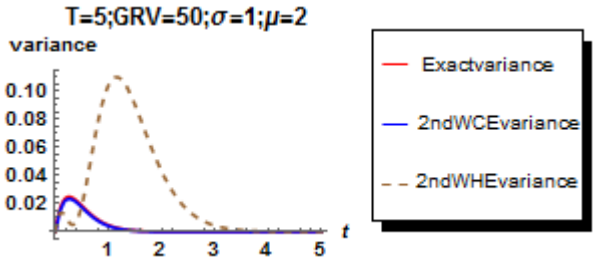

FIG 14. Second order response variances for the exact, WCE and WHEP. Comparison between the three variances at $x = \pi / 3, \sigma = 1$ **.**

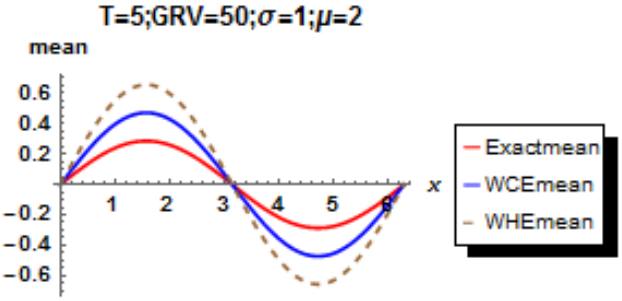

FIG 15. Second order means response for the exact, WCE and WHEP. Comparison between the three means at $t = 0.5, \sigma = 1$ **.**

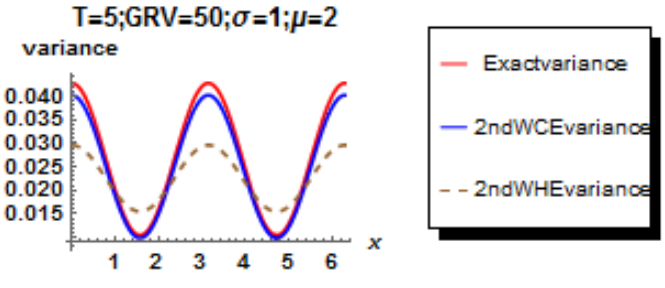

FIG 16. Second order response variances for the exact, WCE and WHEP. Comparison between the three variances at $t = 0.5, \sigma = 1$ **.**

From Figs (17, 18) we found that decreasing the number of GRVs leads to a deviation of the approximate solution of WCE. The larger the number of GRVs, the better convergence is.

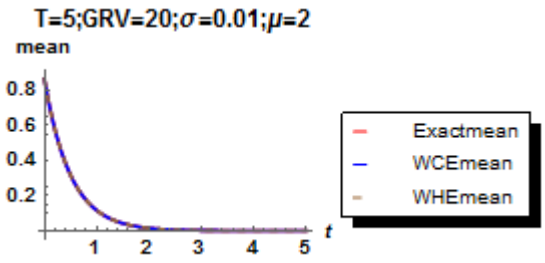

FIG 17. Second order means response for the exact, WCE and WHEP. Comparison between the three means at $x = \pi / 3$ and $GRV = 20$.

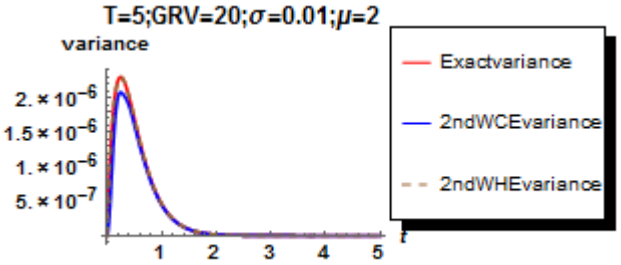

FIG 18. Second order response variances for the exact, WCE and WHEP. Comparison between the three variances at $x = \pi / 3$ and $GRV = 20$.

Finally, we show the errors between the exact solution and the approximate solutions of both WCE and WHEP techniques. We investigate the effects of the coefficients of SADE on the error. In Fig 19 we found that, the error between the exact solution and the WCE approximate solution is decreased by increasing order solution of WCE. In Fig 20 we found that, as the diffusion coefficient μ increases, the error of second order approximate solution decreases.

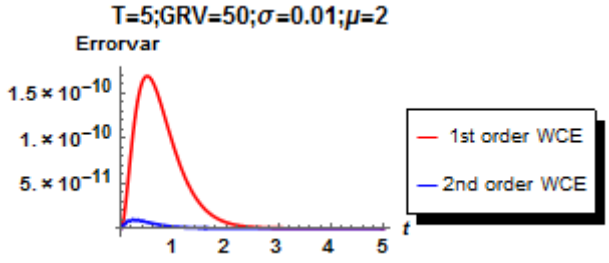

FIG 19. Error of variance response for 1st and 2nd order approximation of WCE. Comparison between the errors at $x = \pi / 2$.

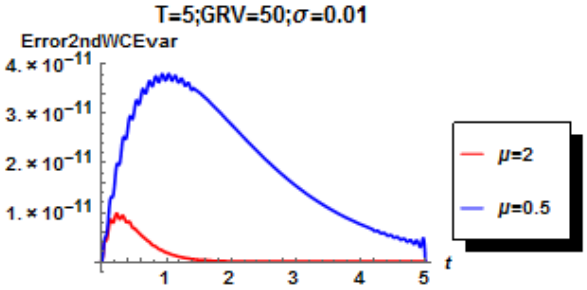

FIG 20. Error of second order approximation variance of WCE. Comparison between the errors for different value of μ at $x = \pi / 2$.

In Fig (21-22) we found that, the error of WCE approximate solution is less than the error of the WHEP approximate solution. We can obtain the following conclusion: the WCE technique is better than the WHEP technique.

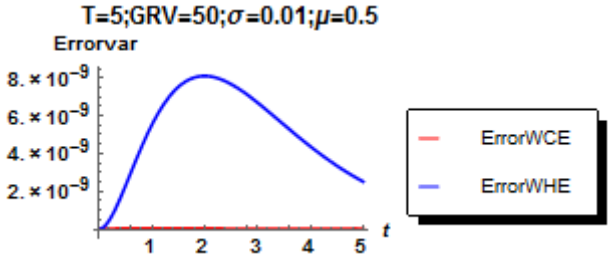

FIG 21. Second order response variance for the WCE and WHE. Comparison between the errors of variance at $x = \pi / 2$ and $\mu = 0.5$.

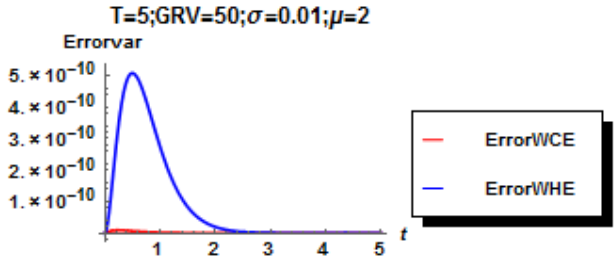

FIG 22. Second order response variance for the WCE and WHE. Comparison between the errors of variance at $x = \pi / 2$ and $\mu = 2$.

IX. CONCLUSION

In this paper, the solution of the SADE with multiplicative white noise using WCE and WHEP techniques is introduced. The numerical results show that the WCE technique gives the closed form mean solution while the WHEP technique gives the mean solution in the form of an infinite series. Both techniques give the variance of the solution process in the form of infinite series.

The numerical results not only demonstrate the accuracy of the two techniques, but also show that the WCE technique is more efficient than the WHEP technique. The diffusion and advection coefficient and the intensity of Gaussian white noise play important roles in the SADE solution.

The convergence of the WCE depends on increasing the number of Gaussian random variables. The convergence of the WHEP technique depends on decreasing the perturbation parameter σ. The larger the diffusion coefficient, the more convergence the approximate solution is. The effect of advection coefficient is contrary to that of diffusion coefficient, i.e., the smaller the advection coefficient, the more convergence the approximate solution.

APPENDIX A

To prove the formula (7.1), let we have the general form of equation (2.2) with initial condition and a periodic boundary condition on x not for $-L \le x \le L$ but for $0 \le x \le 2\pi$,

$$u_t(x,t) = a\,u_{xx}(x,t) + F(x,t), \quad u(x,0) = f(x),$$
$$u(0,t) = u(2\pi,t), \ \frac{du(0,t)}{dx} = \frac{du(2\pi,t)}{dx}, \tag{10.1}$$

for the homogenous case of equation (10.1), the solution will be in the form $u(x,t) = \sum_n T_n(t)Q_n(x)$, then we have

$$\frac{dT}{dt} = -a\lambda T, \quad \frac{d^2Q}{dx^2} + \lambda Q = 0, \tag{10.2}$$

there are three cases for λ. For $\lambda > 0$ the solution will be $Q(x) = A\cos(\sqrt{\lambda}x) + B\sin(\sqrt{\lambda}x)$, the second case for $\lambda = 0$ the solution will be $Q(x) = A + Bx$ and the third case is $\lambda < 0$ and the solution will be $Q(x) = A\cosh(\sqrt{-\lambda}x) + B\sinh(\sqrt{-\lambda}x)$, after the application of boundary conditions for the three cases we will have the general Fourier series of a function with 2π period as

$$X(x) = \sum_{n=0}^{\infty} X_n^1 \cos(nx) + \sum_{n=1}^{\infty} X_n^2 \sin(nx) = \sum_{n,j} X_n^j Q_n^j(x), \tag{10.3}$$

with the Fourier coefficients

$$X_0 = \frac{1}{2\pi}\int_0^{2\pi} X(x)\,dx,$$
$$X_n^1 = \frac{1}{\pi}\int_0^{2\pi} X(x)\cos(nx)\,dx, \tag{10.4}$$
$$X_n^2 = \frac{1}{\pi}\int_0^{2\pi} X(x)\sin(nx)\,dx.$$

Let $u(x,t) = \sum_{n,j} u_n^j(t)Q_n^j(x)$ in equation (10.1) we get: $\sum_{n,j}\frac{d}{dt}u_n^j(t)Q_n^j(x) - a\sum_{n,j}u_n^j(t)Q_n^j(x)'' = \sum_{n,j}F_n^j(t)Q_n^j(x)$,

$$\sum_{n,j}\left[\frac{d}{dt}u_n^j(t) + a\lambda_n u_n^j(t) - F_n^j(t)\right]Q_n^j(x) = 0, \tag{10.5}$$

and for the initial condition,

$$f(x) = \sum_{n,j} C_n^j Q_n^j(x),$$
$$u(x,0) = \sum_{n,j} u_n^j(0)Q_n^j(x) = \sum_{n,j} C_n^j Q_n^j(x) \Rightarrow \sum_{n,j}\left[u_n^j(0) - C_n^j\right]Q_n^j(x) = 0, \tag{10.6}$$

$$\frac{d}{dt}u_n^j(t)+a\lambda_n u_n^j(t)-F_n^j(t)=0,\quad u_n^j(0)-C_n^j=0,\quad \lambda_n=n^2, \tag{10.7}$$

multipling both sides by $e^{-a\lambda_n t}$ and integrates then multiply by its orthognality then in the end we will get

$$u(x,t)=\sum_{n=0}^{\infty}\left[C_n^1 e^{-an^2t}+\int_0^t e^{-an^2(t-s)}F_n^1(s)\,ds\right]\cos(nx)+\sum_{n=1}^{\infty}\left[C_n^2 e^{-an^2t}+\int_0^t e^{-an^2(t-s)}F_n^2(s)\,ds\right]\sin(nx).$$

REFERENCES

[1] P. E. Kloeden, and E. Platen, Numerical Solution of Stochastic Differential Equations areds. Springer, Berlin, (1995).

[2] B. Oksendal, Stochastic Differential Equations: An Introduction with Application, Springer, Berlin, (1998).

[3] D. Nykamp and D. Tranchina. A population density method that facilitates large-scale modeling of neural networks: Extension to slow inhibitory synapses. *Neural Computation*, 13:511–546, 2001.

[4] N. Wiener. The homogeneous chaos. Amer. J. Math., 60:897–936, 1938.

[5] N. Wiener. Nonlinear Problems in Random Theory. MIT Press, Cambridge, 1958.

[6] W. C. Meecham and A. Siegel. Wiener-Hermite expansion in model turbulence at large Reynolds number. Phys. Fluids, 7:1178, 1964.

[7] M.A. El-Tawil, The Application of WHEP technique on stochastic partial differential equations, International Journal of Differential Equations and its Applications, Vol. 7, No.3, pp 325-337,2003.

[8] M.A. El-Beltagy and M.A El-Tawil, Toward a Solution of a Class of Non-Linear Stochastic perturbed PDEs Using Automated WHEP Algorithm, Applied Mathematical Modeling, 37 (2013) 7174–7192 7175.

[9] M.H. Abd-Elghany, M.A El-tawil, Wiener Hermite Expansion and Homotopy Method for Solving Stochastic DE: Wiener Hermite Expansion With Perturbation and Homotopy Techniques, Noor Publishing (2016), 188.pp.

[10] M. El-Beltagy and A. Al-Johani, "Higher-Order WHEP Solutions of Quadratic Nonlinear Stochastic Oscillatory Equation," Engineering, Vol. 5 No. 5A,(2013), pp. 57-69. doi: 10.4236/eng.2013.55A00.

[11] M.A. El-Tawil, and A. Fareed, "Solution of Sto-chastic Cubic and Quintic Nonlinear Diffusion Equation Using WHEP, Pickard and HPM Meth-ods," Open Journal of Discrete Mathematics, Vol. 1 No. 1, 2011, pp. 6-21.
doi:10.4236/ojdm.2011.11002.

[12] H. Cameron and W. T. Martin, "The Orthogonal Development of Non-linear Functionals in Series of Fourier- Hermite Functionals, Ann. Math., Vol. 48 (1947) pp. 385–392.

[13] H. Holden, B. Øksendal, J. Uboe, and T. Zhang. Stochastic Partial Differential Equations. A Modeling, White Noise Functional Approach. Birkh¨auser, Boston, 1996.

[14] R. Mikulevicius and B. Rozovskii. Linear parabolic stochastic PDEs and Wiener chaos. SIAM J. Math. Anal., 29:452–480, 1998.

[15] R. Mikulevicius and B. Rozovskii. Stochastic Navier-Stokes equations for turbulence flow. SIAM J. Math. Anal., 35:1250–1310, 2004.

[16] R. Mikulevicius and B. L. Rozovskii. Stochastic Navier-Stokes equations: Propagation of chaos and statistical moments. In J. L.Menaldi, E. Rofmann, and A. Sulem, editors, Optimal Control and Partial Differential Equations, pages 258–267, Amsterdam, 2001. IOS Press. In honor of Professor Alain Bensoussan's 60th Birthday.

[17] S. Lototsky, R. Mikulevicius, and B. Rozovskii. Nonlinear filtering revisited: a spectral approach. SIAM J. Control Optim., 35:435–461, 1997.

[18] S. V. Lototsky. Nonlinear filtering of diffusion processes in correlated noise: analysis by separation of variables. Appl. Math. Optim., 47(2):167–194, 2003.

[19] R. G. Ghanem. Stochastic finite element with multiple random non-Gaussian properties. J. Engrg. Mech., 125(1):26–40, 1998.

[20] S. Sakamoto and R. Ghanem. Polynomial chaos decomposition for the simulation of non-Gaussian non-stationary stochastic processes. J. Eng. Mech., 128:190–201, 2002.

[21] I. Babuska, R. Tempone, and G. E. Zouraris. Solving elliptic boundary value problems with uncertain coefficients by the finite element method: the stochastic formulation. Comput. Methods Appl. Mech. Engrg., 194:1251–1294, 2005.

[22] P. Frauenfelder, C. Schwab, and R. A. Todor. Finite elements for elliptic problems with stochastic coefficients. Comput. Method Appl. Mech. Engrg., 194:205–228, 2005.

[23] H. G. Matthies and A. Keese. Galerkin methods for linear and nonlinear elliptic stochastic partial differential equations. Comput. Methods Appl. Mech. Engrg., 194:1295 -1331, 2005.

[24] D. Xiu and G. E. Karnidakis. The Wiener-Askey polynomial chaos for stochastic differential equations. SIAM J. Sci. Comput., 24:619–644, 2002.

[25] D. Zhang and Z. Lu. An efficient, high-order perburbation approach for flow in random porous media via Karhunen-Loeve and polynomial expansion. J. Comput. Phy., 194:137–167, 2003.

[26] Lue W., "Wiener Chaos Expansion and Numerical Solutions of Stochastic Partial Differential Equations", PhD Thesis, California Institute of Technology, Pasadena, California, (2006).

[27] Z. Zhang, B. Rozovskii, M. V. Tretyakov, and G. E. Karniadakis,A Multistage Wiener Chaos Expansion Method for Stochastic Advection-Diffusion-Reaction Equations, *SIAM J. Sci. Comput.*, 34(2), (2012) A914–A936.

[28] T. Imamura, W. Meecham, A. Siegel, Symbolic Calculus of the Wiener Process and Wiener-Hermite Functional, J. Math. Phys. Vol. 6, No. 5, (1965), pp. 695–706.

[29] M. El Tawil, M. Elbeltagy, B.S. El-desouky and M. Hamed, Solution of Nonlinear Stochastic Langevin's Equation Using WHEP, Pickard and HPM Methods, Applied Mathematics, 2014, 5, 398-412.

[30] David H. Bailey, Paul N. Swarztrauber, "A fast method for the numerical evaluation of continuous Fourier and Laplace transforms", SIAM Journal on Scientific Computing , 15 (5): 1105–1110 , (1994), doi:10.1137/0915067.

Theory of Dipole-Exchange Spin Waves in a Ferromagnetic Nanotube. Consideration of Volume and Surface Modes

V.V. Kulish

Department of general and experimental physics, National Technical University of Ukraine "Igor Sikorsky Kyiv Polytechnic Institute", 37 Peremogy prosp., 03056, Kyiv, Ukraine

Abstract— *The paper extends study of dipole-exchange spin waves in a ferromagnetic nanotube with a circular cross-section started by the author in the previous paper. The proposed model considers the magnetic dipole-dipole interaction, the exchange interaction, the anisotropy effects, the damping effects, the general boundary conditions and the existence of both volume and surface modes for the considered spin waves. Therefore, a new method of obtaining the values' spectrum of the orthogonal (to the translation axis) wavenumbers for the investigated spin waves is proposed in addition to the previously obtained dispersion law. The method is based on the application of general boundary conditions for the magnetic field on a superposition of the above-mentioned modes. The obtained spectrum is shown to be a quasi-one-dimensional one – similar to that in a thin ferromagnetic field – for typical ferromagnetic nanotubes. Exploitation of the above-mentioned method essentially extends the area of application of the obtained results compared to the previous paper.*

Keywords— Spin wave, Dipole-exchange theory, Ferromagnetic nanotube, Volume mode, Surface mode.

I. INTRODUCTION

At the present time, a variety of actual and prospective technologies are based on the applications of spin waves in nanosystems. In particular, such waves are promising for application in information technologies – for creating new data storage [1], transfer [1,2] and processing [3] devices. One of the key problems for developing such technologies is theoretical modeling of spin-wave processes in these nanosystems. Such modeling is required not only for direct applications of spin waves, but also for synthesizing materials with preset magnetic properties because these properties are often influenced by spin-wave processes. This modeling, in turn, requires deeper understanding of the corresponding processes in magnetic nanosystems. In the proposed paper, one of the problems of the above-described type is solved.

It has been shown by numerous studies that the properties of nanosystems – in particular, spin-wave properties – depend essentially on their size and shape. Unfortunately, a general theory of spin waves in magnetic nanosystems has not been created at the moment. Therefore, spin waves in nanosystems of different geometries are studied separately. Among the variety of magnetic nanosystems of different configurations, a special class is represented by shell-type ferromagnetic nanosystems (nanoshells, nanotubes and others). These nanosystems exhibit unique – not inherent to traditional continuous nanosystems – magnetic properties that are prospective for numerous technical applications. For instance, magnetic properties of such nanosystems can be regulated more flexibly than properties of corresponding continuous nanosystems. However, such nanosystems remain poorly researched at the moment. In particular, study of spin waves in synthesized recently magnetic nanotubes [4] represents an actual topic of research.

The paper continues the study of dipole-exchange spin waves in a ferromagnetic nanotube with a circular cross-section started by the author in the papers [5,6]. In the study, the magnetic dipole-dipole interaction, the exchange interaction, the anisotropy effects and the damping effects are considered. In the previous papers of the author [5,6], a dispersion relation for the above-described spin waves has been obtained. However, for complete description of the considered waves, this relation should be complemented by either a relation between the wavenumber components or values' spectrum of the orthogonal (to the tube axis) wavenumber component. For the most nanosystems, that represents more challenging task than just finding the dispersion relation. Moreover, for thin films and nanotubes one should consider existence of both volume and surface modes that are, generally speaking, hybridized in the considered cases. In the papers [5,6], only a volume spin wave mode has been considered and the above-mentioned spectrum has been obtained only for a very specific particular case (the material outside the nanotube has been assumed to be a high-conductivity metal) thus essentially limiting the area of application of the entire obtained result. The proposed paper overcomes this limitation by considering both modes' types and applying a different – essentially more general – method of obtaining the above-mentioned spectrum. As a result, the obtained values' spectrum of the orthogonal wavenumber component has an essentially wider range of applications. The obtained spectrum of wavenumbers is shown to have a quasi-one-dimensional form for the considered (thin) nanotubes.

II. PROBLEM STATEMENT. MODEL DESCRIPTION

Let us consider a ferromagnetic nanotube – with a circular cross-section – composed of a uniaxial ferromagnet of the "easy axis" type. Let us denote the ferromagnet parameters as follows: the exchange constant α, the uniaxial anisotropy parameter β, the gyromagnetic ratio γ, the ground state magnetization $\vec{M}_0$ (is considered constant inside the tube), the dissipation parameter α_G (the Hilbert term is used for consideration of the dissipation), the external magnetic field $\vec{H}_0^{(e)}$ (is also considered constant). We assume that both the easy magnetization axis (with the direction unit vector $\vec{n}$) and the external magnetic field inside the tube are directed along the tube translation axis – the axis Oz. Therefore, the ground state magnetization is also directed along Oz. Let us denote the internal tube radius *a* and the external radius *b* (see Fig.1.).

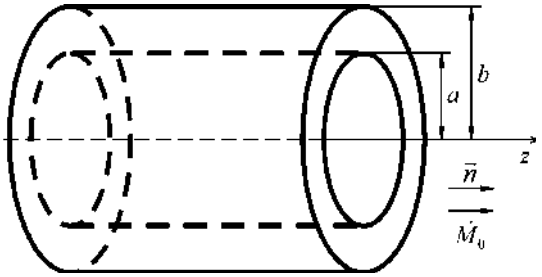

FIGURE 1. The nanotube that is studied in the paper.

Let us consider a spin wave propagating in the above-described nanotube. The magnetization $\vec{m}$ and the magnetic field $\vec{h}$ of the wave are assumed to be small perturbations of the overall magnetization $\vec{M}$ and the magnetic field inside the ferromagnet $\vec{H}^{(i)}$, correspondingly (linear wave). Thus, the relations $|\vec{m}| << |\vec{M}_0|$, $|\vec{h}| << |\vec{H}_0^{(i)}|$ fulfill, where $\vec{H}_0^{(i)}$ is the ground state internal magnetic field (so that $\vec{M} = \vec{M}_0 + \vec{m}$, $\vec{H}^{(i)} = \vec{H}_0^{(i)} + \vec{h}$). Let us consider the fact that for such spin waves, both volume and surface modes exist. The latter can make an essential contribution into spin-wave properties of the considered thin tube. Let us find the dispersion relation and the values' spectrum of the orthogonal (to the Oz axis) wavenumber for such linear spin waves.

For the investigated spin excitation, let us use the magnetostatic approximation, assuming that the magnetic potential Φ exists and, therefore, $\vec{h} = -\nabla\Phi$. After introducing amplitudes $\vec{m}_0$, $\vec{h}_0$ for the magnetization and the magnetic field perturbations, correspondingly (so that $\vec{m}(\vec{r},t) = \vec{m}_0(\vec{r})\exp(i\omega t)$, $\vec{h}(\vec{r},t) = \vec{h}_0(\vec{r})\exp(i\omega t)$, where ω is the wave frequency), we can write down the following relations for the magnetic potential: $\vec{h}_0 = -\nabla\Phi_0$, $\Phi = \Phi_0\exp(i\omega t)$. The outside material is considered non-magnetic so the relations $\vec{m}_0 = 0$, $\Delta\Phi_0$=0 fulfill outside the investigated ferromagnet. After combining the linearized Landau-Lishitz equation with the Maxwell equation $div\vec{H}^{(i)} = -4\pi div\vec{M}$ the following starting system of equations can be written (see [5,6]):

$$\begin{cases} i\omega\vec{m}_0 = \gamma M_0\vec{e}_z \times \left(\vec{h}_0 + \alpha\sum_i \dfrac{\partial^2\vec{m}_0}{\partial x_i^2} - \left(\beta + \dfrac{H_0^{(i)}}{M_0} - i\dfrac{\alpha_G\omega}{\gamma M_0}\right)\vec{m}_0\right), \\ \Delta\Phi_0 - 4\pi div\vec{m}_0 = 0 \end{cases} \quad (1)$$

here the cylindrical coordinates (ρ,θ,z) are used. After considering the fact that for the considered nanosystem symmetry $\vec{H}_0^{(i)} = \vec{H}_0^{(e)} - 4\pi\hat{N}\vec{M}_0 = \vec{H}_0^{(e)}$ (here $\hat{N}$ is the demagnetizing coefficients tensor) and eliminating the magnetization amplitude in (1), the following equation for the magnetic potential of the investigated waves can be obtained (see [5,6]):

$$\left(\frac{\omega^2}{\gamma^2 M_0^2} - \left(\tilde{\beta} - i\frac{\alpha_G\omega}{\gamma M_0} - \alpha\Delta\right)\left(\tilde{\beta} - i\frac{\alpha_G\omega}{\gamma M_0} + 4\pi - \alpha\Delta\right)\right)\Delta\Phi_0 + 4\pi\left(\tilde{\beta} - i\frac{\alpha_G\omega}{\gamma M_0} - \alpha\Delta\right)\frac{\partial^2\Phi_0}{\partial z^2} = 0, \quad (2)$$

here the value $\tilde{\beta} = \beta + H_0^{(e)}/M_0$.

The equation (2) should be complemented with the boundary conditions for the magnetic field. Analogously to the case of the ferromagnetic nanoshell (see the previous paper of the author [10]) let us assume that standard boundary conditions fulfill for the ground state magnetization and the magnetic field. Therefore, $b_{1n}=b_{2n}$, $h_{1\tau}=h_{2\tau}$ on the boundary of the considered ferromagnet (here medium 1 is the ferromagnet, medium 2 is the external medium, n means normal and τ – tangential to the boundary vector component, $\vec{b}$ is the magnetic induction vector of the wave). For the vectors $\vec{h}$, $\vec{m}$ one can obtain h_{1n}-$h_{2n}=4\pi m_n$, $h_{1\tau}=h_{2\tau}$ (as the outside environment is non-magnetic). From these conditions and the condition of the potential continuity on the ferromagnet boundary, the following relations for the magnetic potential imply:

$$\Phi_0\big|_1=\Phi_0\big|_2,\ \left(\nabla\Phi_0\right)_{1\tau}=\left(\nabla\Phi_0\right)_{2\tau},\ \frac{\partial\Phi_0}{\partial n}\bigg|_1-\frac{\partial\Phi_0}{\partial n}\bigg|_2=4\pi m_{0n}. \tag{3}$$

As the conditions (3) contain not only the magnetic potential, but also a normal component of the magnetization of the wave, boundary conditions for the magnetic potential should be implied in addition to (3). However, as it will be shown further, for the considered nanosystem the sought orthogonal wavenumber spectrum does not depend on these conditions.

The system (2) together with the boundary conditions (3) will be used as starting relations during further investigation.

III. SPECTRAL CHARACTERISTICS OF THE SPIN WAVES

Similarly to [5,6] let us seek a the potential inside the ferromagnet in the form

$$\Phi_0=\left(A_1J_n\left(k_\perp\rho\right)+A_2N_n\left(k_\perp\rho\right)\right)\exp\left(i\left(n\theta+k_{||}z\right)\right) \tag{4}$$

that satisfies the Poisson equation $\Delta\Phi_0=k^2\Phi_0$. Here A_1, A_2 are constants, $k_\perp$ and $k_\parallel$ are the orthogonal and longitudinal wavenumbers, correspondingly (they describe the wave propagation in the orthogonal to easy axis direction or along that direction, correspondingly), n is the mode number and J_n, N_n are the Bessel and Neumann functions of the order n, correspondingly.

$$\begin{aligned}&\alpha^2\left(k_{||}^2+k_\perp^2\right)^3+2\alpha\left(\beta+\frac{H_0^{(e)}}{M_0}-i\frac{\alpha_G\omega}{\gamma M_0}+2\pi\right)\left(k_{||}^2+k_\perp^2\right)^2+\\&+\left(\left(\beta+\frac{H_0^{(e)}}{M_0}-i\frac{\alpha_G\omega}{\gamma M_0}\right)\left(\beta+\frac{H_0^{(e)}}{M_0}-i\frac{\alpha_G\omega}{\gamma M_0}+4\pi\right)-\frac{\omega^2}{\gamma^2M_0^2}-4\pi\alpha k_{||}^2\right)\left(k_{||}^2+k_\perp^2\right)-4\pi\left(\beta+\frac{H_0^{(e)}}{M_0}-i\frac{\alpha_G\omega}{\gamma M_0}\right)k_{||}^2=0\end{aligned} \tag{5}$$

Substitution of the solution (4) into the equation (3) leads to the dispersion equation that is of the 6th order by $k_\perp$ for the given $k_\parallel$, ω. (The wavenumber $k_\perp$ has a discrete spectrum of values while $k_\parallel$ is varying approximately continuously because the nanotube length is much greater than its thickness. Therefore, the component $k_\parallel$ is chosen as the defining parameter.) Three roots (values of $k_\perp^2$) of this equation exists, one (with the real $k_\perp$ for $\alpha_G=0$) corresponds to the volume modes and other two (with complex values of $k_\perp$ that are complex-conjugate even for $\alpha_G=0$) correspond to surface modes that decay inside the tube from the internal ($\rho=a$, $\mathrm{Im}k_\perp>0$) and the external ($\rho=b$, $\mathrm{Im}k_\perp<0$) surfaces. Elementary spin excitation, therefore, should – in a general case – be a superposition of three excitations of the form (4), with three above-described values of $k_\perp$ (for the given $k_\parallel$, ω), denoted further as $k_\perp^{(1)}$ (volume mode) and $k_{\perp R}^{(2)}\pm ik_{\perp I}^{(2)}$ (surface modes). (Analogous effects for flat ferromagnetic films have been investigated, e.g., in [8]). In some cases this 3-modes elementary excitation can be separated into three individual modes that can exist independently. Therefore, the boundary conditions can be applied separately to the each mode.

Substitution of the potential (4) (regardless of whether it is single mode (4) or the above-described superposition) leads to the following dispersion law [6]:

$$\omega=\frac{|\gamma|M_0}{1+\alpha_G^2}\left(\sqrt{\left(1+\alpha_G^2\right)\left(\alpha^2k^4+2\alpha\tilde{\beta}k^2+\tilde{\beta}^2+4\pi\alpha\left(1+\frac{\tilde{\beta}}{\alpha k^2}\right)k_\perp^2\right)-\alpha_G^2\left(\frac{K}{k}\right)^4}-i\alpha_G\left(\frac{K}{k}\right)^2\right), \tag{6}$$

here $K^2=\alpha k^4+\tilde{\beta}k^2+2\pi k_\perp^2$, $k^2=k_{||}^2+k_\perp^2$ is the total wavenumber. One can notice that spin waves can only be excited for small values $\alpha_G\leq0.1$ and, therefore, in the dispersion law (4) the addend α_G^2 can be neglected compared to 1. This allows rewriting the dispersion law (6) in the following simplified form:

$$\omega = |\gamma| M_0 \left(\sqrt{\alpha^2 k^4 + 2\alpha\tilde{\beta} k^2 + \tilde{\beta}^2 + 4\pi\alpha\left(1 + \frac{\tilde{\beta}}{\alpha k^2}\right) k_\perp^2 - 4\pi^2 \alpha_G^2 \frac{k_\perp^4}{k^4}} - i\alpha_G \left(\alpha k^2 + \tilde{\beta} + 2\pi \frac{k_\perp^2}{k^2} \right) \right). \quad (7)$$

Magnetic potential outside the tube Φ_0^e should satisfy the Laplace equation $\Delta\Phi_0=0$ and (together with its radial derivative) the continuity condition. Therefore, for a single mode (4) the outside potential has the following form:

$$\Phi_0^e = \begin{bmatrix} A_1^e I_n(k_{||}\rho)\exp(i(n\theta + k_{||}z)), & \rho \le a \\ A_2^e K_n(k_{||}\rho)\exp(i(n\theta + k_{||}z)), & \rho > b \end{bmatrix} \quad (8)$$

with the constants $A_1^e = (I_n(k_{||}a))^{-1}(A_1 J_n(k_\perp a) + A_2 N_n(k_\perp a))$, $A_2^e = (K_n(k_{||}b))^{-1}(A_1 J_n(k_\perp b) + A_2 N_n(k_\perp b))$. Here I_n, K_n are the modified Bessel functions of the first and the second kind, correspondingly, of the order n.

In order to use the third boundary condition in (3), amplitude magnetization components $m_{0\rho}$, $m_{0\theta}$ should also be found (the component $m_{0z}=0$ because $\vec{M}_0 \| Oz$). These components should have the form $m_{0\rho} = f_1(\rho)\exp(i(n\theta + k_{||}z))$, $m_{0\theta} = f_2(\rho)\exp(i(n\theta + k_{||}z))$. Therefore, the following system of equations for f_1, f_2 can be obtained from (1):

$$\begin{cases} \alpha f_1'' + \left(\frac{3\alpha}{\rho} + \frac{\omega\rho}{\gamma M_0 n} \right) f_1' - \left(\alpha\left(\frac{n^2+1}{\rho^2} + k_{||}^2 \right) + \left(\beta + \frac{H_0^{(e)}}{M_0} - i\frac{\alpha_G \omega}{\gamma M_0} \right) \right) f_1 - \frac{k^2 R}{4\pi}\left(\frac{2\alpha}{\rho} + \frac{\omega\rho}{\gamma M_0 n} \right) - R' = 0, \\ f_2 = -\frac{i\rho}{n}\left(\frac{k^2 R}{4\pi} - f_1' \right) \end{cases} \quad (9)$$

here $R(\rho)$ is a radial part of the dependence (4). This function is a combination of expressions $A_1 J_n(k_\perp\rho) + A_2 N_n(k_\perp\rho)$ with three above-described different values of $k_\perp$ (one for the volume mode and two for the surface modes). The considered nanotube is thin (b-a<<a) and, therefore, inside the nanotube $k_\perp\rho \sim 2\pi\rho\,(b-a)^{-1} >> 1$, $\rho \in [a,b]$ (for the complex values of $k_\perp$ this relation fulfils with $|k_\perp|$). Then, the asymptotics of the Bessel and Neumann functions can be used in (4): $J_n(k_\perp\rho) \approx \sqrt{2/(\pi k_\perp\rho)}\cos(k_\perp\rho - n\pi/2 - \pi/4)$, $N_n(k_\perp\rho) \approx \sqrt{2/(\pi k_\perp\rho)}\sin(k_\perp\rho - n\pi/2 - \pi/4)$. One can also note that for typical nanotubes their thickness is of the same order of magnitude as the exchange length (unities of nm for typical ferromagnets). Therefore, the factors that consider surface modes decay inside the nanotube can be considered approximately constant: $\exp(-k_{\perp I}^{(2)}\rho) \approx \exp(-k_{\perp I}^{(2)}a)$, $\exp(k_{\perp I}^{(2)}\rho) \approx \exp(k_{\perp I}^{(2)}b)$. Therefore, the function R can be rewritten as

$$R \approx \frac{1}{\sqrt{\rho}}\left(A_1^{(1)}\cos\left(k_\perp^{(1)}\rho - \frac{n\pi}{2} - \frac{\pi}{4}\right) + A_2^{(1)}\sin\left(k_\perp^{(1)}\rho - \frac{n\pi}{2} - \frac{\pi}{4}\right) + A_1^{(2)}\cos\left(k_{\perp R}^{(2)}\rho - \frac{n\pi}{2} - \frac{\pi}{4}\right) + A_2^{(2)}\sin\left(k_{\perp R}^{(2)}\rho - \frac{n\pi}{2} - \frac{\pi}{4}\right), \quad (10)$$

where $A_1^{(1)}$, $A_2^{(1)}$, $A_1^{(2)}$, $A_2^{(2)}$ are constants. After substituting the 3-modes combination (10) for the magnetic potential into the system of equations (9) and then – after taking corresponding derivatives – replacing ρ with its mean value $\rho_0=(a+b)/2$ in all power factors, one can obtain f_1 in the form

$$f_1 = \frac{1}{\sqrt{\rho}}\left(E_{11}\cos\left(k_\perp^{(1)}\rho - \frac{n\pi}{2} - \frac{\pi}{4}\right) + E_{12}\sin\left(k_\perp^{(1)}\rho - \frac{n\pi}{2} - \frac{\pi}{4}\right) + E_{21}\cos\left(k_{\perp R}^{(2)}\rho - \frac{n\pi}{2} - \frac{\pi}{4}\right) + E_{22}\sin\left(k_{\perp R}^{(2)}\rho - \frac{n\pi}{2} - \frac{\pi}{4}\right)\right). \quad (11)$$

Here E_{11}, E_{12}, E_{21}, E_{22} are constants. After substituting into the third boundary condition of system (3) the magnetic potential with the radial part in the form (10) (with replacement $\rho \to \rho_0$ in all power factors after taking radial derivatives) and the magnetization component $m_{0\rho}$ with the function f_1 in the form (11), one can notice that in the resulting system of equations, the values $(k_{||}/k_\perp)(I_n'(k_{||}a)/I_n(k_{||}a))$, $(k_{||}/k_\perp)(K_n'(k_{||}b)/K_n(k_{||}b))$ for both $k_\perp = k_\perp^{(1)}$, $k_\perp = k_{\perp R}^{(2)}$ can be neglected compared to unity when $k_{||}$<<$k_\perp$. (Really, the quantities $I_n'(k_{||}a)/I_n(k_{||}a)$, $K_n'(k_{||}b)/K_n(k_{||}b)$ are of the order of magnitude of $(k_{||}a)^{-1}$, $(k_{||}b)^{-1}$ correspondingly when $k_{||}a$<<1 and of the order of magnitude of unity or less on the remaining part of $k_{||}$ range. The quantity $k_\perp$ – when it is nonzero so the orthogonal spin excitations are present – is of the same order of magnitude as $(b-a)^{-1}$ and the nanotube is thin so that b-a<<a. Therefore, the quantities $(k_{||}/k_\perp)(I_n'(k_{||}a)/I_n(k_{||}a))$,

$\left(k_{||}/k_{\perp}\right)\left(K_n'\left(k_{||}b\right)/K_n\left(k_{||}b\right)\right)$ really are small compared to 1 regardless of the value of $k_{||}a$ as long as the relation $k_{||}<<k_{\perp}$ fulfils.) The quantity $k_{||}$ is of the same order of magnitude as the reverse length of the nanotube which is much less than $(b-a)^{-1}$, so the relation $k_{||}<<k_{\perp}$ fulfils – and, therefore, the above-mentioned quantities can be neglected – on the most part of both quantities' ranges. As a result, the above-mentioned boundary condition can be rewritten into the form $G_1\cos\left(k_{\perp}^{(1)}a+\alpha_1\right)+G_2\cos\left(k_{\perp R}^{(2)}a+\alpha_2\right)=0$, $G_1\cos\left(k_{\perp}^{(1)}b+\alpha_1\right)+G_2\cos\left(k_{\perp R}^{(2)}b+\alpha_2\right)=0$. Here G_1, G_2, α_1, α_2 are constants, combinations of $A_1^{(1)}$, $A_2^{(1)}$, $A_1^{(2)}$, $A_2^{(2)}$, E_{11}, E_{12}, E_{21}, E_{22}, $k_{\perp}^{(1)}$ and $k_{\perp R}^{(2)}$. Therefore, regardless of the exact form of the boundary conditions for the magnetization, the orthogonal wavenumber has the quasi-one-dimensional form: $k_{\perp}(b\text{-}a)=0$ for both values of $k_{\perp}$ and, correspondingly,

$$k_{\perp}^{(1)}=\pi s_1/(b-a),\ k_{\perp R}^{(2)}=\pi s_2/(b-a). \tag{12}$$

Here s_1, s_2 are non-negative integers (orthogonal modes' numbers). Therefore, the dispersion law for the investigated spin waves is given by the relation (7) with the orthogonal wavenumbers given by (12). For the volume mode these two relations completely describe the spectral characteristics of the wave.

IV. DISCUSSION

Let us analyze the obtained dispersion relation for the volume spin wave mode.

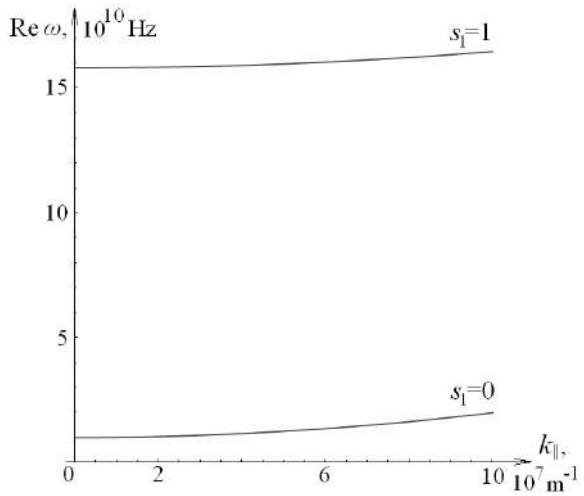

FIGURE 2. The dependence of Reω on $k_{\perp}$ for β=1, α=10^{-12} cm^{-2}, γ=10^7 Hz/Gs, M_0=10^3 Gs. The first two radial modes (s_1=0, s_1=1) are shown.

As it can be seen from (7), the dependence of the imaginary part of the frequency (that describes to the spin wave decay) on the longitudinal wavenumber $k_{||}$ in the investigated wavenumbers' range $k_{||}<<k_{\perp}$ is close to the square law: Im$\omega\approx|\gamma|M_0\alpha_G(\alpha($ $k_{||}^2+k_{\perp}^2)+\widetilde{\beta}+2\pi)$. On the other hand, the dependence of the real part of the frequency on $k_{||}$ is more complex but close to a constant if the orthogonal excitations are present ($k_{\perp}\neq0$). The mode with s_1=0, $k_{\perp}$=0 formally does not satisfy the relation $k_{||}<<k_{\perp}$; however, such mode is known to exist and is the only possible mode when the nanotube thickness is less than the exchange length. The dependence of Reω on $k_{\perp}$ for typical values on the nanotube parameters is depicted on the Fig. 2. The first two radial modes (s_1=0, s_1=1) are presented on the graph.

The longitudinal wavenumber is restricted, on the one hand, by the nanotube length – unities of micrometers for typical nanotubes – and, on the other hand, by the interatomic distance d_0 – several angstroms for typical materials. Therefore, the wavenumber lies in the interval 10^6-10^9 m^{-1}. Substitution of the above-mentioned typical values of nanotube parameters (β=1, α=10^{-12} cm^{-2}, γ=10^7 Hz/Gs, M_0=10^3 Gs) into the obtained dispersion law shows that the real part of the spin wave frequency lies in the interval 10^{10}-10^{12} Hz. This, really, is a frequencies interval for typical observed spin waves.

V. CONCLUSION

Thus, dipole-exchange spin waves in a ferromagnetic nanotube (easy-axis ferromagnet) have been studied in the paper. The

magnetic dipole-dipole interaction, the exchange interaction, the anisotropy effects and the damping effects have been considered. It has been shown that – similarly to the known case of a thin ferromagnetic film – in the considered nanotube, both surface and volume spin wave modes can be observed as well as hybrid modes. The dispersion law for such waves – obtained in the previous paper of the author – has been complemented with the spectrum of orthogonal wavenumber values. Unlike the previous papers of the author [5,6], the above-mentioned spectrum have been obtained using general boundary conditions for the magnetic field. This essentially extends the area of application of the obtained results compared to the papers [5,6] in which the spectrum has been found for a very specific particular case. It has been shown that for both modes' types the orthogonal wavenumber (for the surface modes – its real part) values' spectrum is quasi-one-dimensional on the most part of orthogonal and longitudinal wavenumbers' ranges. Therefore, the obtained results can be used for any round ferromagnetic nanotube of the studied configuration as long as the general model used in the paper (thin nanotube, linear waves, constant absolute value of the magnetization vector etc.) can be applied – and the mentioned model is applicable for typical round ferromagnetic nanotubes synthesized nowadays.

A graphical representation of the resulting dispersion relation with account for the obtained orthogonal wavenumber values' spectrum has been given. Numerical estimations of the spin waves' frequency for typical nanoshell parameters have been performed. The estimations have shown that the resulting frequency, really, lies within the frequencies interval for typical observed spin waves.

The method proposed in the paper can be applied to nanotubes of more complex configurations – in particular, to synthesized recently ferromagnetic nanotubes with an elliptic cross-section – as well as for more complex configurations of shell-type nanosystems in general. For some of them boundary conditions can be applied separately on volume and surface modes.

ACKNOWLEDGEMENTS

The author is grateful to Corresponding Member of the Academy of Pedagogical Sciences of Ukraine, Dr.Sci. (Phys.-Math.), Professor Yu.I. Gorobets for his attention to this work, fruitful discussions and valuable remarks.

REFERENCES

[1] C. Chappert, A. Fert, and F.N. Van Dau, "The emergence of spin electronics in data storage", Nat. Mater., vol.6, No.11, pp. 813–823, November 2007.

[2] S. Neusser and D. Grundler, "Magnonics: spin waves on the nanoscale", Adv. Mater., vol.21, pp. 2927–2932, June 2009.

[3] A. Khitun, M. Bao, and K.L. Wang, "Magnonic logic circuits", Journ. Phys. D: Appl. Phys., vol.43, No.26, 264005, June 2010.

[4] Y.Ye and B.Geng, "Magnetic Nanotubes: Synthesis, Properties, and Applications", Critical Reviews in Solid State and Materials Sciences, vol.37, pp.75-93, June 2012.

[5] V.V. Kulish, "Spin Waves in an Arbitrary Ferromagnetic Nanosystem with a Translational Symmetry. Nanotube with a Round Cross-section. Nanotube with an Elliptic Cross-section", Journal of nano- and electronic physics, vol.6, No.2, 02021, June 2014 [in Ukrainian].

[6] V.V. Kulish, "Spin Waves in a ferromagnetic nanotube. Account of dissipation and spin-polarized current", Ukr. Journ. Phys., vol.61, No.1, pp. 59-65, Jan 2016.

[7] V.V. Kulish, "Theory of Dipole-Exchange Spin Excitations in a Spherical Ferromagnetic Nanoshell. Consideration of the Boundary Conditions", IJOER, vol.3, Iss.9, pp.64-69, Sep 2017.

[8] E.B. Sonin, "Spin superfluidity and spin waves in YIG films", Phys. Rev. B, vol.95, 144432, Apr 2017.

Study on Different Types of Tenders, Tender Qualification/ Processing, Quantitative Techniques for Tendering, Planning and Monitoring

Manoj Kumar[1], B. Hemanth Roy[2]

[1]Assistant Professor, Department of Civil Engineering, Sri Ramakrishna Institute of Technology, Coimbatore - 641010, India.

[2]PG Student, Department of Civil Engineering, Sri Ramakrishna Institute of Technology, Coimbatore- 641010, India

Abstract— *Indian construction industry has played a vital role in the process of economic transformation and furtherance for over five decades and is the primary input for the socio-economic development of the country. Increasing complexity in design and involvement of numerous stakeholders in modern construction projects are huge challenge for both clients and contractors to meet criterion of skills and capabilities required to successfully deliver a project at bidding stage. Implementation of HAM (Hybrid- Annuity Model) to revive investments in road infrastructure projects, HAM has seen good initial success. About 30 highway projects have been awarded under HAM by the National Authority of India (NHAI) at a total cost of about 28,000crore. Half the projects awarded in HAM. This paper summaries the key changes and features which are brought under the new arrangement and provides a comparison with pat models.*

Keywords— tender notice, Hybrid Annuity Model, stakeholders.

I. INTRODUCTION

In India, road projects are awarded via one of the three models: Build-operate-transfer (BOT)- Annuity, BOT-Toll, EPC(Engineering, procurement and construction) contracts. After the BOT model of public private partnership (PPP) an advanced version of Model Concession Agreement (MCA), presently called as Hybrid Annuity Model is paving way for road projects. The Hybrid Model is supposed to be win-win situation for the Government and Developers. The government is expected to fund up to 40% of the project cost while remaining 60% to be funded by the private player, and thus easing the financial burden on the exchequer as well. This comes as a welcome step in the situation of dismal performance of highway construction projects awarded under MCA.

1.1 Background

The revised Model Concession Agreement (MCA), now called as Hybrid Annuity Model

(HAM) is a welcome change over all the previous Build Operate Transfer (BOT) model of Public Private Partner-ship (PPP).

Since the new union government took over in May, 2014 the question of languishing BOT projects was on top priority due to dismal performance of high-way construction projects awarded under existing model concession agreement. In very short time, the government came up with new HAM to ad-dress the various concerns felt by the stakeholders. By now first 2 projects are being awarded and more projects under same model will be awarded in coming months.

In last decade, many variants of PPP were experimented. Commonly adopted models were BOT with toll and BOT with annuity. Some early projects were awarded with success, mainly connecting important cities with steady and growing traffic. But soon it was clear that in some road segments may not have adequate toll paying traffic thus requiring partial government support. This was achieved through offering Viability Gap Funding (VGF) from 20% to 40 % of project cost and the Contractor asking for minimum VGF Grant could get the project. While experimenting with this VGF model, Government realized that some road connecting important cities had good prospects of collecting toll more than required for recovery of investment including interest and profits. This resulted into negative grant i.e. Contractors were willing to give money to government for awarding the project and those paying highest grant to government could get project awarded to them. More than 10-12 projects were awarded on these lines, perhaps due to over-enthusiasm of Contractors to get the projects. But soon

it was clear that reality was not rosy and Contractors started backing out of project, by returning the concession granted to them.

Still there were few projects in remote areas, which were not commercially viable due to their poor toll collection prospects. For such projects government decided to offer 100% support, by annuity payment over the concession period and the Contractor asking for lowest annuity was awarded project without toll collection responsibility. This idea was well received due to assured annuity without the responsibility of collecting toll. But soon Government felt that such annuity payment for large number of projects will create a permanent burden of annuity payout in all future budget and they decided to discontinue with this model unless very essential in rare cases.

In all this process, awarding of road construction projects slowed down. However to keep some nationally important linkage in remote areas going and to give some push to road construction, EPC/Turnkey projects were awarded with full payment by Government for construction, without any deferred payouts mechanism, to revive the road sector.

Hence all these combinations of payment arrangement needed a relook, as many of these were not working well and contractor stopped quoting for new BOT projects, due to various risks they were facing in the previously awarded projects.

1.2 How HAM is different?

The key changes and features which are brought in HAM MCA are summarized below. In general, HAM has brought in welcome change in the business environment due to the positive orientation of the government with a business friendly approach to achieve the speedy execution of long delayed highway projects.

The previous BOT model has structured the risk sharing with a major responsibility on the Con-tractor, managing financing risk, revenue risk and O&M risk apart from usual construction risk and government (or NHAI) was required to manage right of ways and granting toll collection rights to the Concessionaire. While in new HAM a dramatic realignment of Risk sharing is brought in. In this model, the government is accepting revenue (toll) collection risk, along with partial sharing (40%) of financial risk, and only expecting Contractor to continue managing execution and O&M risks. This is definitely much better balance compared to past risk al-location. In the process, they have brought in hybrid combination of old Annuity and BOT model and also EPC contract risks strategies. The brief picture of Risk Allocation can be tabulated as in Table 1.

TABLE 1
RISK ALLOCATION IN DIFFERENT CONTRACT MODELS

Type of Risk Type of Model	Financing risk	Revenue or toll collection risk	O & M Risk
BOT Model	By Private	By Private	By Private
Annuity Model	By Private	By Govt.	By Private
BOT-VGF Model	By Govt. & Private	By Private	By Private
EPC Model	By Govt.	By Govt.	By Govt.
HAM Model	By Govt. & Private	By Govt.	By Private

These changes though welcome are really favorable repackaging of various models in the past. For example, old annuity model was assuring minimum bi-annual release of payment to Concessionaire, with toll collection under government control while in some VGF models, there was willingness to pay up to 40% of Project cost (where toll collection prospects were low in uneconomic or backward areas). Actually both these earlier models were welcomed by construction community, but were discontinued by government because those good features relating to budgetary support to the project were putting financial pressure on short term budgeting and long term compulsions of financing.

This Hybrid combination of earlier ideas is presently welcome, when Infrastructure development has slowed down. However within 3-4 years, government financing may be stressed by necessary short term direct budgetary sup-port to Infrastructure and long term annuity commitment. This is inevitable due to upfront payments required, during execution and long term burden to be accepted in annual budgets for annuity payments over 15-20 years.

Also all nationalized banks' infrastructure related loan books are full or restricted due to either sectorial caps or non-performing loans. Hence though the terms of new HAM models are comforting to the banks, they may not have spare funds for at least 2-3 years to allocate to these hybrid projects which are likely to be awarded now and in the next financial year.

Though this new hybrid model lowers the responsibility of Contractor to 60% of project cost to raise the money, the question of sufficient promoter participation by Contractors with 25 to 30% equity component within 60% project cost will be expected by banks. This would mean arranging of 15 to 18% participation of overall project cost by promoters be-fore the balance amount of 40 to 45% are granted by public sector banks or financial institutions (private banks have mostly kept away from infrastructure loans).

It is well known that the balance sheets of most of the leading Infrastructure groups are stressed and over leveraged. They may not have the spare capacity to bring in equity participation in new projects, nor will the banks grant further project funding unless the balance sheets of these groups are deleveraged, by the existing projects or selling the stressed project assets. This will take some time (say 2 to 3 years).

This stress of new equity on Infrastructure groups can be eased; if banks/financial institutions agree to offer full borrowing of 60% of the project costs, since annuity payments are fully secured by government commitment in this HAM model (this really means banks giving loans to infrastructure groups due to government guarantee of annuity payment).

The other concerns expressed by financial experts is about pricing of these projects under HAM. Since Contractors taking up such project will have to line up promoter's equity and loan component of this project, keeping in mind project execution and long term O & M risks, apart from making profit on the promoter's equity, these projects may be priced up at least 25 to 30% more than the price obtainable under full EPC model. This will result into higher annuity payouts and matching higher values of toll which government will have to charge to recover high annuity payouts, which is committed to Promoters.

These expectations of high toll collection may not be easy to recover for any democratically elected government. Recently Government of Maharashtra has to closedown many small and medium size toll collection plazas due to popular political pressure and they are now struggling to compensate the private Concessionaire to honor` the contractual commitment made to those Special Purpose Vehicles (SPVs) created by private contractors.

The O & M payouts provided in this model are well identified in new MCA but the rates provided are modest. These amounts might be sufficient for maintaining really high quality road over long period of time. But the problems of quality of construction are complicated due to misuse by road users. It is a common knowledge that axle overloading by all heavy duty road carriers is rampant and axle over-loading up to even 30% is commonly noticed. The construction contractors have argued against this overloading as the cause of road damage and related repair costs, overshooting of O & M costs.

This dispute over appropriate causes for road repair costs during O&M period might become contentious issue in future. Since the O&M payments are modest, Contractors might delay or avoid carrying out proper and timely repairs to the road and make claims about heavy repair costs for reasons beyond their control, such as overloading of designed axle loads. Fortunately, O&M costs are delinked for annuity payment but failure in proper maintenance will attract penalties which might get disputed on the grounds of overloaded vehicles.

The broader issue of toll collection from public with their willingly cooperation is an unresolved problem. However government is well equipped to deal with law and order problem arising out of non-payment of toll by some sections of local community, than a private contractor (some attempts to convert toll into fuel surcharge has not worked since refueling of vehicles is chosen by user far away from toll points).

In recent past, existing companies operating under BOT model have reported toll leakage from 15 to 22 % due to demands from various pressure groups of end-users. The non-cooperation of frequently traveling local people is a well-known problem. The concept of paying end user charges for public utilities created by government or private agencies is not yet fully accepted in India.

Also, economically weaker sections of society cannot bear the full cost of service as they cannot afford it.

For readers who would like to know more about other changes in HAM model and its comparison with provisions in earlier BOT and Annuity models, a detailed risk allocation chart is prepared and attached below. It is conceded that no model (BOT/ Annuity/HAM) can be free from all risks, since executing Infrastructure projects is always about striking a fair balance of risk between the parties who can manage it best, with minimum cost burden.

As per shown in below table.

Risks	BOT Toll	BOT	Hybrid Annuity
Preconstruction			
a) Environment, forest clearances, Right of Ways	Responsibility of Handing over ROW on at least 80% of required area, Environmental protection& Conservations, Forest Clearances will be procured by the Authority.		
Construction Risk			
a) Cost overrun			
b) Time overrun	**Concessionaire to bear all risk**		
c) Quality			
Financing Risk			
a) Achieving Financial closure in time			
b) Financing cost overruns			
a) Interest Rate	**Concessionaire to bear all risk**		
b) Repayment			
c) Foreign Exchange			
Revenue			
a) Traffic volume	Shared by concessionaire & Authority. IF average Traffic volume falls below 2.5% of targeted traffic on targeted date (approx. 10 years after start of operations) Concession period is ex- tended by 1.5% per 1% of shortfall. If Actual traffic exceeds the targeted traffic by 1% the Concession period is reduced by .75%.	Not relevant	NHAI to take all risks
b) Toll leakages	Concessionaire to bear all risk	Not relevant	NHAI to take all risks
c) Tariff Rates	Tariff rates are decided as per National Tariff Policy. Hence there is no ambiguity involved. However revenue may reduce if the WPI does not rise as per original expectations of the Concessionaire.	Not Relevant	NHAI to take all risks
d) Competing road	Concessionaire to be compensated suitably if traffic exceed capacity	Not Relevant	NHAI to take all risks
Operations Risk			
a) Annual O&M			
b) Additional Periodic Maintenance	Concessionaire to bear all risk		
Economic Risks			
a) Taxes	Concessionaire to bear all risk		
b) Inflation			
Force Majeure (FM) events			
Time extension			
a) Before Financial closure (Appointed Date)	Time set forth for achieving Financial closure extended by time of FM event		

Risks	BOT Toll	BOT	Hybrid Annuity
b) Between Appointed Date and Commercial Operation date (COD)	Time set forth for Project completion extended by time of FM event Non-political FM: Respective parties to bear the costs. Neither party is required to pay other party		
c) After COD	Concession period extended by time of FM event	…	Concession period not ex-tended. But Concessionaire will continue to receive Annuity
Cost arising out of FM event			
a) Before Appointed date	Cost to be borne by Concessionaire & Authority respectively		
b) After Appointed Date	Non Political Event : Cost to be shared by respective parties Indirect Political event : To be shared Direct Political : Cost compensated by Authority		
Hand Over Risks			
a) Quality of Road	Concessionaire to bear all risk		
b) Default of Concessionaire	Pay 90% of Debts due at that time	Pay 90% of Debts due at that time	During Operations: 65% of debt due; During construction: 50% to 80% of debt due of 9% to 32% of Bid project cost which ever lower
c) Default of Govt. / NHAI	Pay all debts plus 150% of equity	Pay all debts plus150% of equity	Before COD : All debt due or 9% to 40.5% of PID Project Cost whichever lower plus 150% of equity; After COD: All annuity payments due till transfer date
Other risk			
a) Scope change during any stage	Authority to compensate if change cost increases beyond 0.25% of project cost.	Authority to compensate if change cost in-creases beyond 0.25% of project cost.	Authority to compensate costs fully

II. LITERATURE REVIEW

Edwin H. Chan, Maria C. Au

This states that the risk for a contractor in sudden increase of material rates as per not given with the risk transfer. Therefore, understanding the factors influencing the contractors pricing of contract risk is crucial for employers to optimize the cost effectiveness of risk allocation in contracts. The factors that contractors perceive to be important when they are pricing time related contract risk.

Aftab Hameed Menon, Ismail Abdul Rahman;

In Malaysian, traditional lump sum system, design and build/turnkey system says that the typical contractual relationship under traditional method in order to take the relation between client with contractor & consultant, and contractor with sub-contractor & supplier. Typical sequence of operations like brief, design, tender, construction. Management procurement:

client with main contractor & consultant and by the same time with workers. Operations of management procurement brief, design, construction.

Tejas C. Patil, Ashish P. Waghmare, P.S.Gawande

The rapid evolution of e-commerce in the past few years has introduced many ways for organizations to perform tendering process and participate in bidding. With a new conceptual techniques by reducing time and cost factor. Buying goods or services or engaging a contract for civil works like building roads, houses, and factories is an important activity. Contractor should develop their own planning, creation and administration in three steps they are:

- Planning department
- Contract creation department
- Contract administration department

Dr. Jim Mason, department of architect

It deals with the topic of Building Information Model with the pace of innovation and need to legal solutions and accommodate new approaches. Intelligent contracts work best were they are of short term or of instantaneous effect. The hypothesis advanced is that certain aspects of the construction contract cannot be fully intelligent and the best that can achieved in short to medium sale of contracts.

Fani Antoniou, Georgious N. Aretoulis

The choice of most appropriate contract type regarding the method of contractor compensation is one of the most essential and complex decision. In addition with the construction process s always technologically complex as it is comprised of numerous task and objectives.

Vladimir Obradovic, Petar Jovanovic

The implementation of this research is important to both project managers who wish to improve their performance and successes rate and organization in their human resource policy.

There is a very high positive correlation between emotional intelligence and professional success.

For recruiting staff to the position of project managers should consider the concept of emotional intelligence. But not only for the project managers has it also revealed to decide on human resource development program.

H. Randolph Thomas, Ralph D. Ellis

Many of the small or medium sized construction companies will show less interest on operational planning. Its better ti develop for prebid plans reduce costs and shorten schedules and improve labor productivity. The planning process consists of eight steps pressingly important for the growth of the company with high profits and minimizing of work load among the labors with their safety vision.

Yong-Cheol Yang, Chan-Jung Park, Ju-Hyung Kim &Jae-Jun Kim

For getting accuracy of work in the site done in the site of day to day progress. These can be done by the means of DPR under the progress of planning department in camp area to the office of client along with the pictures of construction. Through these the client can understand the condition of site in the office itself. But in these article it is explained for a multi- apartment building.

Unmesh. Y.Polekar, Rohit.R. Salgude.

It consists of proper planninng and scheduling is most efficient part in completion of project without time lagging and knowing in glance for the material required. And regular monitoring of the project will give satisfactory work for the workers and engineers working in that project. Mainly the planning office should know about the conditions corresponding to the respective manner by using some kind of software techniques.

Md Imran Khan, Maneeth P D, Brij Bhusan S

Its gives the information on the procedures adopted for recording, reporting & collecting information related to the performance of project by the use of DPR and MPR to estimate the progress stage of the project which have to be cross

checked by the prebid scheduling if any lagging of plan should be taken to the view of that engineer to give the corresponding reason and explanation for the delay of work.

Mr. Nilesh D. Chinchore, Prof. Pranay R. Khare

it deals with the construction equipment planning and its uses in very crucial time at which the time management may be rectified by a firm to continue its standards. With these the resource leveling and allocation for different kinds of works with multiple equipment to complete the project in means interval of time. Construction planning aims at identifying construction equipment for executing project task assessing equipment performance capability.

III. CONCLUSION

On collecting data from all aspects of contracts along with their merits and demerits from past years. Among all type of contracts HAM [Hybrid Annuity Model] is the best one to get competitive in present up growing world economy. Is a mix of both EPC (Engineering Procurement and Construction) and BOT (Build Operate Transfer) models? Under EPC model, NHAI pays private players to lay roads. The private player has no role in the road's ownership, toll collection or maintenance (it will be taken by the Government). Under BOT model, private players have an active role they build operate and maintain the road for specified number of year's say10-15 years. Before transferring asset back to the Government.

Now HAM combines EPC (40 per cent) and BOT (60 per cent). On behalf of the government NHAI releases 40%- 70%of total project cost. All kinds of loan clearance will be taken up by the government. According to different states they were giving % as say in Tamil Nadu is giving 50% as well Karnataka giving 75% (KESHIP) of the total project cost. As per the scope of emergency they were releasing the high percentages. Material escalation will also paid by the government.

From my regarding the HAM method is useful and efficient to attract all competitors in construction industry.

REFERENCES

[1] **Edwin H. Chan, Maria C. Au: (2012)** How to get the lowest estimate of a bid conformation, Open Journal of Business Management.

[2] **Aftab Hameed Menon, Ismail Abdul Rahman: (2017)** cost management in constructuion projects, International Journal of Civil Engineering and Built Enviroment.

[3] **Tejas C. Patil, Ashish P. Waghmare, P.S.Gawande: (2016)** tendering process in construction projects, IJISET March(2016)

[4] **Dr. Jim Mason, department of architect (2015)** new approaches while tendering process, IJISET July(2015)

[5] **Fani Antoniou, Georgious N. Aretoulis (2013)** different types of contract in highway projects, journal of civil engineering.

[6] **Vladimir Obradovic, Petar Jovanovic (2012)** role of project managers while tendering process, 26th IPMA world congress Crete, Greece.

[7] **H. Randolph Thomas, Ralph D. Ellis (2012)** functions of project management, International Journal Of Civil Engineering.

[8] **Yong-Cheol Yang, Chan-Jung Park, Ju-Hyung Kim &Jae-Jun Kim (2007)** daily work progress in construction projects, Journal of Construction Engineering and Management.

[9] **Unmesh. Y.Polekar, Rohit.R. Salgude (2015)** planning and scheduling in construction projects, International Journal of Advance Research in Computer Science and Management Studies.

[10] **Md Imran Khan, Maneeth P D, Brij Bhusan S (2008)** planning techniques in construction, Journal of Construction Engineering and Management.

[11] **Mr. Nilesh D. Chinchore, Prof. Pranay R. Khare (2014)** selection of equipment's for highway porjects. Journal of Engineering Research and Applications.

[12] **MORTH (Ministry of Road Transportation & Highways)** Revised on 2015.

[13] **IRC-SP:19-2001**, Indian Road Congress

Hamilton's Principle for Search of Invariants at Creation, Evolution and Destruction of Nanomaterials

Sergy Vasilievich Korotkevich

RUP «Gomelenergo», Gomel, 246001, Belarus

Abstract— *It is shown that the kinetics of the evolution of a structure of materials under external influences occurs in accordance with the minimum production of entropy and is characterized by a lower absolute value of a free energy. Using the extinction contours, the local curvature of the dispersed crystal lattice of nickel, the stress values and the dislocation density were quantitatively evaluated. Based on the provisions of mesomechanics and nonequilibrium thermodynamics, the positions of the kinetics of physicochemical, mechanical and tribological properties of the metal interface under contact interaction are developed. The substantiation of the search for invariants in the creation, evolution and destruction of nanomaterials from the symmetry properties of space and time under various external influences is given, which has scientific and practical significance.*

Keywords— time, space, invariants, dislocation structure; kinetics of nanostructure.

I. INTRODUCTION

Accumulated experimental data base does not allow using it to the fullest. The experimental data given in various sources differ from each other. On the one hand, this can be explained by some difference in the regimes and technologies for obtaining nanomaterials, as well as the conditions for their testing, and on the other hand, the lack of scientifically based fundamental principles and, as a consequence, the measurement parameters. The absence of scientific schools, the fragmentation of the directions of fundamental research and the purely practical approach to solving momentary applied problems, unfortunately, do not allow concentrating efforts on the classification and systematization of data in the fields of metal physics, tribochemistry, condensed matter physics and nanomaterial science. The results of plastic deformation studies are often controversial, and sometimes contradictory. The current state of the problem of the creation of nanomaterials is characterized as a transitional period between the accumulation of experimental data and their interpretation in the categories of mechanics, physics, chemistry and the development of generalizing invariant criteria that do not depend on regimes, conditions and technologies for obtaining them.

Improving the wear resistance of metal surfaces it is directly related to the establishment of hardening mechanisms, evolution and destruction of the structural elements constituting the material or a conjugate pair. It is necessary to create conditions under which the injection of frictional loading energy into the interior of the material and the amorphization associated with it will not result in the creation of developed porosity and friability, but the creation and slippage of submicro and nanostructural elements relative to each other. The creation and slippage of submicro and nanostructured elements and mechanisms of formation of a "lock" or the coupling of nanostructures and their conglomerates with respect to each other will allow not only designing block nanomaterials, but also to reduce their fragility and improve operational properties. In this connection, direct experimental studies of the kinetics of the structure at various scale levels are of great importance: macro, micro, submicro, and nano [1].

Another reason for not studying this issue is the conservatism of thinking associated with the dominant role of the fatigue theory of fracture, which does not take into account the energy relaxation processes accumulated in the material by, for example, flake-like sheets separation of friction wear particles [2]. The method of ferromagnetic resonance (FMR) has proved to be effective for studying the mechanism of flake-like sheets separation of wear particles, since changes in the resonance curve of the FMR reflect the kinetics of the microstructure of a thin surface layer [3]. The observed cyclicity of the strength characteristics of surface volumes at a multi-cycle and low-amplitude effect can be explained from the point of view of dislocation representations. On the rise of each cycle, as a result of the action of plastic deformation factors, two opposite processes occur in the subsurface volume: hardening due to the generation of new dislocations and partial softening associated with annihilation of dislocations of the opposite sign, the formation of polygonal structures and the flow of defects to the surface of microcracks. Probably, in the region of the tops of cycles, these processes balance each other. The areas of recession are caused by the relaxation of elastic stresses due to intense cracking. At this stage of the test, a strong dispersion of the crystal lattice of the surface layer is observed due to the formation of numerous microcracks, pores and other discontinuities in the continuity of the material [4]. The growth of cracks and their fusion into closed contours promotes

peeling of the dispersed layer. This destruction has a local, in time, character. Further repetition of the cycle is associated with the rise of the underlying layer [1].

The phenomenological model of a time-localized fracture mechanism has been developed, resulting in a cyclical peeling of the deformation of the surface layer of a metal under frictional loading of surfaces [5, 6]. Priority determined that, in contrast to the usual contact methods (rolling, compression), in the case of friction, the cyclic nature of the change in the strength parameters [7]. This periodicity of structural changes is established by the method of ferromagnetic resonance (FMR), electron microscopy and electron diffraction, X-ray diffraction analysis, and wear rate [1]. A set of experimental results showed that deformation dispersion and subsequent selective destruction of surface layers of metals under frictional loading are multilevel processes occurring at meso- and macro-scale levels and are mainly determined by the kinetics of the dislocation structure [1, 8]. Damascus steel has a high plasticity, strength and sharpness of the cutting edge, which is possible only when the graded structural-phase states form on the surface of solids. A special role here is played by the joints and boundaries of the polycrystalline grains.

Plastic deformation of solids is realized at several interrelated structural levels, the scale of which is determined by the nature of the structural defects responsible for the shaping [9]. In most cases, the distribution of localization zones is ordered in space and time, and the type of localization is determined by the law of plastic flow. The consideration of a solid body as a multilevel hierarchically organized system consisting of 3D-crystalline and 2D-planar subsystems causes a sharp increase in the role of the curvature of the crystal structure in describing the behavior of solids in fields of external influences [10]. All types of deformation defects can be represented as solitons of curvature of the crystal structure. The type of deformation defect is determined by the scale level of the curvature soliton [11].

The aim of the work is to develop theoretical and practical aspects of the creation, evolution and destruction of nano and submicrocrystalline structures and lubricating films on the surface of metals under external influences in the presence of surface and chemically active substances contained in plastic lubricants and oils of various nature and functional purpose for establishing physico- chemical and mechanical properties and regularities of their kinetics from the point of view of scale invariance of deformation, which together determined the conceptual development of new fundamental directions: to search for invariants in the creation, evolution and destruction, including, and nanomaterials; to increase the safety margin, operational reliability and durability of metal surfaces of machine components and mechanisms.

II. EXPERIMENTAL DETAILS

Let's give the concrete example. It is known that the formation of nanostructures in 3D material occurs under conditions of high contact pressures ≈ 6-12 GPa, realized, for example, in the case of equal-channel pressing and intense plastic deformation of the material [12, 13]. The nickel surface is 2D planar subsystem where the atoms are not bonded as firmly as in 3D crystal lattice. The surface of a solid is a structural defect already because of the asymmetric nature of the attraction of the atoms of the surface. This determines the basic physical and chemical properties of the surface of the material, due to free energy. The question arises about the possibility of forming nanocrystalline structures at low contact pressures (≈ 100 kPa) under conditions of accumulation of free energy by the metal surface [14]. In other words, is it possible to obtain structures with a high degree of misorientation and, accordingly, possessing unique properties at a pressure differing by five orders of magnitude? If so, what are the conditions for implementing this process?

Transformation of dislocation structure in the near-surface layer of nickel under friction loading has been studied by means of electron microscopy and ferromagnetic resonance. Polycrystalline nickel with purity of 99.9 % has been examined. Samples in the form of thin disks (5 x 0.1 mm^2) were electrolytically polished and annealed in vacuum (0.133 MPa under 973 K) [1]. Friction test was carried out by means of a machine of type AE-5 with precision positioning of contact surface. Sliding friction was performed in pair Ni – Mo in air and lubricant CIATIM – 201 under load of 82.3 kPa and linear velocity of 0.5 m/s. Number of working operating strokes was in the range of $1 – 36 \cdot 10^3$. Average volume temperature of the sample didn't exceed 40 $^{\circ}C$. Range of ferromagnetic resonance was registered by means of method described in the monograph [1]. Electronic and microscopic researches of nickel were carried out by the instrumentality of microscope ЭМВ – 100АК and S-806 Hitachi by means of thin foils «for transparency». Foils were obtained by means of single-sided electrolytic thinning of disks at the opposite side of the friction surface at the installation of jet-stream polishing, equipped with sensitive photodiode bridge, which makes it possible to control transparency of areas at the depth of ≈ 0.1 micrometers from the friction surface [1].

III. RESULTS AND DISCUSSION

The principle of least action or Hamilton principle can be understood in a narrow and broad sense. In the narrow sense, this principle means energy advantage, i.e. the kinetics of the evolution of the structure of materials under the influence of

external influences, proceeds in accordance with the minimum production of entropy and is characterized by a lower absolute value of the free energy (Figure 1).

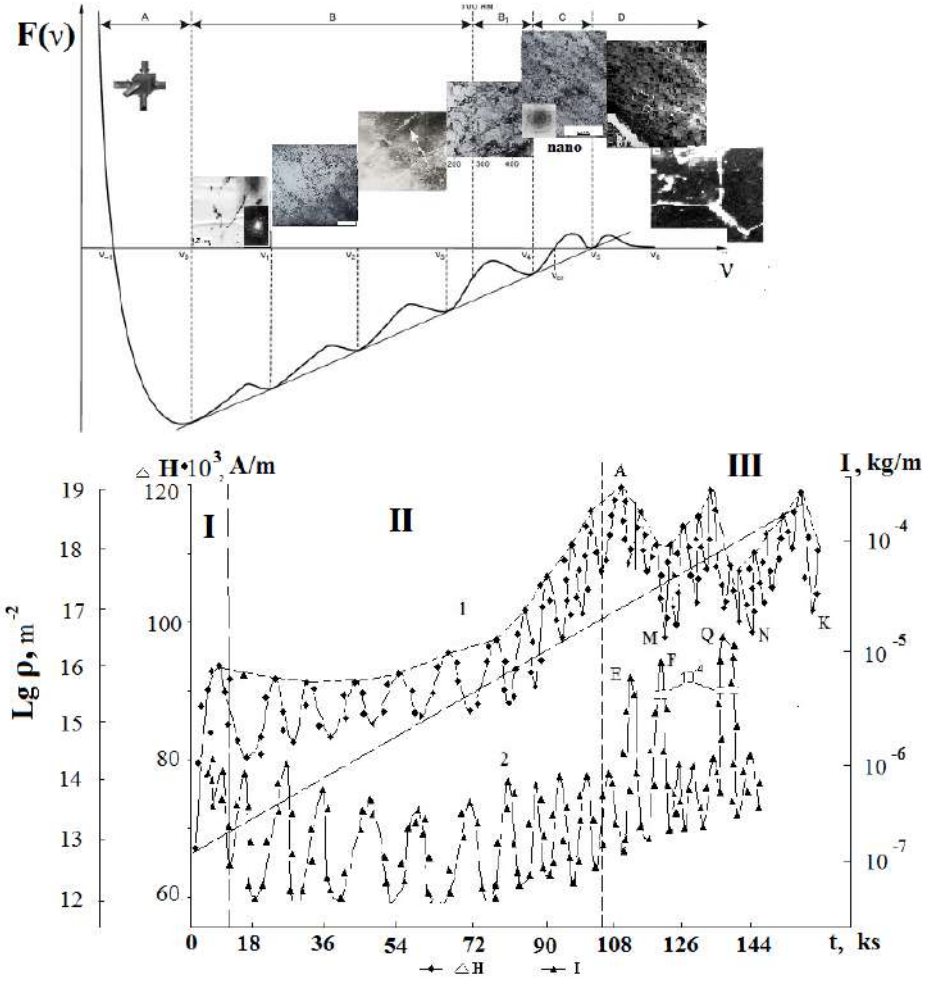

FIGURE 1. Dependences of the Gibbs potential (F(ν)), dislocation density (ρ) and wear (I) on the friction time (t).

A distinctive feature of the appearance of nanocrystalline structures (Fig. 2) with friction (≈ 84 kPa) from the occurrence of intense plastic deformation (6–12 GPa) is that they are already beginning to form at a relatively short time t = 0.6–0.9 ks (Fig. 1) at the stage of the first cycle of surface hardening in the presence of surface and chemically active substances contained in the lubricant CIATIM-201.

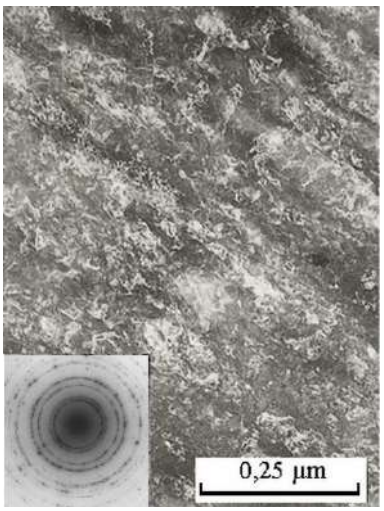

FIGURE 2. Nanostrucrure (t = 0.9 ks)

The primary flows of structural transformations in a deformed polycrystalline of nickel develop in a 2D planar subsystem in which there is no translational invariance. The distribution of normal stresses in the boundary of disoriented polycrystalline grains is described by a sinusoidal function that is, alternating regions of tensile and compressive stresses [15, 16]. With this development of grain boundary sliding in the zones of tensile normal stresses, clusters of positive ions arise which are shielded by an electron gas from the nearest environment in the border zone of the 3D crystalline grain. A decrease in the concentration of free electrons between ions causes an increase in their interionic distance and the appearance of a localized gap in an electron-energy spectrum [17]. This is equivalent to the appearance in the system of a quantum dot, which creates its own "impurity" electronic states in the local energy gap of an electron-energy spectrum. As a consequence, bifurcation minima of the multiparticle interaction of potential arise in interstices.

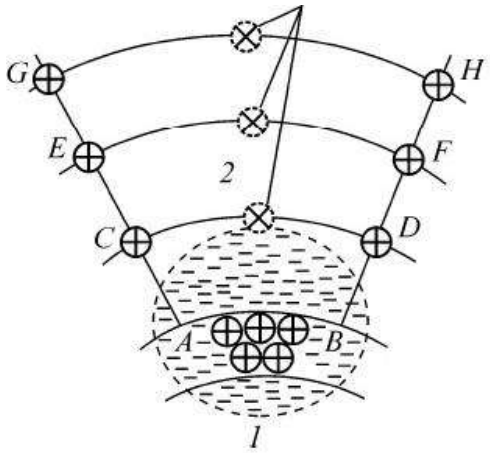

FIGURE 3 – Generation of bifurcation interstitial structural states in the zone of local curvature of the crystal lattice, where AB are clusters of positive ions on the grain boundary 1 and 2

Displacement atoms in the vapor during the development of the shear deformation will be accompanied by plastic distortion in the region of the bifurcation of interstitial minima multiparticle potential that causes a local plastic flow vorticity. The expression for the vorticity of a localized plastic shear was obtained in [18] and has the form:

$$\chi_{\nu}^{\beta} = \varepsilon_{\mu\chi\delta}\,\partial/ox\left(E_{\nu}^{\beta} - P_{\nu}^{\beta}\right)\frac{C_{\alpha\beta}^{\mu\nu}}{E} \tag{1}$$

where $\varepsilon_{\mu\chi\delta}$ – is Levi-Civita symbol, the expression representing the relaxation of shear stresses by the mechanism of plastic distortion P_{ν}^{β} in the zones of local curvature of the crystal lattice is presented in parentheses. Taking into account the curvature of the crystal lattice in the entire volume of the deformed solid body necessitates the construction of a nonlinear mechanics of plastic deformation and fracture.

The formation of bifurcation interstitial structural states and the development of the effects of plastic distortion are enhanced under conditions of intense plastic deformation, when the curvature of the crystal structure is strongly pronounced [19–21]. Particular attention is paid to the problem of wear of materials by papers in the field of grinding the structure of materials with their equal-channel angular pressing [21] and friction welding with mixing [21]. Under conditions of equal channel angular pressing, the curvature of the crystal structure is formed throughout the cross section of the preform, in the interstitial spaces of which plastic distortion processes develop with the formation of a large concentration of vacant sites of the crystal lattice. Their multilevel coalescence causes fragmentation of the initial structure at the meso- and nanoscale structural levels. The formation of a submicrocrystalline structure (0.1–0.5 μm) obtained by intense plastic deformation, for example, equal-channel angular pressing, extrusion causes a significant increase in the stress of cyclic hardening, the endurance limit under multicyclic loading, and a decrease in the characteristics of cyclic crack resistance [22]. This is due to an increase in the density of dislocations and a decrease in the grain size. In view of the high gradient of the properties of the two-phase (crystal and its boundaries) nanocrystalline state, the formed structures are nonequilibrium with a high concentration of defects and their properties are described from the standpoint of nonequilibrium thermodynamics and nonlinear mechanics [23]. It should

be noted that dynamic recrystallization occurs under conditions of high curvature up to 1000 deg / μm of the crystal lattice and high local stress microconcentrators and their gradients. Fragmentation of the crystal lattice into nano- and ultrafine-grained structural states is realized by collective dislocation-disclination relaxation of the micromoentions by mutual shifts and rotations as a whole of meso- volumes larger than 1 μm. The realization of the collective rotational mode of deformation is carried out at several scale levels and includes the following basic mechanisms: the formation of the fragment boundaries, namely, submicrogerene with variable misorientation vectors or high density of partial disclinations as a result of the relaxation of micromotions; the formation of localization bands of non-crystallographic shear with high-angle misorientations at the boundaries of meso-volumes; the formation of elements of the nanocrystalline structure in the zones of intense shear and rotations [23].

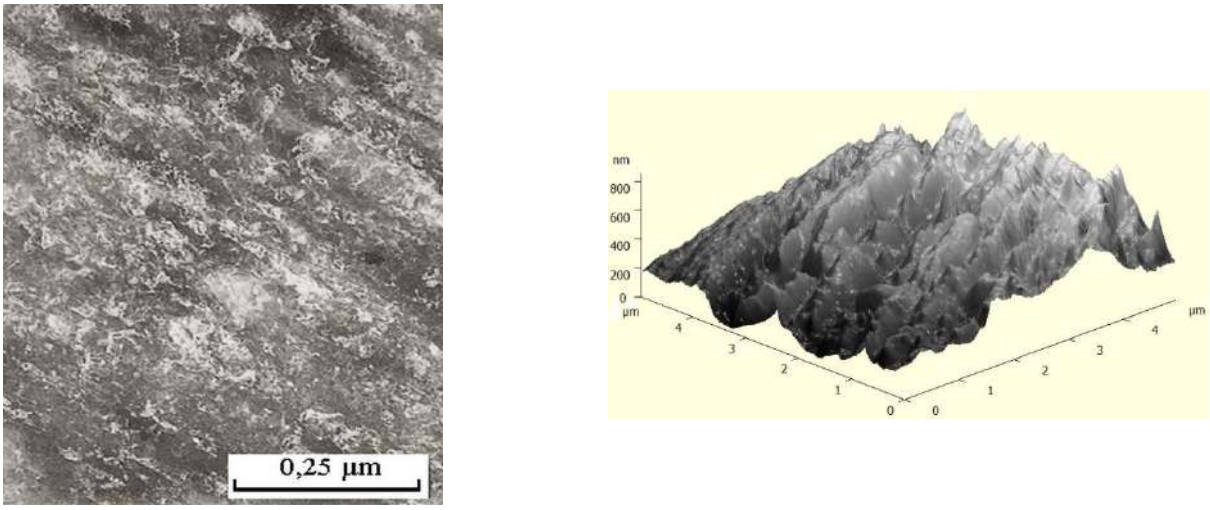

(A) (B)

FIGURE 4. A - nanostructure; B - AFM image of the surface of nickel with nanostructured formations.

Nanocrystalline structures have a size of ≈ 5–50 nm with a high-angle misorientation of the cell boundaries ≈ 5–10° [24]. It can be assumed that under conditions of nonequilibrium deformation and nonlinear dynamics of structure formation, when the rate of increase in stresses exceeds the rate of their relaxation, the formation of dislocations on the surface of nickel during friction and the facilitated exit to the surface in the presence of surface and chemically active substances are present. The high dislocation density $\rho \approx 10^{16}$ m^{-2} ensures their convergence and splitting, which is accompanied by an increase in the local curvature of the crystal structure.

It can be argued that these nanostructures are formed not only in the presence of high contact pressures, causing intense plastic deformation, but also in conditions of nonequilibrium deformation (region I in Fig. 1), where the sources of failure, namely slip bands, microcracks, twins, pores, vacancies are not present. There are no mechanisms of energy relaxation yet. The only possible mechanism for splitting dislocations and the formation of nanostructures on the surface of nickel are realized. There is a principle of least action or the greatest energy efficiency at the maximum possible result namely the formation of nanostructures (Figure 4) [14].

Consider the transition of the system from one equilibrium state to another (Figure 1). For example, the material under the influence of external influences passes from the state "A" (the original crystal of the metal, which has the translational invariance of the crystal lattice) to the state "B" (the nanostructured state), while the necessary condition for the transition to a new structural state is that, that the value of the energy difference $\Delta H = H_{max} - H_{min}$ should be sufficient to create a new structural state. The material structure passes from one state, for example, "A" to state "B" (Figure 5) in accordance with the principle of least action [25]. Once the amount of energy injected into the system (material) is sufficient to form a new structural state, it is formed in accordance with the principle of least action.

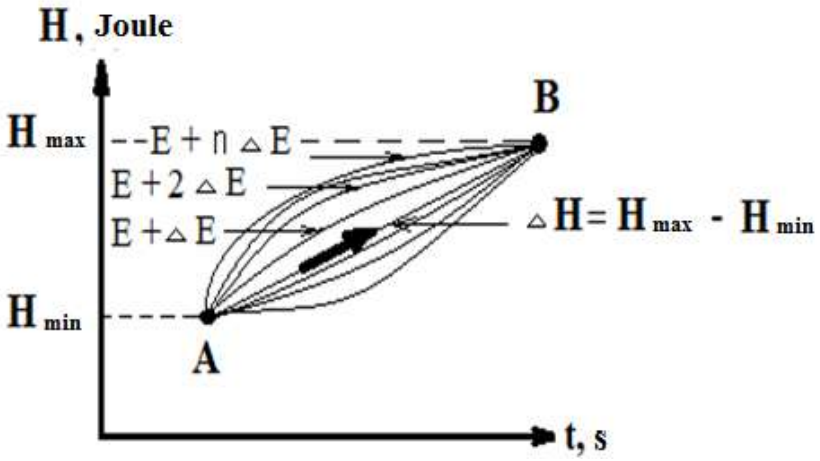

FIGURE 5. Kinetics of the transition of a system from one structural state (A) to another (B) in accordance with the principle of least action.

The system or material tends to move to a new structural state in accordance with the principle of least action, characterized by a decrease of free energy.

In a broad sense, the use of the principle of least action means the search for invariants in the creation, evolution and destruction, including, and nanomaterials.

It is known that the principle of least action (S) at moving a material point from one position to another during a time interval $\Delta t = t_2 - t_1$ can be written in the form [25]:

$$\delta S = \delta \int_{t_1}^{t_2} L\,(x, v, t)\,dt = 0\,, \tag{2}$$

where x – is the generalized coordinate, v – is the generalized velocity, t – is time, and L (x, v, t) is the Lagrange function.

Assume that the kinetic structural change material, with the transition from state «A» to state the structure of the structure «B» can be written as:

$$\delta S = \delta \int_{t_1}^{t_2} L\,(x, \chi, t)\,dt = 0\,, \tag{3}$$

where x – is the generalized coordinate, χ – is the curvature of the crystal lattice, and t – is the time.

The analysis of literary data in the field of tribology, condensed matter physics, and nanomaterial science testifies mainly about their experimental character. The level of our understanding is currently aimed at solving applied problems and does not allow us to develop fundamental principles for meaningful evolutionary development, both in the field of condensed matter physics, tribology, and in the development of nanomaterials.

Conservation laws are invariants in physics [25]. An invariant is a property that remains unchanged under transformations of a certain type. In kinetic processes, an invariant is a physical quantity whose value in some physical process does not change with time. They are performed in a closed reference system or where the projection of their vector quantities is stored in the field of action of forces on the direction, where their magnitude does not change.

Processes of contact interaction of solids and the creation of nanomaterials under external influences proceed in the same space-time continuum, with the same properties (from the homogeneity of time, the law of conservation of energy follows, from the homogeneity of space - the law of conservation of momentum, from the isotropy of space - law conservation of the angular momentum) and are accompanied by heat exchange [25]. Does this mean that since the system is not closed, then the conservation laws and invariants in it are absent or are all forms of energy dissipation and the fulfillment of the energy balance not only possible but also an objective reality? Therefore, the existence of invariants when acting on a tribosystem or material follows from the fact that it itself is part of a space-time continuum with certain properties. Since the modern stage

of understanding the processes occurring at the interface between metals and materials under external influences does not allow us to fully clearly formulate invariants, we can only assume the direction of their search and the ways of development.

The homogeneity of space and the law of conservation of momentum it will correspond to the invariant associated with the geometric parameters of the material structure when it is *created*, for example, the conservation of the scale invariance of the curvature of the crystal lattice of the metals, a particular manifestation of which is the formation of an equilibrium roughness in the friction of conjugated bodies in accordance with the Le-Satelier–Brown [26].

It is known that initially nickel has a translationally invariant crystal lattice with a low dislocation density $\rho = 10^{12}$ m^{-2} and a curvature of the crystal lattice $\chi \approx 0$ degrees / nm. Each half-cycle of hardening corresponds to a half-cycle of destruction (Figure 1), and the region of compression of the material corresponds to a stretching area similar to a chessboard [15, 16]. Like Heisenberg's uncertainty principle in quantum mechanics in nanomaterial science (the smaller the size of the nanostructure, the larger the size of the amorphous "coat" surrounding it), we can assume that the product of two physical parameters is a constant value [27]. As one physical parameter, the curvature of the crystal lattice χ can be chosen, which increases in proportion to the dislocation density (Fig. 1), and as another parameter one can choose a parameter that decreases accordingly, that is, it is in antiphase. In this particular case (Figure 1), this is the rate of destruction (this may be the area of pores, discontinuities, cracks, etc.) or wear. Then we can assume that the product of these two parameters has the form:

$$\left(\sum_{i=1}^{N} \chi_i\right) \times I = const \tag{4}$$

where χ_i – is the local curvature of the crystal lattice at the i-th mesoscopic level, and I – is the wear rate.

The homogeneity of time and the energy conservation law associated with it will correspond to a certain structural state formed under external influences. Here it is necessary to note the special role of time in the *evolution* of the material at the formation of highly excited energy states, namely, how long this material will be in this state. The definite content of the exciton material corresponds to a definite form expressed in the elements of plastic distortion. The transition of atoms to the interstices of the crystal lattice under external action and the formation of bifurcation states by them provides the spectrum of excited states of the electronic subsystem and nuclei [28]. The definite content of the exciton material corresponds to a definite form expressed in the elements of plastic distortion. Using the method of electron transmission microscopy, it is established that after the expiration of a time period of forty years, extinction circuits (fig. 6, a, b, arrows) with high stresses (up to 300 GPa) and plastic distortion elements are clearly preserved and do not dissociate (fig. 6, c, arrow). But does this form correspond to its energetic state or content? On the one hand, there is superplasticity and amorphous (like liquid) state of the material, expressed in plastic distortion elements, for example, circles on the water, and on the other hand circles on the water (or elements of plastic distortion) completely relax in time, which cannot be said about the elements plastic distortion (fig. 6, c, arrow).

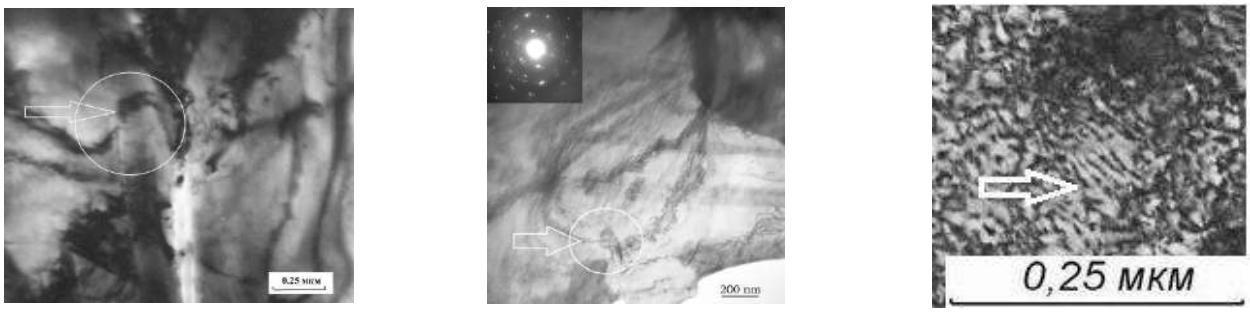

(A) **(B)** **(C)**

FIGURE 6. A) and B) The extinction circuits at curvature of the crystal lattice of the metals; C) The elements plastic distortion

The plastic components of the amplitude of internal stresses in bending and torsion are calculated by formulas [29, 30]:

$$\sigma_{11,n\prime} = E\sqrt{b\chi_{11,n\prime}} \tag{5}$$

$$\sigma_{12,пл} = E\sqrt{b\chi_{12,пл}} \quad (6)$$

where E – is the modulus of elasticity; b – is the Burgers vector, and χ – are the components of the curvature-torsion tensor of the crystal lattice.

The width of the contour can be represented in terms of the components of $\Delta L_{пл}$ and, respectively, on the OX and OY axes of the Descartes coordinate system. The plastic components of the curvature-torsion gradient at the bending and torsion χ of the crystal lattice, respectively, are determined by formulas:

$$\chi_{11,пл=\frac{\Delta\varphi}{\Delta L_{ox,пл}}} \quad (7)$$

$$\chi_{12,пл=\frac{\Delta\varphi}{\Delta L_{oy,пл}}} \quad (8)$$

where Δφ – is the angle of misorientation on the width of the contour ΔL; ΔL – is the width of extinction contour.

The quantitative estimation of the local curvature of the crystal lattice of the nickel surface, the plastic components of the internal stress amplitude for bending $\sigma_{11} \approx 0.6 \cdot 10^{11}$ Pa and torsion $\sigma_{12} \approx 0.9 \cdot 10^{11}$ Pa is comparable with the magnitude of the nickel elasticity modulus $\approx 2 \cdot 10^{11}$ Pa, which indicates a loss elastic properties, the accumulation of energy deformation and the destruction of the surface.

I estimated the dislocation density using expression [31]:

$$\rho = \frac{1}{b}\chi \quad (9)$$

where b – is the Burgers vector of dislocations, χ – is the disorientation gradient equal to the curvature-torsion of the crystal lattice. The dislocation density is $\rho + - \approx 10^{18} - 10^{19}$ m^{-2}.

Fragmentation of the initial structure of the material causes a strong thermodynamic disequilibrium of the surface layer of the material during the contact interaction. When the stresses are reached $\approx 1 \cdot 10^{11}$ Pa, the nickel crystal lattice loses its resistance to shear $\approx 0.77 \cdot 10^{11}$Pa. The amorphous layer with unique physicomechanical properties is formed.

It is of interest to determine the contribution of the hardening mechanisms by the formula [31]:

$$\sigma_{\Sigma} = \sigma_{тр} + \sigma_{тв} + \sigma_{з} + \sigma_{Op} + \sqrt{(\sigma_{д}^{2} + \sigma_{л}^{2})} \quad (10)$$

where $\sigma_{з}$ – grain boundary hardening. where $\sigma_{тр}$ is the frictional stress of dislocations in the Ni crystal lattice; $\sigma_{тв}$ – hardening of the Ni sample by the atoms of the alloying elements (C, Mn, V, etc.); $\sigma_{л}$ – hardening by forest dislocations, which cut sliding dislocations; $\sigma_{Д}$ – hardening by internal long-range stress fields; σ_{Op} – hardening by incoherent particles when they are traversed by dislocations by the Orovana mechanism (dispersive hardening); $\sigma_{з}$ – hardening due to grain boundaries.

The most significant contribution to hardening of the nickel surface is made by hardening due to the interaction of long-range stress fields ($\sigma_{д}$). The magnitude of the stress $\sigma_{л}$ corresponds to a charged dislocation ensemble of dislocations and is estimated by electron microscopy using flexural extinction contours [31]:

$$\sigma_{д} = m \cdot \alpha_{c} \cdot G \cdot b \cdot \sqrt{\rho_{+-}} \quad (11)$$

where α_{c} = 0,5 – is the Strunin coefficient; m – is the orientational factor, or Schmid factor [31], m = 2.2; α – is a dimensionless coefficient that varies within the range 0.05–0.6, depending on the type of dislocation ensemble (we shall take it equal to 0.25 [31]); G = 78 GPa – is the shear modulus of the matrix material, b = 0.35 nm – is the lattice constant of nickel; ρ – is the average value of the scalar density of dislocations.

The external contact action on the nickel surface at a very long friction time t = 108 ks and more in the presence of surfactants contained in the plastic lubricant CIATIM-201 leads to the formation of a highly developed dispersed submicrostructure, which causes the interaction of long-range dislocation fields (≈ 70 nm) polarization of the dislocation structure, which is reflected in the appearance of extinction loops. The quantitative estimation of the curvature-torsion

parameter from the analysis of the images of the extinction loops in Figures 6, a and b shows that it is up to $\chi = 3$ degrees / nm at a voltage up to $\approx 3 \cdot 10^{11}$ Pa.

The oscillating kinetics of hardening and destruction of amorphous layer takes place at superplastic.

I estimated the energy density using expression [30]:

$$\Delta U = \frac{1}{4E}[(1-\nu)]\sigma_{11}^2 + 2\sigma_{12}^2 \quad (12)$$

where ν – is Poisson's coefficient, and the remaining parameters correspond to the parameters described above in expressions 3 and 4.

Accumulated energy under friction in local areas with a large curvature of the crystal lattice reaches $\approx 17 \cdot 10^9$ Joule. Coalescence of nano and submicropores into micropores leads to a viscous destruction of the surface layer of the material. There is a time-localized selective mechanism for the destruction of the surface layer, the fundamental role in which is determined by the multilevel curvature of the crystal structure of the surface layer [5, 6].

The isotropy of space and the law of conservation of angular momentum associated with it can be compared the invariant associated with the mechanisms of deformation and *fracture* of the surface of tribosystem or material at all mesoscopic structural-scale levels of deformation [27]. A possible implementation mechanism will be implemented through intergranular shift, relative rotation and slip [1, 6]. According to the law of conservation of the angular momentum, the macro-rotation must be compensated by the sum of all rotations in the hierarchy of mesoscale levels of deformation. This law is defined by the expression [28, 32]:

$$\sum_{i=1}^{N} rotJ_i = 0 \quad (13)$$

where I_i - fluxes of defects at the i-th mesoscopic level. The formation of defect fluxes I_i is a kinetic process that requires a periodic crack stop to bring the material state before the crack tip to the critical level of the nanostructured states.

It is necessary to note the dominant role of the nanostructural level in the hierarchically organized phenomenological model of destruction [33]. The output of dislocations on the surface of metals in the form of steps leads to the rise of the Kelvin probe, which causes an increase in the contact resistance [33]. The dependence of the tunneling conductivity on the nanometer thickness of the boundary lubricating layer makes it possible to diagnose the operating modes of the rolling and sliding bearings, which increases the reliability of their operation [34, 35].

IV. CONCLUSION

Thus, on the basis of mesomechanics and nonequilibrium thermodynamics, as well as the properties of space and time, the positions of the kinetics of the physicochemical, mechanical and tribological properties of the interface of metals under contact interaction have been developed, namely:

- Each stable state of the metal interface will have its own structure with a certain value of free energy and, accordingly, with the kinds of its redistribution between the elements of the boundaries and within the structural formation;
- The system tends to occupy a position or form a structure of the interface, which corresponds to the minimum thermodynamic potential of Gibbs;
- If the effect of the load-velocity parameters or external action exceeds a certain critical value that has entered the energy system, it goes into a new structural state with a minimum production of entropy and is characterized by a lower value of the free energy;
- The system tends to shift to a new structural state in accordance with the scaling of the local curvature of the crystal lattice at all structural-scale levels of plastic deformation and destruction of the metal surface;
- based on the analysis of the basic properties of space and time, the principle of least action is proposed for analyzing the kinetics of structure formation and the search for invariants in the *creation*, *evolution* and *destruction* of

nanostructured materials under various external influences and the determination of kinetic regularities and their physicochemical and mechanical properties that have scientific and practical value.

The proposed approach requires further development and reflection.

ACKNOWLEDGEMENTS

Thanks to professor V.G. Pinchuk and academician of RAS, professor V.E. Panin for research support.

REFERENCES

[1] V. G. Pinchuk, S.V. Korotkevich. Kinetics of Strengthening and Destruction of Metal Surface at Friction, Saarbrŭcken: Lambert Academic, 2014, 180 pp.

[2] Suh, N.P. The Delamination Theory of Wear / N.P. Suh // Wear. – 1973. – Vol. 25, № 1. – P. 111 – 124.

[3] Pinchuk, V. G. Microstructure and Strength Properties of Submicro and Nanocrystalline Nickel under Friction / V. G. Pinchuk, S. V. Korotkevich // Modeling and Numerical Simulation of Material Science. – 2013. – № 3. –P. 8–13.

[4] Pinchuk, V. G. Microstructure evolution in friction-loaded layers of nickel / V.G. Pinchuk, S.V. Korotkevich // Indian Journal of Research . – Vol. № 4, issue № 2. – 2015. – P. 8–10.

[5] Pinchuk, V. G. Physical patterns of dislocation structure kinetics in friction loaded surface layers / V. G. Pinchuk, S. V. Korotkevich // Global Journal For Research Analysis. – № 4, issue № 5. – 2015. – P. 255–257.

[6] Pinchuk, V. G. / Kinetics of Microstructure and Selective Mechanism of Fracture of Metal Surface Layer under Friction / V. G. Pinchuk, I. A. Buyanovskiy, S. V. Korotkevich // Inorganic Materials: Applied Research. – 2015. – Vol. № 6., № 5. – P. 355–359.

[7] Moser, B. Cyclic strain hardening of nanocryslline nickel / B. Moser, T. Hanlon, K.S. Kumar // Scri. Mater. – 2006. – V. 54, № 6. – P. 1151 – 1155.

[8] Panin, V.E. Physical mesomechanics of destruction and wear on the surfaces of friction of solids / V.E. Panin, P.A. Vityaz // Physical mesomechanics. – 2002. – V. 5, № 1. – P. 5–13.

[9] Panin, V.E. Physical mesomechanics of a deformed solid body as a multilevel system. I. Physical foundations of the multilevel approach / V.E. Panin, V.E. Egorushkin, A.V. Panin // Physical mesomechanics. – 2006. –V. 9, № 3. – P. 9–22.

[10] Panin, V.E. The fundamental role of the curvature of the crystal structure in plasticity and strength of solids / V. E. Panin, A.V. Panin, T. F. Yelsukova, Yu. F. Popkov // Physical mesomechanics. – 2014. – V. 17, № 6. – P. 7 – 18.

[11] Panin, V.E. Fundamental role of local curvature of crystal structure in plastic deformation and fracture of solids // Physical Mesomechanics of Multilevel Systems 2014: AIP Conf. Proc. – 2014. – V. 1623. – P. 475–478.

[12] Evolution of nickel microstructure under deformation by torsion under pressure / Ditenberg IA [and others] // Physical mesomechanics. – 2012. – V. 15, № 5. – P. 59–68.

[13] Glezer, A.M. Conditions for the formation of various defect structures in the process of large plastic deformations. Glezer, V.A. Pozdnyakov // Deformation and destruction of materials. – 2005. – № 4. – P. 9–15.

[14] Korotkevich, S. V. Features of the formation of nanocrystalline structures on the surface of polycrystalline nickel under friction / S.V. Korotkevich, M.S. Korotkevich // Actual problems of strength: materials of the 60th international scientific conference. – Vitebsk, 14–18 мау, 2018. – P. 114–116.

[15] The effect of the "chessboard" in the distribution of stresses and strains on interfaces in a loaded solid body // DAS.– 2006. – V. 409, № 5. – P. 1–5.

[16] Panin, V.E. "Chess" meso-effect of the interface in heterogeneous media in fields of external influences / V.E. Panin, A.V. Panin, D.D. Moiseenko // Physical mesomechanics. – 2006. – V. 9, № 6. – P. 5–15.

[17] Kashchenko, M.P. Couples of inversely populated electron states in the optimal energy range for the generation of waves / M.P. Kashchenko, N.A. Skorinova, V.G. Chaschina // Izv. High schools. Physics. – 2005. – V. 48, № 5. – P. 44–48.

[18] Egorushkin, V.E. Gauge dynamic theory of defects in inhomogeneously deformed media with a structure. Behavior of the interface / V.E. Yegorushkin, "Izv. High schools. Physics.– 1990. – V. 33, № 2. – P. 51–68.

[19] Panin, V.E. Nonlinear wave processes in a deformed solid body as multilevel in a hierarchically organized system / V.E. Panin, V.E. Egorushkin, A.V. Panin // Physics Uspekhi. – 2012. – V. 182, № 12. – P. 1351–1357.

[20] Panin, V.E. Solitons of curvature as generalized wave structural carriers of plastic deformation and fracture / V.E. Panin, V.E. Egorushkin, A.V. Panin // Physical mesomechanics. – 2013. – V. 16, № 3. – P. 7–26.

[21] Panin, V.E. Fundamental role of local curvature of crystal structure in plastic deformation and fracture of solids // Physical Mesomechanics of Multilevel Systems 2014: AIP Conf. Proc. – 2014. – V. 1623. – P. 475–478.

[22] Holste, C. Cyclic plasticity of nickel, from single crystals to submicrocrystalline polycrystals / C. Holste // Philosophical Magazine. – 2004. – V. 84, № 3–5. – P. 299–315.

[23] Panin, V.E. Physical mesomechanics and nonequilibrium thermodynamics as a methodological basis of nanomaterial science / V.E. Panin, V.E. Egorushkin // Physical mesomechanics. – 2009. – V. 12, № 4. – P. 7–26.

[24] Pinchuk, V. G. Evolution of the submicro and nanostructure of nickel surface layer under friction loading] / V. G. Pinchuk, S. V. Korotkevich, D.N. Garkunov // Materialovedenie. – 2013. – № 6. – P. 39–44.

[25] Landau, L.D. Theoretical physics in ten volumes. V. 1 Mechanics / L.D. Landau, E.M. Lifshits. - Moscow: Science. – 1988. – 215 pp.

[26] Dotsenko, A.I. Fundamentals of tribotechnics / A.I. Dotsenko, I.A. Buyanovsky. – M.: INFRA-M. – 2014. – 336 pp.

[27] Lifshits, E.M. Theoretical physics. Theoretical physics. T.10. Physical kinetics / E.M. Lifshits, L.P. Pitaevsky. – Moscow: Science. – 1979. – 527 pp.

[28] Multiscaling of Lattice Curvature on Friction Surfaces of Metallic Materials as a Basic of Their Wear Mechanism / V.E. Panin, V.G. Pinchuk, S.V. Korotkevich, S.V. Panin // Physical Mesomechanics. – Vol. 20, № 1. – 2017. – P. 69 – 77.

[29] Evolution of the contributions to the plastic component of internal stresses of the components of the bending and torsion of the crystal lattice in austenitic steel / S.F. Kiseleva, N.A. Popova, N.A. Koneva, E.V. Kozlov // Materials Science. – 2016. – № 7. – P. 24–26.

[30] Determination of the energy density stored in the plastic deformation of an isotropic body by the curvature-torsion of the crystal lattice / Koneva, S.F. Kiseleva, N.A. Popova, E.V. Kozlov // Fundamental problems of modern materials science. – 2011. –V.8. – № 3. – P. 34–41.

[31] Effect of equal-channel angular pressing on the structure and yield strength of 10G2FT steel / E.V. Kozlov [and others] // Deformation and destruction of materials. – 2016. – № 3. – P. 10–14.

[32] Panin, V.E. Deformable rigid body as a nonlinear hierarchical organized system. Panin, V.E. Egorushkin // Physical mesomechanics. – 2011. – V. 14, № 3. – P. 7–26.

[33] Interrelation of the microstructure of the surface layer of metals, the thickness and character of the adsorption of the boundary lubricating layer with wear. Korotkevich [and others] // Technology of metals. – 2016. – No. 7. –P. 16–22.

[34] Korotkevich, S.V. Nondestructive testing of rolling bearings / S.V. Korotkevich // International Journal of Scientific Research. – 2017. – Vol. 6, issue 12. – 2017. – P. 478–484.

[35] Korotkevich, S.V. Nondestructive testing of sliding bearings / S.V. Korotkevich, N.F. Solovej, A.S. Shantyko // International Journal of Environmental and Agriculture Research. – 2018. – Vol. 4, issue 3. – 2018. – P. 59–71.

Study of high-mobility thin films containing highly crystalline single-walled carbon nanotubes

Norihiro Shimoi[1], Kazuyuki Tohji[2]

Graduate school of Environmental Studies, Tohoku University, 6-6-20 Aoba, Aramaki, Aoba-ku, Sendai 980-8579, Japan

Abstract**—** *While data from various devices as Internet of Things (IoT) are scattered and isolated as silos at present, some expect that hundreds of billions of devices will be connected through the Internet by the early 2020s. To prevent radio interference of huge amounts of data, it is necessary to develop ubiquitous wearable devices that enable constant retention and sharing of data. We aim to establish the basic packaging technology for realizing the semiconductive thin films and circuits that make up such electronic devices, and we fabricated thin films using highly crystalline single-walled carbon nanotubes (HC-SWCNTs) by a wet-coating process and evaluated their electrical properties in this study. Our research has developed a technology to disperse HC-SWCNTs without impairing their crystallinity and succeeded in fabricating thin films from a dispersion liquid of HC-SWCNTs obtained by this technology. We also evaluated the Hall mobility of these thin films and found that a high Hall mobility of 1,000 cm2/Vs can be achieved by controlling the crystallinity. On the basis of the results of this study, we will pursue our research to establish a technology for packaging electronic circuits that take full advantage of the electronic properties of HC-SWCNTs by a wet-coating process.*

Keywords**— single-walled carbon nanotube, high crystallization, IoT, Hall mobility, thin film.**

I. INTRODUCTION

As more electronic devices around us become compatible with the Internet of Things (IoT), networks are being constructed to share information among various devices. While data from various devices are scattered and isolated as silos at present, some expect that hundreds of billions of devices will be connected through the Internet by the early 2020s. Although huge amounts of data and information are constantly generated, they cannot be shared as long as they are isolated as silos. To deal with this issue, it is necessary to develop wearable devices that enable constant retention and sharing of data [1]. Namely, it is desirable to realize wearable electronic devices having nonconventional functions [2-4], such as flexibility that renders them foldable or windable, a light weight, conformability to irregular surfaces [5-7], and comfort while wearing as well as a large area and transparency [8, 9].

Taking advantage of the high Hall mobility that is theoretically expected of highly crystalline single-walled carbon nanotubes (HC-SWCNTs)[10-14], we aim to establish the basic packaging technology for energy-efficient wearable devices that are capable of a high-frequency response with almost zero energy loss. With the aim of realizing a low-carbon and energy-efficient process for the basic performance elements (semiconductive thin films and circuits) that make up devices, we fabricated thin films using HC-SWCNTs by a wet-coating process [15, 16] and evaluated their electrical properties in this study. The SWCNTs used in this study have high potential for use as a semiconductor and have been studied for applications to thin-film transistors (TFTs) for displays [17-20], integrated circuit (IC) tags [21-24], and sensors [25-28] in the field of conventional applied research and development. SWCNTs consist of 60–80% semiconductor tubes and 20–40% metal tubes [29], but the technologies to take advantage of their excellent semiconductor properties have not yet been established. In this study, we attempted to fabricate thin films by supporting SWCNTs on a matrix of indium tin oxide (ITO) so that the SWCNTs act as conductive paths in the thin films.

Although metal oxide films have conventionally been used as materials for electronic elements [31, 32] such as thin-film transistors and display devices, metal oxide films with a higher mobility are required in order to improve the performance of electronic elements and display devices. The results of past research have not satisfied this requirement for metal oxide films. Also, the mobility in metal oxide–carbon composite thin films has remained unclarified. The purpose of this study was to fabricate high-mobility thin films containing HC-SWCNTs by a wet-coating process while suppressing the amount of HC-SWCNTs added. Another aim was to devise a simple technique for fabricating semiconductive thin films with high mobility using fewer HC-SWCNTs under atmospheric pressure.

II. EXPERIMENTAL

2.1 Synthesis of metal oxides

The semiconductive films used in this study consist mainly of ITO as the metal oxide and contain a small amount of carbon nanotubes (CNTs). In ITO, tin oxide is a solid solute in indium oxide and its composition varies with the manufacturing conditions [15, 33, 34]. Some organic components may remain when a metalorganic compound is used as the starting material and the sintering temperature is low; however, the ITO contents in this study represent the values obtained assuming that the indium and tin contained in the field electron emission films are oxides of stoichiometric composition [16, 35].

The semiconductive films fabricated in this study essentially consist of indium oxide, tin oxide, partial decomposition products of organic compounds associated with the raw materials (indium and tin), organic substances derived from the raw materials, and HC-SWCNTs. The conducting films can contain conductive materials, such as metal particles, that do not cause adverse effects on the properties of conductive films fabricated from the materials listed above. However, fundamentally, these films do not contain insulating materials because such materials decrease the conductivity of the films.

The semiconductive films in this study are formed on a Ta substrate using SWCNTs (whose content is controlled within the range of 0.1–20 wt%) as the conductive material. While there is no limit to the type of substrate, a conductive substrate is preferable because such a substrate provides a higher degree of freedom in terms of electrical connections. Thin films with homogeneously dispersed SWCNTs are obtained by coating the substrate with a dispersion liquid, which consists of a material containing indium and a material containing tin, which are precursors of ITO, and CNTs, that forms a wet film coating on the substrate by spray coating, spin coating, dip coating, or any other generally used method, and then heating and sintering the wet film coating to form a CNT-containing ITO film. Thin films mainly consisting of ITO and containing a small amount of SWCNTs can be obtained by heating (sintering) the above-mentioned wet film coating at 430 °C. The sintering is performed in a low-vacuum atmosphere of about 0.1 Pa.

Arc-SWCNTs (ASP-100F; Hanwha Chemicals Co. Ltd., Korea) are used in this study. Highly crystalline SWCNTs are obtained by annealing the SWCNTs at a high temperature (973 K) under a high vacuum (pressure $>10^{-4}$ Pa).

2.2 Initial dispersion liquid

A mixture of 0.01 g of the above-mentioned HC-SWCNTs, ~30 g of ethyl cellulose (48–49.5%, ethoxy 100 cP; Kanto Chemical Co., Inc.), and ~160 g of butyl acetate is prepared. This mixture is subjected to ultrasonic dispersion for 30 min. After the ultrasonic dispersion, the mixture is processed ten times to disperse and collide with ink droplets including HC-SWCNTs and micro-scaled media beads by a jet mill (HJP-25001; Sugino Machine Limited) at a discharge pressure of 60 MPa to obtain a homogeneous dispersion liquid of SWCNTs.

A mixture of the above-mentioned dispersion liquid of SWCNTs and ethyl cellulose (48–49.5%, ethoxy 100 cP; Kanto Chemical Co., Inc.) is prepared. The obtained mixture is then mixed with ~15 mL (17.45 g) of ITO-05C (ITO dipping material; Kojundo Chemical Laboratory Co., Ltd.) and subjected to ultrasonic dispersion for 30 min. After the ultrasonic dispersion, the mixture is processed several times using a jet mill (HJP-25001) at a discharge pressure of 60 MPa to obtain the dispersion liquid used as the starting material. The mass of the ITO film obtained by applying and sintering ITO-05C is 2–3% of that of the ITO-05C.

2.3 SWCNT-containing ITO films

The surface of a 0.1-mm-thick Ta substrate (tantalum plate) is coated with the above-mentioned dispersion liquid of SWCNTs using a static coating spray. The thickness of the film coating is adjusted so that the film thickness after sintering becomes 20 μm. The Ta substrate coated with the dispersion liquid of SWCNTs is heated and dried at 230 °C in air for 30 min. After that, the Ta substrate coated with the dried dispersion liquid of SWCNTs is heated to 470 °C under reduced pressure (0.001 Pa) for 90 min and then left to stand for 30 min to form an SWCNT-containing ITO film on the Ta substrate. Also, SWCNT-containing ITO films that are to be used as a reference are formed on a Ta substrate by the method described above using SWCNTs that are not annealed (not processed at 973 K in a vacuum for 3 h).

Figure 1 shows a transmission electron microscopy (TEM; HR-3000; Hitachi High Tech. Co., Ltd., Japan) image of SWCNTs annealed to achieve high crystallinity and that of nonannealed SWCNTs, showing the difference in crystallinity between them. Nanobubble-like crystalline discontinuities are observed in the wall of the nonannealed SWCNTs [36, 37], indicating that there is a difference in crystallinity between the annealed and nonannealed SWCNTs.

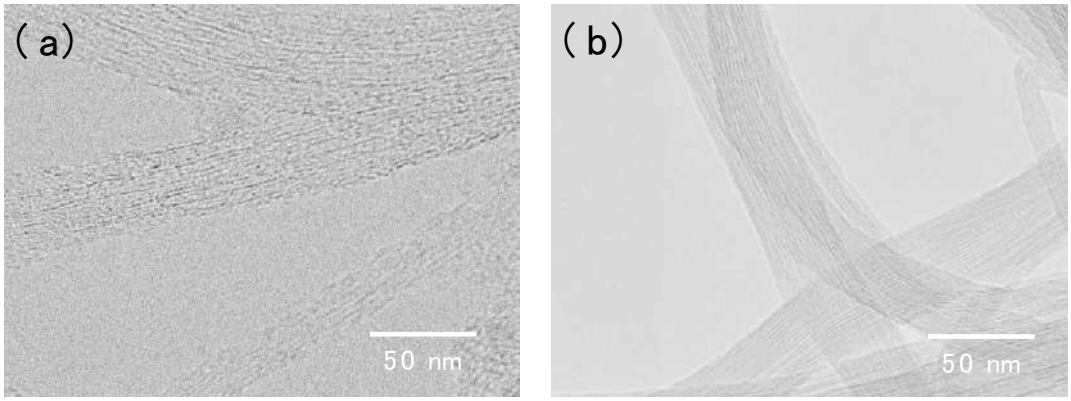

FIG. 1: TEM images of SWCNTs (accelerating voltage, 200 kV).
(a) Commercial SWCNTs and (b) highly crystalline SWCNTs

III. RESULTS AND DISCUSSION

3.1 Evaluation of film coating

The amount of SWCNTs added to thin films is controlled arbitrarily in this study. Figure 2 shows thin films containing controlled amounts of highly crystalline HC-SWCNTs. The density of HC-SWCNTs added to the thin films is defined as the weight of added HC-SWCNTs per unit area (weight density).

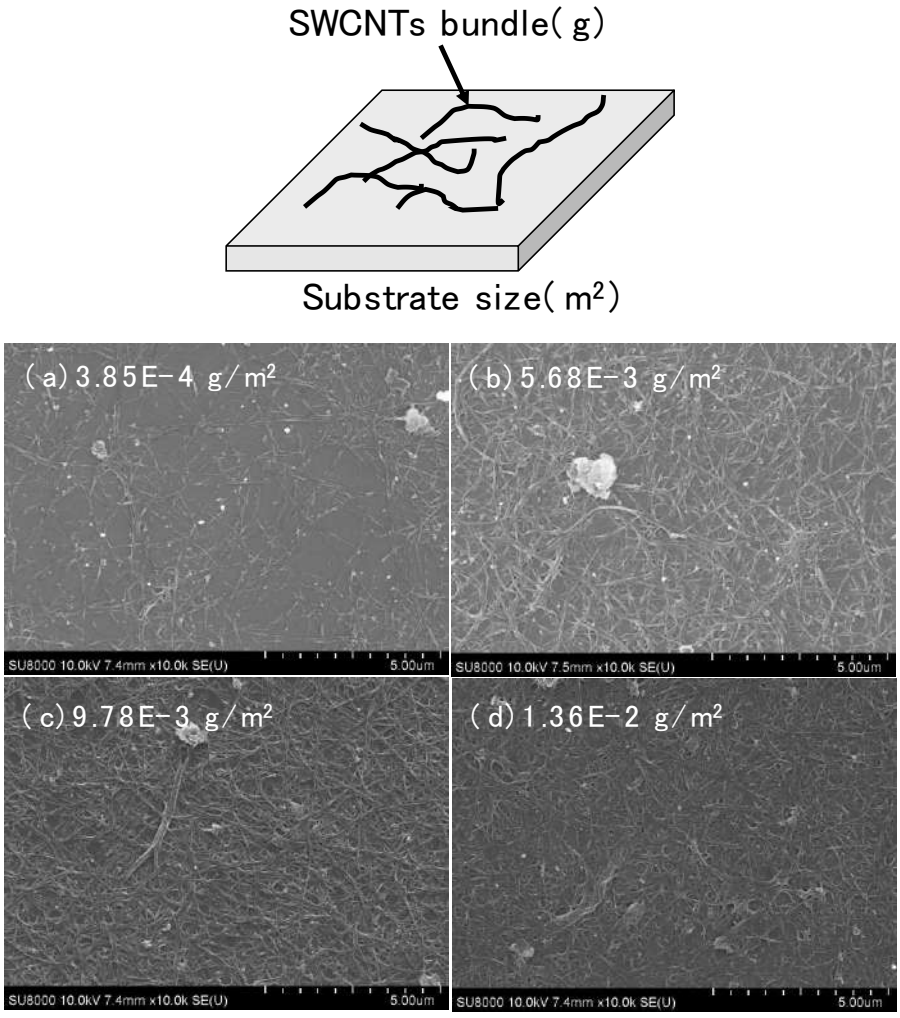

FIG. 2: Schematic of definition of weight density (top) and SEM images of surface of thin films containing HC-SWCNTs at controlled weight densities (bottom).
(a) 3.85×10^{-4} g/m^2, (b) 5.68×10^{-3} g/m^2, (c) 9.78×10^{-3} g/m^2, and (d) 1.36×10^{-2} g/m^2.

The dispersion state of SWCNTs with crystal defects is similar to that of HC-SWCNTs. Scanning electron microscopy (SEM) images show no difference in the appearance of dispersion states among SWCNTs with different crystallinity.

3.2 Measurement of mobility of SWCNT-containing ITO films

The Hall mobility of SWCNT-containing ITO films is obtained by the time-of-flight (TOF) method [38-40]. In this method, the thin films to be measured are irradiated with visible light and the time-dependent responsiveness of electric current flowing through the thin films is measured. Figure 3 shows a schematic of the measurement. In this study, thin films are irradiated with pulsed light for an arbitrarily controlled irradiation time and the responsiveness of electric current flowing after the irradiation is analyzed using an oscilloscope. On the basis of the time taken for electrons (current) generated in a thin film to reach the counter electrode [t (s)], the distance between the electrodes [L (cm)], and the electric field applied to the thin film (V/cm), the charge-transfer rate per unit electric field and per unit time μ is given by the following Eq. (1). Table 1 shows the conditions for the measurement of mobility.

$$M = L/[t \times (V/L)](\mathrm{cm}^2/\mathrm{Vs}) \quad (1)$$

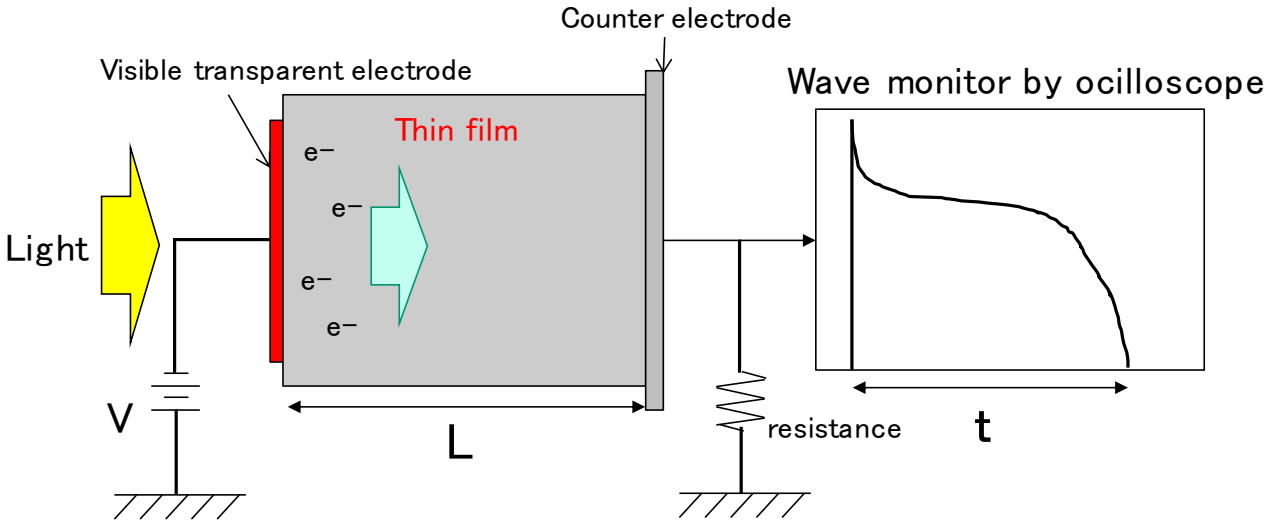

FIG. 3: Evaluation of Hall mobility by TOF method

The oscilloscope used for the measurement is a 3000T X-Series oscilloscope (1 GHz; Keysight Technologies).

TABLE 1
CONDITIONS FOR MOBILITY MEASUREMENT

Measurement sample size	10 mm × 10 mm × 20 μm
Visible transparent electrode	ITO film formed by sputtering method
Counter electrode	Ta substrate
Region formed between visible transparent electrode and counter electrode	$10 \times 10\ \mathrm{mm}^2$
Excitation light source	Halogen lamp
Applied voltage	100 V (DC)

Figure 4 shows the obtained Hall mobilities of thin films containing HC-SWCNTs at arbitrary controlled weight densities. The Hall mobility of ITO films alone and that of the thin films containing SWCNTs with crystal defects at arbitrary controlled weight densities are also measured as references. The results show that the Hall mobility increases as the weight density of SWCNTs increases. The highest Hall mobility of 1,000 $\mathrm{cm}^2/\mathrm{Vs}$ is achieved in the thin film containing HC-SWCNTs at a weight density of about 1.2×10^{-2} $\mathrm{g/m}^2$. In addition, the Hall mobility varies considerably with the crystallinity; namely, it decreases to one-tenth owing to the presence of crystal defects. The Hall mobility is dependent on the crystallinity of the SWCNTs.

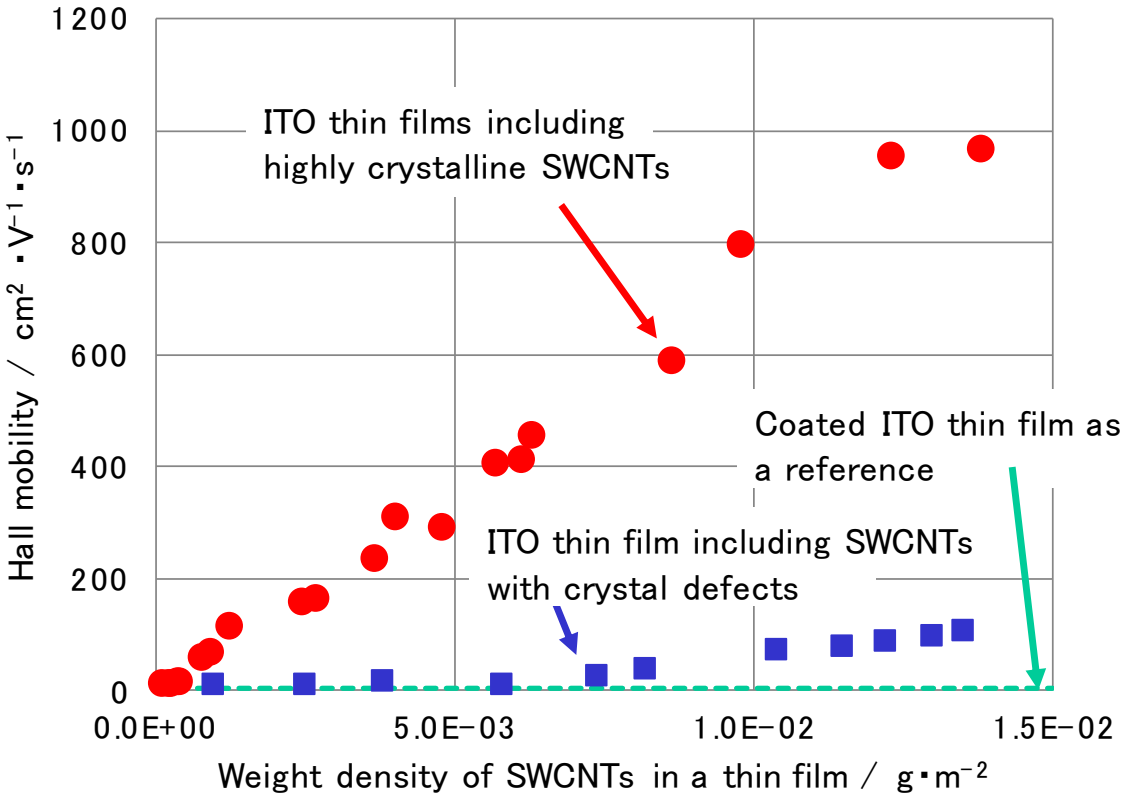

FIG. 4 Dependence of Hall mobility on weight density for different crystallinities of SWCNTs

It is known that CNTs, including SWCNTs, have a high theoretical mobility of 5,000–10,000 cm^2/Vs [41, 42]. In the CNT-containing films formed by a coating method, however, there is electrical resistance at contact points among the CNTs because many CNTs are arranged in a netlike pattern, as shown in Fig. 1. By reducing the electrical resistance among CNTs, their high potential can be realized in applications. Therefore, a variety of research and development projects related to CNT structure formation and control at the nanometer (one-millionth of a millimeter) scale have been carried out, aiming at obtaining CNTs with a small range of variation in diameter. To discuss the mobility shown in Fig. 4, we evaluate the significant variation in contact resistance resulting from the difference in the crystallinity of SWCNTs [43-46]. Nanotubes are dispersed on a Ta substrate and their contact resistance is evaluated using a tunneling current detection scanning probe microscope [SPM; MultiMode8 PeakForce TUNA (tunneling AFM); Bruker Japan K.K.]. An arbitrary voltage is applied between the sample and the probe and the current flowing in the measurement circuit shown in Fig. 5 is obtained.

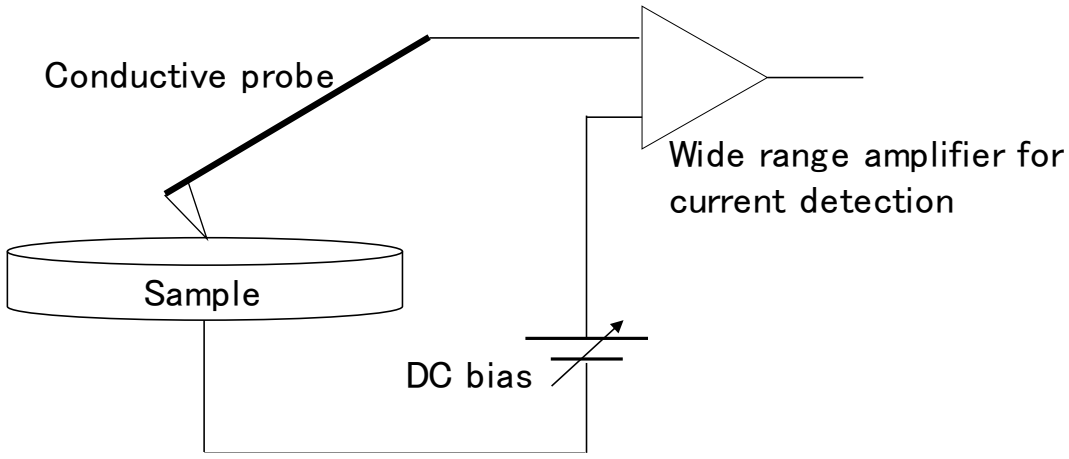

FIG. 5: Schematic of SPM used for tunneling current detection

The SPM probe used in this study is a silicon-nitride-based cantilever with a platinum–iridium-coated tip (PeakForce TUNA, Bruker Japan K.K., spring constant = 0.4 N/m). Table 2 shows the measurement conditions used for all samples.

TABLE 2
CONDITIONS FOR SPM MEASUREMENT

Measured area	$1 \times 1\ \mu m^2$
Scan rate	0.18–0.20 Hz
Amplitude setpoint	250 mV
Drive amplitude	750–825 mV
DC bias	−1.5 V

Figure 6 shows three-dimensional images of SWCNTs and SWCNT bundles prepared by dispersing SWCNTs in acetone on a Si substrate without using a dispersant, followed by heating the substrate at 150°C to dry and vaporize the acetone. The figure also shows images of the current distribution at the same locations. Figures 6(a) and 6(b) are images of HC-SWCNTs and Figs. 6(c) and 6(d) are images of SWCNTs with crystal defects. In the images of the current distribution, the dark brown color represents the areas in which electric current is detected. The areas are arranged almost in the shape of CNTs. These images show that in SWCNTs with crystal defects, the areas in which electric current is detected are more discontinuous than those in HC-SWCNTs and that electric current does not flow homogeneously in some areas. Also, contact resistance occurs at the contact points among CNTs or CNT bundles. In particular, electric current is not detected because of the high contact resistance at many of the contact points among the SWCNTs with crystal defects. Figure 7 shows the current–voltage (*IV*) characteristics at selected contact points in each sample. The measurement points are indicated by arrows in Fig. 6 (points A–F). The graph shows that the contact resistance in SWCNTs with crystal defects is relatively high compared with that in HC-SWCNTs. Because the internal resistance of CNTs is inhomogeneous, it is assumed that the areas of CNTs with high internal resistance come into contact with each other with high probability, making it difficult for electric current to flow. The contact resistance of the samples is depended on the crystallinity of CNTs can be determined from the *IV* characteristics of these samples. The above results indicate that the electric current flowing through SWCNTs depends on their crystallinity.

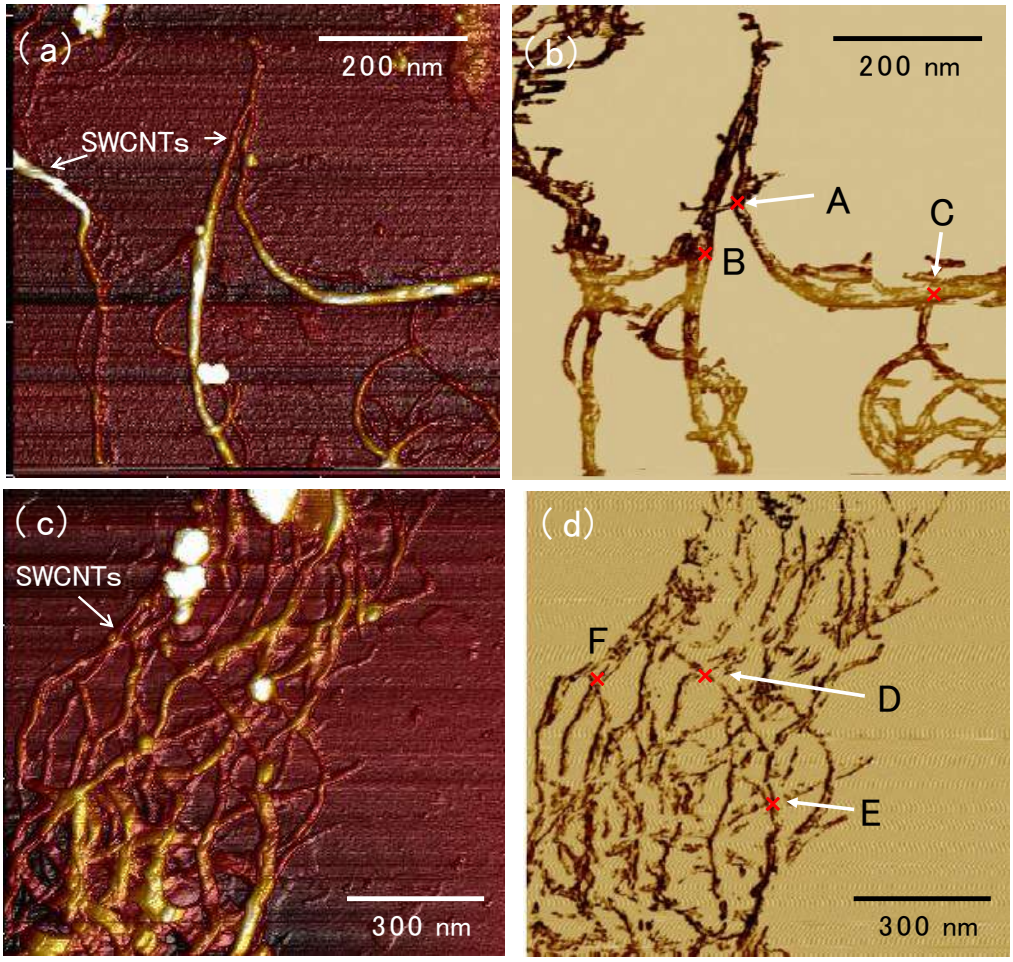

FIG. 6: SPM images.
(a), (c) Three-dimensional images and (b), (d) distribution of electric current induced by applied voltage. (a), (b) HC-SWCNTs dispersed on a Ta substrate and (c), (d) SWCNTs with crystal defects.

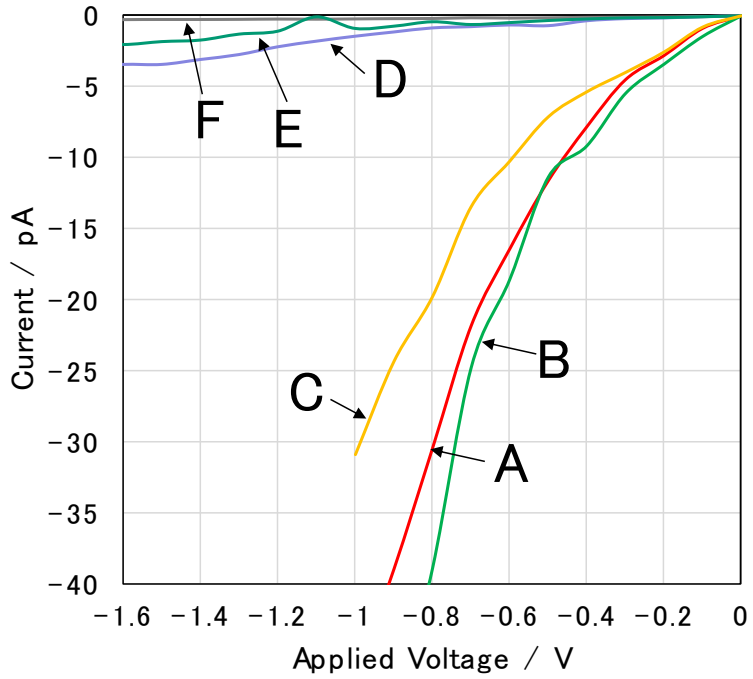

FIG. 7: IV characteristics at points A–F indicated by arrows in Figs. 6(b) and 6(d).

From Figs. 4, 6, and 7, we found that the Hall mobility can be greatly improved by controlling the density of added SWCNTs (weight density) and their crystallinity. The reason for this is that the Hall mobility reflects the increase or decrease in the number of contact points among SWCNTs as a result of controlling the density of added SWCNTs, as well as the changes in the contact resistance among the SWCNTs and their internal resistance resulting from the control of crystallinity. It is assumed that the Hall mobility of 1,000 cm^2/Vs can be achieved because the contact resistance among CNTs is small in HC-SWCNTs and therefore, the electric charge passes through multiple contact points (indicated by blue circles in Fig. 8) forming the shortest path in accordance with the density and arrangement of CNTs [Figs. 8(a) and 8(b)]. On the other hand, a path for the flow of electric charge is formed less easily in SWCNTs with crystal defects because of the higher internal resistance and contact resistance of the CNTs. The electric charge takes a less direct path as shown in Fig. 8(c), resulting in the low Hall mobility.

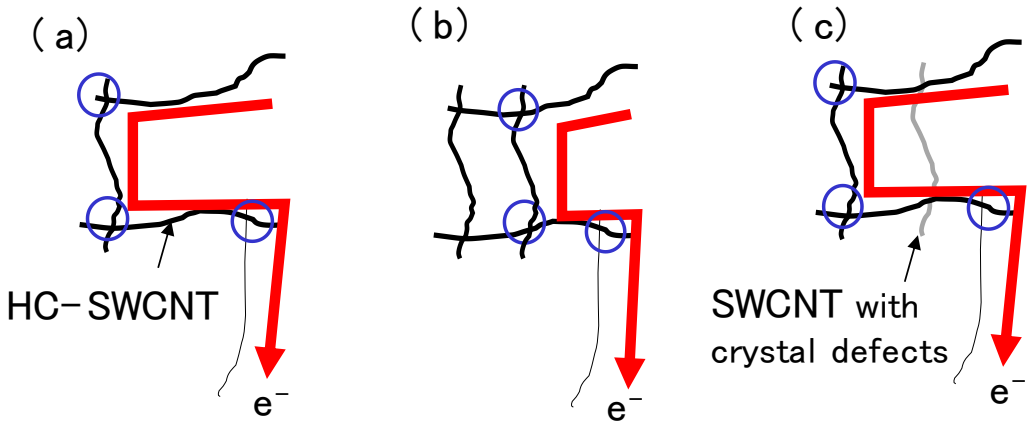

FIG. 8: Paths of electrons flowing through SWCNTs

IV. CONCLUSION

In this study, we fabricated SWCNT-containing thin films by a wet-coating process and evaluated the dependence of the Hall mobility on the weight density of added SWCNTs per unit area and the crystallinity of SWCNTs. Because CNTs, including SWCNTs, have semiconductive or metallic conductive properties, studies have been carried out with the aim of fabricating

semiconductive thin films containing semiconductive SWCNTs and taking advantage of their properties. However, the research and development of practical applications of SWCNT-containing thin films have been limited because the handling and control of SWCNTs are difficult owing to their fibrous form, and the homogeneous dispersion of SWCNTs by a wet-coating process is also difficult. Our research team has developed a technology to disperse SWCNTs without impairing their crystallinity and succeeded in fabricating thin films from a dispersion liquid of SWCNTs obtained by this technology. We also evaluated the Hall mobility of these thin films and found that a high Hall mobility of 1,000 cm^2/Vs can be achieved by controlling the crystallinity.

The analysis of the conductive characteristics of SWCNTs using an SPM for tunneling current detection revealed that the resistance characteristics of SWCNTs depend on their crystallinity. Although it has been theoretically predicted that the conductive characteristics of CNTs depend on their crystallinity[47], this was the first time ever that the crystallinity dependence of conductive characteristics was demonstrated by an SPM-based analysis. The control of the Hall mobility of thin films was realized by using highly crystalline CNTs, including HC-SWCNTs, and controlling the weight density of the CNTs contained in the thin films. The results of this study showed the possibility of using CNT-containing semiconductive films formed on a substrate of arbitrary shape as ubiquitous devices. It is expected that the electron mobility of thin films will be further increased by synthesizing SWCNTs with zero defects and improving the composition of SWCNT thin films as well as that of the ITO matrix. On the basis of the results of this study, we will pursue our research to establish a technology for packaging electronic circuits that take full advantage of the electronic properties of HC-SWCNTs by a wet-coating process, and thus, to develop environmentally friendly semiconductor devices with high packaging density. Our goal is to realize thin films with low energy losses exhibiting a Hall mobility that is near the theoretical value for CNTs.

ACKNOWLEDGEMENTS

This work was supported in part by DOWA Holdings Co. Ltd., Japan. The author would like to thank the co-researchers from DOWA for the discussions and suggestions. I am grateful for the technical instructions provided during the device-assembly process and the assembly work. This study was conducted as a project consigned by the New Energy and Industrial Technology Development Organization and supported by JSPS KAKENHI Grant Number 26220104.I would like to express our sincere gratitude for the guidance received.

REFERENCES

[1] Zhang, K.; Li, G.-H.; Feng, L.-M.; Wang,N.; Guo, J.; Sun, K.; Yu, K.-X.; Zeng, J.-B.; Li, T.; Guo, Z.; Wang, M. Ultralow percolation threshold and enhanced electromagnetic interference shielding in poly(L-lactide)/multi-walled carbon nanotube nanocomposites with electrically conductive segregated networks. *J. Mater. Chem.***2017**, *C 5(36)*, 9359-9369.

[2] Kim,K. S.; Zhao,Y.; Jang,H.; Lee,S. Y.; Kim,J. M.; Kim,K. S.;Ahn,J.-H.; Kim,P.; Choi,J.-Y.; Hong, B. H. Large-scale pattern growth of graphene films for stretchable transparent electrodes. *Nature***2009**,*457*, 706–710.

[3] Kim,D.-H.;Ahn,J.-H.; Choi,W. M.; Kim,H.-S.; Kim,T.-H.; Song,J.; Huang,Y. Y.; Liu,Z.; Lu,C.; Rogers, J. A. Stretchable and foldable silicon integrated circuits. *Science***2008**, *320*, 507–511.

[4] Sekitani,T.;Noguchi,Y.; Hata,K.; Fukushima,T.; Aida,T.; Someya,T. A rubberlike stretchable active matrix using elastic conductors.*Science***2008**, *321*, 1468–1472.

[5] Stutzman,N.; Friend,R. H.; Sirringhaus,H.Self-aligned, vertical-channel, polymer field-effect transistors. *Science***2003**, *299*, 1881-4.

[6] Dimitrakopoulos,C. D.;Purushothaman,S.;Kymissis,J.;Callegari,A.; Shaw,J. M.Low-Voltage Organic Transistors on Plastic Comprising High-Dielectric Constant Gate Insulators. *Science***1999**, *283*, 822.

[7] Dimitrakopoulos,C. D.;Malefant,P. R. L.Organic Thin Film Transistors for Large Area Electronics. *Adv. Mater.***2002**, *14*, 99-117.

[8] Nomura,K.;Ohta,H.; Takagi,A.;Kamiya,T.; Hirano,M.; Hosono,H.Room-temperature fabrication of transparent flexible thin-film transistors using amorphous oxide semiconductors. *Nature***2004**, *432*, 488-492.

[9] Nomura,K.;Ohta,H.; Ueda,K.;Kamiya,T.; Hirano,M.; Hosono,H.Thin-Film Transistor Fabricated in Single-Crystalline Transparent Oxide Semiconductor.*Science***2003**, *300*, 1269-1272.

[10] Geim,A. K.;Novoselov,K. S. The rise of graphene. *Nature Mater.***2007**, *6*, 183–191.

[11] Lee,C.; Wei,X.;Kysar,J. W.; Hone,J. Measurement of the elastic properties and intrinsic strength of monolayer graphene. *Science***2008**, *321*, 385–388.

[12] Cao,Q.; Rogers,J. A.Ultrathin Films of Single-Walled Carbon Nanotubes for Electronics and Sensors: A Review of Fundamental and Applied Aspects.*Adv. Mater.***2009**, *21(1)*, 29-53.

[13] Bauhofer,W.; Kovacs, J. Z. A review and analysis of electrical percolation in carbon nanotube polymer composites.*Comp. Sci.and Tech.***2009**, *69(10)*, 1486-1498.

[14] White,K. L.; Shuai,M.; Zhang,X.; Sue,H.-J.; Nishimura,R.Electrical conductivity of well-exfoliated single-walled carbon nanotubes.*CARBON***2011**, *49(15)*, 5124-5131.

[15] Shimoi,N.; Adriana,L.E.; Tanaka,Y.;Tohji, K. Properties of a field emission lighting plane employing highly crystalline single-walled carbon nanotubes fabricated by simple processes.*CARBON***2013**, *65*, 228-23.

[16] Garrido,S. B.; Shimoi,N.; Abe,D.; Hojo, T.; Tanaka,Y.; Tohji,K. Planar light source using a phosphor screen with single-walled carbon nanotubes as field emitters. *Rev. Sci. Inst.***2014**, *85*, 104704.

[17] Martel,R.; Schmidt,T.; Shea,H. R.; Hertel,T.;Avouris, P.Single- and multi-wall carbon nanotube field-effect transistors. *Appl. Phys.Lett.***1998**, *73*, 2447.

[18] Tans,S. J.;Verschueren,A. R. M.; Dekker, C. Room-temperature transistor based on a single carbon nanotube.*Nature***1998**, *393*, 49-52.

[19] Duan,X. F.;Niu,C. M.;Sahi,V.; Chen,J.;Parce,J. W.; Empedocles,S.; Goldman,J. L.High-performance thin-film transistors using semiconductor nanowires and nanoribbons. *Nature***2005**, *425(6955)*, 274-278.

[20] Elias,D. C.; Nair,R. R.; Mohiuddin,T. M. G.; Morozov,S. V.; Blake,P.; Halsall,M. P.; Ferrari,A. C.;Boukhvalov,D. W.;Katsnelson,M. I.;Geim,A. K.;Novoselov,K. S. Control of graphene's properties by reversible hydrogenation: evidence for graphene. *Science***2009**, 323, 610–613.

[21] Javey,A.; Guo,J.; Wang,Q.; Lundstrom,M.; Dai,H. Ballistic carbon nanotube field-effect transistors.*Nature***2003**, *424*, 654.

[22] Durkop,T.; Getty,S. A.;Cobas,E.; Fuhrer, M.S. Extraordinary Mobility in Semiconducting Carbon Nanotubes.*Nano Lett.***2004**, *4*, 35-39.

[23] Bradley,K.; Gabriel,J.-C. P.; Star,A.;Gru¨ner, G. Short-channel effects in contact-passivated nanotube chemical sensors.*Appl. Phys. Lett.***2003**, *83*, 3821.

[24] Bradley,K.; Gabriel,J.-C. P.;Gru¨ner, G. Flexible Nanotube Electronics.*Nano Lett.***2003**, *3*, 1353-1355.

[25] Gabriel,J.-C. P. Large Scale Production of Carbon Nanotube Transistors: A Generic Platform for Chemical Sensors. *MRS Proc.***2003**, *776*, Q12.7.

[26] Snow,E. S.; Novak,J. P.; Campbell,P. M.; Park, D. Random networks of carbon nanotubes as an electronic material.*Appl. Phys. Lett.***2003**, *82*, 2145.

[27] Szeluga,U.;Kumanek,B.;Trzebicka, B.Synergy in hybrid polymer/nanocarbon composites. A review.*Compos. A***2015**, *73*, 204-231.

[28] Ram,R.; Rahaman,M.; Khastgir,D. Electrical properties of polyvinylidene fluoride (PVDF)/multi-walled carbon nanotube (MWCNT) semi-transparent composites: Modelling of DC conductivity. *Compos. A*,**2015**, *69*, 30-39.

[29] Ebbesen,T.W.; Lezec,H. J.; Hiura,H.; Bennett,J. W.; Ghaemi,H. F.; Thio, T. Electrical conductivity of individual carbon nanotubes. *Nature* **1996**, *382(6586)*, 54-56.

[30] Bunch, J. S. et al. Impermeable atomic membranes from graphene sheets. *Nano Lett.***2008**, *8*, 2458–2462.

[31] Wang,X.; Li,X.; Zhang,L.; Yoon,Y.; Weber,P. K.; Wang,H.; Guo,J.; Dai1,H.N-doping of graphene through electrothermal reactions with ammonia. *Science***2009**, *324*, 768–771.

[32] Azoubel,S.; Shemesh,S.; Magdassi,S.Flexible electroluminescent device with inkjet-printed carbon nanotube electrodes.*Nanotechnology***2012**, *23(34)*, 344003.

[33] Saito,Y.; Uemura,S. Field emission from carbon nanotubes and its application to electron sources.*CARBON*, **2000**, *38(2)*, 169-182.

[34] Cao,Q.; Kim,H.-S.; Pimparkar,N.; Kulkarni,J. P.; Wang,C. J.; Shim,M.; Roy,K.; Alam,M. A.; Rogers, J. A.Medium-scale carbon nanotube thin-film integrated circuits on flexible plastic substrates. *NATURE***2008**, *454(7203)*, 495-U4.

[35] Balberg, I. TUNNELING AND NONUNIVERSAL CONDUCTIVITY IN COMPOSITE-MATERIALS.*Phys. Rev. Lett.***1987**, *59(12)*, 1305-1308.

[36] Tohji,K.; Goto,T.; Takahashi,H.; Shinoda,Y.; Shimizu,N.; Jeyadevan,B.; Matsuoka,I. ; Saito,Y.; Kasuya,A.; Ohsuna,T.; Hiraga,K.; Nishina, Y. Purifying single-walled nanotubes. *NATURE***1996**, *383(6602)*, 679.

[37] Iwata,S.; Sato,Y.; Nakai,K.; Ogura,S.; Okano,T.; Namura,M.;Kasuya,A.; Tohji,K.; Fukutani,K. Novel method to evaluate the carbon network of single-walled carbon nanotubes by hydrogen physisorption.*J. Phys. Chem. C Lett.***2007**, *111*, 14937-14941.

[38] Semenoff,G. W. Condensed-matter simulation of a three-dimensional anomaly. *Phys. Rev. Lett.***1984**, *53*, 2449–2452.

[39] Zheng,Y.; T. Ando, T. Hall conductivity of a two-dimensional graphite system. *Phys. Rev. B* **2002**, *65*, 245420.

[40] Tan,H.-X.; Xu, X.-C.Conductive properties and mechanism of various polymers doped with carbon nanotube/polyaniline hybrid nanoparticles. *Comp. Sci. and Tech.***2016**, *128*, 155-160 .

[41] Haldane, F. D. M. Model for a quantum hall effect without Landau levels: condensed-matter realization of the "parity anomaly". *Phys. Rev. Lett.***1988**, *61*, 2015–2018.

[42] Zhang,Y. B.; Tan,Y. W.; Stormer,H. L.; Kim, P.Experimental observation of the quantum Hall effect and Berry's phase in graphene. *NATURE***2005**, *438(7065)*, 201-204.

[43] Phang,I.-Y.; Liu,T.; Zhang,W.-D.; Scho¨nherr,H.; Vancso, G. J. Probing buried carbon nanotubes within polymer–nanotube composite matrices by atomic force microscopy.*European Polymer Journal***2007**, *43*, 4136–4142.

[44] Desbief,S.; Hergue,N.-E.; Douheret,O.; Surin,M.; Dubois,P.; Geerts,Y.; Lazzaronia,R.; Leclere, P. Nanoscale investigation of the electrical properties in semiconductor polymer–carbon nanotube hybrid materials.*Nanoscale***2012**, *4*, 2705.

[45] Yang,X.; Liu,R.; Lei,Y.; Li,P.; Wang,K.; Zheng,Z.; Wang, D. Dual Influence of Reduction Annealing on Diffused Hematite/FTO Junction for Enhanced Photoelectrochemical Water Oxidation. *ACS Appl. Mater. Interfaces***2016**, *8*, 16476−16485.

[46] Herrer,L.; Sebastian,V.; Martín,S.; González-Orive,A.; Pérez-Murano,F.; Low,P. J.; Serrano,J. L.; Santamaríaa,J.; Cea, P. High surface coverage of a self-assembled monolayer by in situ synthesis of palladiumanodeposits.*Nanoscale***2017**, *9*, 13281.

[47] Shimoi,N. Effect of increased crystallinity of single-walled carbon nanotubes used as field emitters on their electrical properties. *J. Appl. Phys.***2015**, *118*, 214304.

Development of a Low-Cost Arduino Based Laser Nephelometric Instrumentation for High Sensitivity determination of the Inflammatory Marker C-Reactive Protein (CRP)

Daniel H. Kriz[1*], Lars-Olof Hansson[2]
[1]European Institute of Science, IDEON Science Park, 22370, Lund, Sweden
[2]Karolinska Institute, Stockholm, Sweden

Abstract**—** *A simple low-cost (<60 USD) Arduino based laser nephelometric instrument, which is suitable for high sensitive immunoprecipitation detection is presented. A measuring range of up to 49 mg/L of dog C-Reactive Protein (CRP) is reported. Furthermore, the limit of detection (LOD) is determined to be 2.1 mg/L. Only 24 µL of dog serum samples are required. Assay-time is 6 minutes. We successfully demonstrated the good performance of the device on two low level (0 and 10.2 mg/L CRP) dog serum samples. The coefficient of variation (CV) was 10% at the level of 10.2 mg/L.*

Keywords— nephelometry, immunoprecipitation, C-Reactive Protein, laser, Arduino.

I. INTRODUCTION

Immunoprecipitation reactions are used for the quantitative analysis of chemical substances in clinical chemistry. The operational principle is based on the formation of immuno-complexes through interactions between antiserum (antibody) and antigen (protein). These complexes can under certain premises aggregate and form precipitates which might scatter light. Both in clinical chemistry and under *in vivo* conditions the formation of immuno-complexes is well documented in scientific literature and books[1].

The immunoprecipitation reactions were for the first time described in the scientific literature already in 1897 by Rudolf Kraus, who published his work with antiserum against cholera and thypoid[2]. Immunoprecipitation is a technique involving precipitation of a dissolved antigen using antiserum that specifically bound to the antigen. The technique has become widely spread in biochemistry and is being used for isolation and separation of antigens[3], as well as, for analytical purposes[4] in clinical chemistry. Continuous improvement of diagnostic methods is of a vital importance for clinical chemistry to improve the diagnosis of diseases.

Antibodies (immunoglobulins) are proteins found in vertebrates with the specific purpose to defend the organism against infection[3]. The immunoglobulin mainly used in immunoassays is immunoglobulin G (IgG). Macromolecules, such as proteins, that are foreign to the organism can induce an immune response and are referred to as antigens. Antibodies (given as Ab) interact with antigens (given as Ag) to form immuno-complexes (given as AgAb) through weak interactions.

Each IgG-antibody contains two identical antigen-binding sites, and is therefore bivalent and thus able to cross link antigens (especially macromolecular antigens) to form large lattices. Once a lattice grows beyond a certain size, it precipitates out of solution (see Fig. 1).

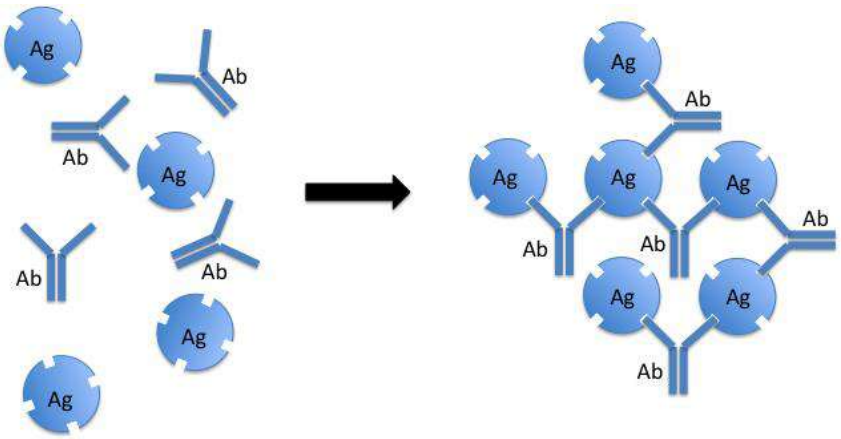

FIGURE 1: Figure illustrating the antibody (Ab) and antigen (Ag) binding and the formation of the insoluble immunoprecipitate complex (AgAb)

The binding reaction between the antibody and antigen is caused by weak interactions, and not by covalent bond formation[2]. This weak binding reaction resembles host-guest chemistry, in which the interaction involves 3-dimensional shapes, as well as, ionic bonds, London dispersion forces, dipole-dipole attractions, and hydrogen bonds[6]. Therefore, they are affected by conditions such as temperature, pH, polymers (e.g. PEG 6000, and Dextrans) and ionic strength. The reversible equilibrium reaction is given by reaction formula (1).

$$Ag_{aq} + Ab_{aq} \leftrightharpoons AgAb_{aq} \quad (1)$$

$$K = \frac{[AgAb]}{[Ag][Ab]} \quad (2)$$

The equilibrium constant of the reaction formula (1) can be calculated according to equation (2) and has experimentally found to have a value ranging[3] from 10^4 M^{-1} to 10^{12} M^{-1}. This means that the reaction nearly completely shifts towards the dissolved antibody-antigen complex. However, the dissolved antibody-antigen complex also reacts with free antibodies (that are in excess) and is further cross-linked into insoluble immunoprecipitate as illustrated in equation (3). However, it is also important to remember that when using polyclonal antisera directed against larger macromolecules like plasma proteins the antisera contains a spectrum of antibodies with varying affinity constants.

$$AgAb_{aq} + Ab_{aq} \longrightarrow AgAb_s \quad (3)$$

Light entering a solution containing suspended immunocomplex particles is scattered. This scattering, caused by the particles, occurs in all directions due to reflection and refraction[7]. Therefore, immunoprecipitation can be measured with light scattering techniques such as turbidimetry and nephelometry. Turbidimetry measures the decrease of the transmitted light and nephelometry measures the scattered light of the sample. An ordinary spectrophotometer can be used for turbidimetry. For point-of-care applications, a standard spectrophotometer is costly, and turbidimetry does not perform as well as nephelometry in dilute solutions, which makes turbidimetry less sensitive. For nephelometry, specialized instrumentation is required, which is even more costly than standard spectrophotometers.

We describe in this paper the construction and the evaluation of a simple and low-cost Arduino based laser nephelometric instrument, which is suitable for rapid and high sensitive detection of immunoprecipitates. As a model application, we evaluated the device for the low-level determination of the inflammatory marker canine C-reactive protein (cCRP)[5]. The C-reactive protein measurements are used clinically for the detection and management of bacterial infections, ischemic necrosis of tissue, and active inflammatory conditions. Most commercially available point-of-care assays for CRP are only suitable for the measurements of CRP concentrations higher than 5-10 mg/L

II. MATERIALS AND METHODS

2.1 Reagents

The Immunoturbidimetric assay for canine CRP (art. No. CP2798) was obtained from Randox (Ireland). Two dog serum samples containing 0 mg/L and 10.2 mg/L CRP, respectively, were obtained from a local veterinary hospital.

2.2 Instrumentation

The Arduino based Nephelometer was built using the following components: Arduino Uno R3 (Arduino, Italy), Black Plastic Rod (Delrin®, D15mm * L40mm), Laser module 670 nm (Art. No.41002975, Elektrokit AB, Sweden), High-Sensitivity Light-to-Voltage Converter TSL257-LF (Art. No. 1226886, Farnell, UK), and an Electronic brick - 5V Relay (Art. No. 41010280, Elektrokit AB, Sweden). The Arduino based nephelometer construction is shown in Fig. 2. The nephelometer was controlled by a software, which is illustrated in Fig. 3. The instrument uses the inbuilt serial interface of the Arduino to transfer data to a computer or to a printer.

2.3 Methods

The method used for this experiment was copied from the instruction for use in the immunoturbidimetric assay for canine CRP. The dog serum sample was filtered through a sterile filter 0.2 µm (Sarstedt, Germany) and subsequently diluted 1:10 with H_2O. The measuring procedure consisted of a first step, where 450µl Reaction Buffer R1 and 24 µl sample were added in the glass vial (Waters, USA), which followed with a 1-minute incubation in the nephelometer, which resulted in signal N_1. Subsequently, 66 µl Antibody Reagent R2 was added and the mixture allowed to incubate during 5 minutes in the nephelometer. The resulting signal N_2 was measured and finally the nephelometric signal was calculated as $\Delta N = N_2 - N_1$.

The glass vials (diameter 8.1mm – length 40mm) were used as cuvettes. However, the vials had to be marked so that the same orientation was always kept in the nephelometer, in order to avoid signal variations dependent on rotation of the vial. The standards used for the calibration curve contained the following concentrations of CRP: 0 mg/L, 10.4 mg/L, 22.6 mg/L, and 49.4 mg/L.

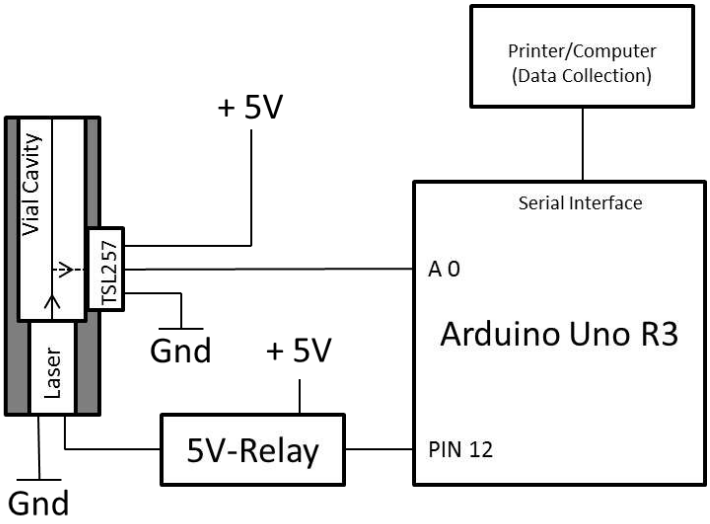

FIGURE 2: The construction of the simple low-cost Arduino based laser nephelometric instrument

```
Laser Nephelometry Meter v2.0 Measures the nephelometry of a substance using a light detector and laser (modified 29 January 2018, by D. H. Kriz)

constint reactiontime1 =  60; //60 second pause before first measurement
constint reactiontime2 =  300; //300 second reaction time before second measurement
intbuttonState = 0;
intledPin = 0;
int A=0;
long B=0;
longsensorValue=0;
int nephelometry1=0;
int nephelometry2=0;
int nephelometry=0;

void setup() {
pinMode(2,INPUT);
pinMode(12, OUTPUT);
pinMode(13, OUTPUT);
Serial.begin(9600);
}
void loop() {

Step1:
buttonState = digitalRead(2);
if (buttonState == LOW) {
goto Step1;
  }
digitalWrite(13, HIGH);
digitalWrite(12, LOW);
for (A=1; A<reactiontime1; A++) {
delay (1000); }
digitalWrite(12, HIGH);
delay (5000);
   B=0;
for (A=1; A<401; A++) {
sensorValue = analogRead(A0);
   B=B+sensorValue;
   }
nephelometry1=B/400;
Serial.println(nephelometry1); //Send results to serial port
digitalWrite(12, LOW);

Step2:
buttonState = digitalRead(2);
digitalWrite(13, HIGH);
delay(100);
digitalWrite(13, LOW);
delay(100);
if (buttonState == LOW) {
goto Step2;
  }
digitalWrite(13, HIGH);
for (A=1; A<reactiontime2; A++) {
delay (1000); }
digitalWrite(12, HIGH);
delay (5000);
   B=0;
for (A=1; A<401; A++) {
sensorValue = analogRead(A0);
   B=B+sensorValue;
   }
   nephelometry2=B/400;

Serial.println(nephelometry2); //Send results to serial port

 Step3:
nephelometry=nephelometry2-nephelometry1; //Calculate nephelometric signal increase
Serial.println(nephelometry); //Send results to serial port
digitalWrite(12, LOW);
digitalWrite(13, LOW);
}
```

FIGURE 3: Arduino Software

III. RESULTS

We observed that the nephelometric signal (ΔN) caused by the immunoprecipitation reaction, increases with the CRP concentration in the range 0-49 mg/L (see Fig. 4). After an initial linear increase, the nephelometric signal saturates at higher CRP concentrations. We modelled a mathematical curve and found that the best-fit curve is y= -0.2546x2 + 24.02x + 127.41 (R2=0.9999).

A dog serum sample containing 0 mg/L CRP was measured 3 times and the following nephelometric signals were obtained: 111 AU, 146 AU, 119 AU, which gives an average of 125 ±15 AU. Using the best-fit curve equation above, the dog serum CRP concentration was determined to be -0.1 ± 0.6 mg/L.

Furthermore, a dog serum sample containing 10.2 mg/L CRP was measured 3 times and the following results were obtained: 332 AU, 291 AU, 303 AU, which gives an average of 309 ±17 AU. Using the equation above, the dog serum CRP concentration was determined to be 8.3±0.9 mg/L. The relative standard deviation (RSD) was found to be 10%.

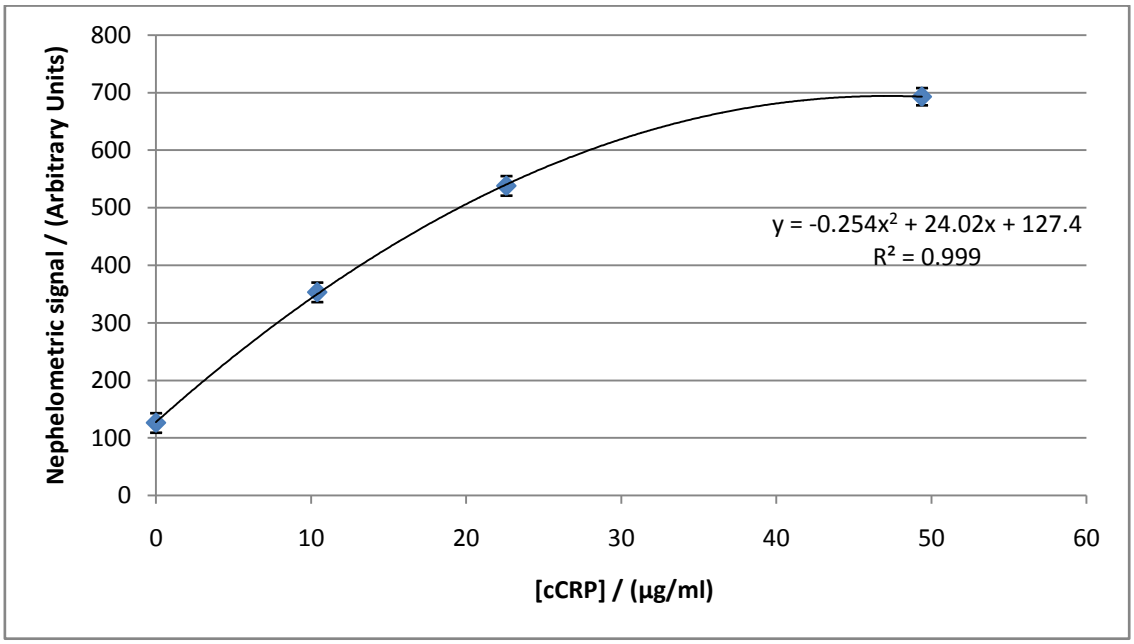

FIGURE 4: Signal observed with an Arduino based nephelometer for C-reactive protein concentrations in the range of 0-49 µg/ml in the sample.

IV. DISCUSSION

According to our results, we have demonstrated that the Arduino based nephelometer was capable of measuring on dog serum samples containing low levels of CRP (0 and 10.2 mg/L).

For the dog serum sample containing 10.2 mg/L CRP, we obtained 8.3 ± 0.9 mg/L, which is 19 % lower than anticipated. However, the RANDOX calibration solutions are based on human CRP, which could explain the slight deviation, as we are measuring canine CRP using human CRP reagent.

In order to estimate the limit of detection (LOD) of our device, we used the standard deviation value (SD=0.15 AU) obtained for the dog serum sample containing 0 mg/L CRP. The limit of detection is calculated by using Δy = 3*SD and the approximated linear calibration curve for the range 0-10 µg/ml (y=21.8x + 126). This results in a limit of detection (LOD) of 2.1 mg/L CRP.

The performance of the Arduino based nephelometer with relation to cost (<60 USD) was very satisfying. Of course, further optimization of the system is needed. This device would thus be of interest to use in many low-income countries if applied to human CRP.

V. CONCLUSION

In conclusion, we describe in this paper a simple low-cost (<60 USD) Arduino laser based nephelometric instrumentation, which is suitable for high sensitive immunoprecipitation detection. We successfully demonstrated the good performance of

the device on dog serum samples.

REFERENCES

[1] Reverberi, Roberto, and Lorenzo Reverberi. "Factors Affecting the Antigen-antibody Reaction." *Blood Transfus.* 2007, Nov;5(4):227-40.

[2] Pauling, Linus, Dan H. Campbell, and David Pressman. "The Nature of the Forces between Antigen and Antibody and of the Precipitation Reaction." Physiological Reviews 23.3 (1943): 203-219.

[3] Boyden, A., Bolton, E., and Gemeroy, D., Precipitin testing with special reference to the photoelectric measurement of turbidity. J. Immunol. 57, 211 (1947). Ritchie, R. F., A simple, direct, and sensitive technique for measurement of specific protein in dilute solution. J. Lab. Gun. Med. 70,512 (1967).

[4] Bangs Laboratories, Inc. Light-Scattering Assays. Tech. no. 304. Fishers: Bangs Laboratories, 1999.

[5] Hansson, Lars-Olof, and Lars Lindquist. "C-reactive Protein: Its Role in the Diagnosis and Follow-up of Infectious Diseases." Current Opinion in Infectious Diseases 10.3 (1997): 196-201.

[6] Killingsworth, L. M., and Savory, J., Manual nephelometric methods for immunochemical determination of immunoglobulins, IgG, IgA, and 1gM in human serum. Gun. Chem. 18, 335 (1972).

[7] Farrell, G. W., and Wolf, P., Immunonephelometric determination of fibrinogen and its derivatives in plasma. J. Immunol. Methods 1,217 (1972).

Phacoablation by Ultraviolet Laser

Prof.(Dr.) Bijay Kumar Parida (MBBS,LLB,MS,ICO,FRCSG)

Associate Professor, Muthusamy Virtual University of Ophthalmology Post Graduation, Bhubaneswar, Odisha, India

Abstract— *New method of multi mode fiberoptic endoscopic delivery of UV laser from Excimer can cause capsulorhexis and ablate cataract in human eyes. This shall eliminate LASER assisted cataract surgery which is exuberantly costly and also traditional phacoemulsification machine.*

Keywords— excimer laser fiber optics, phacosurgery.

I. INTRODUCTION

LASER from excimer machine, if can be delivered on the surface of cataractous lens, then it can do cataract surgery easily. Phaco means lens and ablation means destruction. So cataract surgery done by light is called phacoablation.

An excimer laser, sometimes more correctly called an exciplex laser, is a form of ultraviolet laser which is commonly used in the production of microelectronic devices, semiconductor based integrated circuits or "chips", eye surgery, and micromachining.

II. HYPOTHSIS

Excimer laser can be transmitted through fiber optics to a distance place away from machine. This requires multi mode fiber optic system. The fibers can be embedded in a metallic tube of diameter 1mm.such a system has so many advantages. A bent tip delivery system can be used to make capsular rhexis and bent tip can be used for phacoablation.

PHOTO 1: PLANNED PLANNED OPTICAL FIBER for human eye

Photo 1

Optic fibers inside a metallic tube of diameter 1mm. in both the photos

.

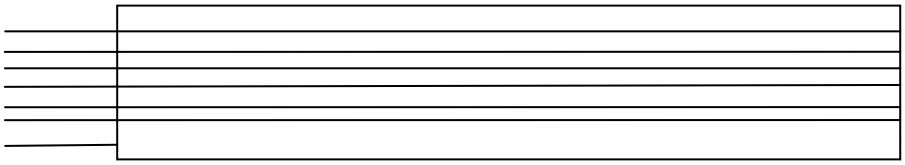

PHOTO 2:

Photo 2 of eye with lens at center Covered by capsule, that has to be cut before in this shape doing phacoablation for cataract surgery

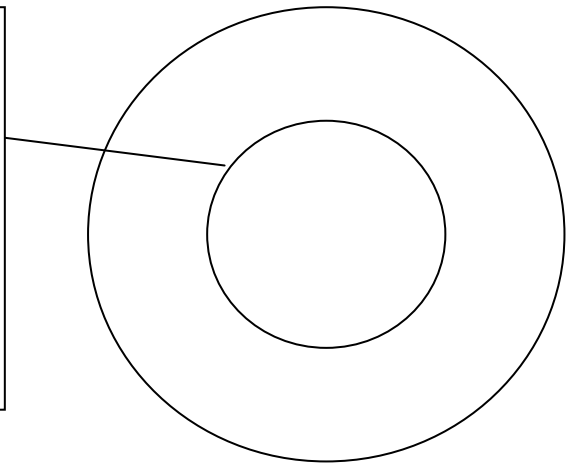

PHOTO 3:bent tip for capsulorrhexis

Photo 1-2:

Specially designed tipped
Endolasrer for capsuorhexis

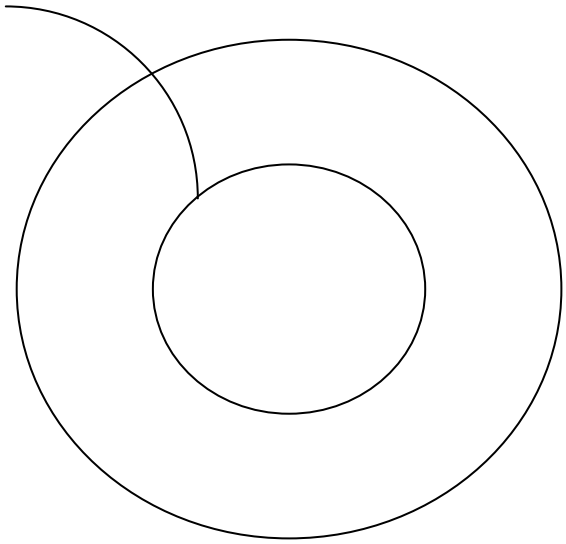

PHOTO 4: Straight tip for phacoablation

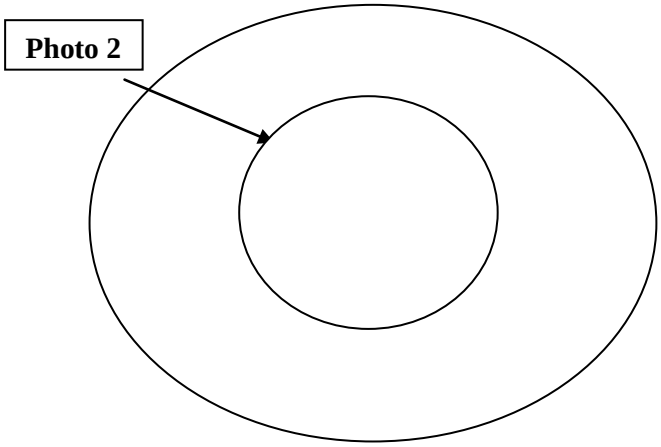

An optical fiber or optical fibre is a flexible, transparent fiber made by drawing glass (silica) or plastic to a diameter slightly thicker than that of a human hair.[1] Optical fibers are used most often as a means to transmit light between the two ends of the fiber and find wide usage in fiber-optic communications, where they permit transmission over longer distances and at higher bandwidths (data rates) than wire cables. Fibers are used instead of metal wires because signals travel along them with less loss; in addition, fibers are immune to electromagnetic interference, a problem from which metal wires suffer excessively.[2]Fibers are also used for illumination and imaging, and are often wrapped in bundles so that they may be used to carry light into, or images out of confined spaces, as in the case of a fiberscope.[3] Specially designed fibers are also used for a variety of other applications, some of them being fiber optic sensors and fiber lasers.[4]

Optical fibers typically include a core surrounded by a transparent cladding material with a lower index of refraction. Light is kept in the core by the phenomenon of total internal reflection which causes the fiber to act as a waveguide.[5] Fibers that support many propagation paths or transverse modes are called multi-mode fibers, while those that support a single mode are called single-mode fibers (SMF). Multi-mode fibers generally have a wider core diameter[6] and are used for short-distance communication links and for applications where high power must be transmitted. Single-mode fibers are used for most communication links longer than 1,000 meters (3,300 ft).

Being able to join optical fibers with low loss is important in fiber optic communication.[7] This is more complex than joining electrical wire or cable and involves careful cleaving of the fibers, precise alignment of the fiber cores, and the

coupling of these aligned cores. For applications that demand a permanent connection a fusion splice is common. In this technique, an electric arc is used to melt the ends of the fibers together. Another common technique is a mechanical splice, where the ends of the fibers are held in contact by mechanical force. Temporary or semi-permanent connections are made by means of specialized optical fiber connectors.[8]

The field of applied science and engineering concerned with the design and application of optical fibers is known as fiber optics. The term was coined by Indian physicist Narinder Singh Kapany, who is widely acknowledged as the father of fiber optics.[9]

The tip of the multi mode fibers can be reduced to 1mm to deliver the laser to ablate the human cataractous lens. The fibers can be embedded in a metallic cylinder of caliber 1 mm. The tip of this cylinder can be introduced through cornea. The anterior capsule can be excised by ablating in circle. Subsequently the lens can be hydro dissected to make it free. Anterior chamber can be filled with viscoelastic substance. Then the tip of the fiber optics is set near the lens. Ablation lens can be continued in one direction covering maximum area possible till all nuclear material is ablated. Then the lens can be rotated to complete the ablation in all directions. Subsequently irrigation and aspiration may be used to complete phacoablation by UV laser from excimer laser.

III. HISTORY

Femtosecond laser is used now-a-days to make capsular rhexis of human lens. The same laser is used to soften the lens. Phacoemulsification of cataract is done then traditional method. This machine shall displace LASER ASSISSTED CATARCT SURGERY & made an useless tool,which is costing exuberantly high around $555000 and every year maintenance cost $30000.Along with this machine, the surgeon has to purchase a standard phacoemulsification machine. By this new method of transmitting laser to the surface of lens, surgeon shall get rid of phacoemeulsification machine also. Femtosecond Laser Technology Current femtosecond laser technology systems use neodymium: glass 1053 nm (near-infrared) wavelength. light. This feature allows the light to be focused at a 3 mm spot size, accurate within 5 mm in the anterior segment.[10] The critical aspect of femtosecond laser technology is the speed at which the light is fired. The focused ultrashort pulses (1015 seconds) eliminate the collateral damage of surrounding tissues and the heat generation associated with slower excimer and neodymium: YAG lasers.

IV. DISCUSSION

4.1 Terminology

The term excimer is short for 'excited dimer', while exciplex is short for 'excited complex'. Most excimer lasers are of the noble gas halide type, for which the term excimer is strictly speaking a misnomer (since a dimer refers to a molecule of two identical or similar parts): The correct but less commonly used name for such is exciplex laser.

4.2 History

The excimer laser was invented in 1970[11] by Nikolai Basov, V. A. Danilychev and Yu. M. Popov, at the Lebedev Physical Institute in Moscow, using a xenon dimer (Xe2) excited by an electron beam to give stimulated emission at 172 nm wavelength. A later improvement, developed by many groups in 1975[12] was the use of noble gas halides (originally XeBr). These groups include the Avco Everett Research Laboratory,[13] Sandia Laboratories,14] the Northrop Research and Technology Center,[15]and the United States Government's Naval Research Laboratory[16] who also developed a XeCl Laser[17] that was excited using a microwave discharge.[18]

4.3 Construction

An excimer laser typically uses a combination of a noble gas (argon, krypton, or xenon) and a reactive gas (fluorine or chlorine). Under the appropriate conditions of electrical stimulation and high pressure, a pseudo-molecule called an excimer (or in the case of noble gas halides, exciplex) is created, which can only exist in an energized state and can give rise to laser light in the ultraviolet range.[19][20]

4.4 Operation

Laser action in an excimer molecule occurs not because it has a bound (associative) excited state, but a repulsive (dissociative) ground state. This is because noble gases such as xenon and krypton are highly inert and do not usually form chemical compounds. However, when in an excited state (induced by an electrical discharge or high-energy electron beams, which produce high energy pulses), they can form temporarily bound molecules with themselves (dimers) or

with halogens (complexes) such as fluorine and chlorine. The excited compound can give up its excess energy by undergoing spontaneous or stimulated emission, resulting in a strongly repulsive ground state molecule which very quickly (on the order of a picosecond) dissociates back into two unbound atoms. This forms a population inversion.

4.5 Wavelength determination

The wavelength of an excimer laser depends on the molecules used, and is usually in the ultraviolet:

TABLE 1
THE WAVELENGTH OF AN EXCIMER LASER

Excimer	Wavelength	Relative power
Ar_2*	126 nm	
Kr_2*	146 nm	
F_2*	157 nm	
Xe_2*	172 & 175 nm	
ArF	193 nm	60
KrF	248 nm	100
XeBr	282 nm	
XeCl	308 nm	50
XeF	351 nm	45
KrCl	222 nm	25

Excimer lasers, such as XeF and KrF, can also be made slightly tunable using a variety of prism and grating intracavity arrangements.[21]

4.6 Medical uses

The ultraviolet light from an excimer laser is well absorbed by biological matter and organic compounds. Rather than burning or cutting material, the excimer laser adds enough energy to disrupt the molecular bonds of the surface tissue, which effectively disintegrates into the air in a tightly controlled manner through ablation rather than burning. Thus excimer lasers have the useful property that they can remove exceptionally fine layers of surface material with almost no heating or change to the remainder of the material which is left intact. These properties make excimer lasers well suited to precision micromachining organic material (including certain polymers and plastics), or delicate surgeries such as eye surgery LASIK. In 1980–1983, Rangaswamy Srinivasan, Samuel Blum and James J. Wynne at IBM's T. J. Watson Research Center observed the effect of the ultraviolet excimer laser on biological materials. Intrigued, they investigated further, finding that the laser made clean, precise cuts that would be ideal for delicate surgeries. This resulted in a fundamental patent [22] and Srinivasan, Blum and Wynne were elected to the National Inventors Hall of Fame in 2002. In 2012, the team members were honored with National Medal of Technology and Innovation by the President of The United States Barack Obama for their work related to the excimer laser.[23] Subsequent work introduced the excimer laser for use in angioplasty.[24] Xenon chloride (308 nm) excimer lasers can also treat a variety of dermatological conditions including psoriasis, vitiligo, atopic dermatitis, alopecia areata and leukoderma.

As light sources, excimer lasers are generally large in size, which is a disadvantage in their medical applications, although their sizes are rapidly decreasing with ongoing development.

Research is being conducted to compare differences in safety and effectiveness outcomes between conventional excimer laser refractive surgery and wavefront-guided or wavefront-optimized refractive surgery, as wavefront methods may better correct for higher-order aberrations.[25]

4.7 Scientific research

Excimer lasers are also widely used in numerous fields of scientific research, both as primary sources and, particularly the XeCl laser, as pump sources for tunable dye lasers, mainly to excite laser dyes emitting in the blue-green region of the spectrum.[26][27]

4.8 Repetition rate

Excimer lasers are usually operated with a pulse repetition rate of around 100 Hz and pulse duration of ~10 ns, although some operate at pulse repetition rates as high as 8 kHz and some have pulse widths as large as 30 ns.

V. ENDOSCOPIC LASER SYSTEM

Endoscopic cyclophotocoagulation (ECP) is a cyclodestructive procedure developed by Martin Uram in 1992. It functions to minimize the disadvantages of more traditional cyclodestructive procedures while maximizing the advantage of ablating the ciliary body epithelium to decrease intraocular pressure (IOP). It uses a laser endoscope containing three fiber groupings: an image guide, a light source, and the semiconductor diode laser. This technology allows direct visualization of the ciliary epithelium. Allowing the laser energy to be precisely delivered to the ciliary processes, thus limiting damage to the underlying ciliary body and surrounding tissue.[28]

Cataract surgery is the most commonly performed surgical procedure in the world, with an estimated 19 million operations performed annually. World Health Organization estimates this number will increase to 32 million by the year 2020 as the over65 population doubles worldwide between 2000 and 2020.29] Globally, more than 3000 eye surgeons (more than 1000 United States surgeons) have been trained. Femtosecond laser technology, introduced clinically for ophthalmic surgery in 2001 as a new technique for creating lamellar flaps in laser in situ keratomileusis (LASIK), has recently been developed into a tool for cataract surgery.[30]

So such a new endoscopic surgery of cataract shall be easier, faster, cheaper and has a wide market.

VI. CONCLUSION

Multi mode fiberoptic endoscopic delivery of excimer laser around 126-156 nm through clear cornea can make capsule rhexis easy and ablate cataractous lens, eliminating phacoemulsification machine and laser assisted cataract surgery. It will be cheaper and reduce the cost of cataract surgery.

REFERENCES

[1] Optical Fiber". www.thefoa.org. The Fiber Optic Association. Retrieved 17 April2015.

[2] Senior, John M.; Jamro, M. Yousif (2009). Optical fiber communications: principles and practice. Pearson Education. pp. 7–9. ISBN 013032681X.

[3] "Birth of Fiberscopes". www.olympus-global.com. Olympus Corporation. Retrieved 17 April 2015.

[4] Lee, Byoungho (2003). "Review of the present status of optical fiber sensors". Optical Fiber Technology. 9 (2): 57-79. doi:10.1016/s1068-5200(02)00527-8.

[5] Senior, pp. 12–14

[6] The Optical Industry & Systems Purchasing Directory. Optical Publishing Company. 1984.

[7] Senior, p. 218

[8] Senior, pp. 234–235

[9] "Narinder Singh Kapany Chair in Opto-electronics". ucsc.edu.

[10] Kullman G, Pineda R II. Alternative applications of the femtosecond laser in ophthalmology. Semin Ophthalmol 2010; 25:256–264.

[11] Basov, N. G. et al., Zh. Eksp. Fiz. i Tekh. Pis'ma. Red. 12, 473(1970).

[12] Basting, D. et al., History and future prospects of excimer laser technology, 2nd International Symposium on Laser Precision Microfabrication, pages 14–22.

[13] Ewing, J. J. and Brau, C. A. (1975), Laser action on the 2 Sigma+ 1/2--> 2 Sigma+ 1/2 bands of KrF and XeCl, Appl. Phys. Lett., vol. 27, no. 6, pages 350–352.

[14] Tisone, G. C. and Hays, A. K. and Hoffman, J. M. (1975), 100 MW, 248.4 nm, KrF laser excited by an electron beam, Optics Comm., vol. 15, no. 2, pages 188–189.

[15] Ault, E. R. et al. (1975), High-power xenon fluoride laser, Applied Physics Letters 27, p. 413.

[16] Searles, S. K. and Hart, G. A., (1975), Stimulated emission at 281.8 nm from XeBr, Applied Physics Letters 27, p. 243.

[17] "High Efficiency Microwave Discharge XeCl Laser", C. P. Christensen, R. W. Waynant and B. J. Feldman, Appl. Phys. Lett. 46, 321 (1985).

[18] Microwave discharge resulted in much smaller footprint, very high pulse repetition rate excimer laser, commercialized under U. S. Patent 4,796,271 by Potomac Photonics, Inc.

[19] IUPAC, Compendium of Chemical Terminology, 2nd ed. (the "Gold Book") (1997). Online corrected version: (2006–) "excimer laser".

[20] Basting, D. and Marowsky, G., Eds., Excimer Laser Technology, Springer, 2005.

[21] F. J. Duarte (Ed.), Tunable Lasers Handbook (Academic, New York, 1995) Chapter 3.

[22] US 4784135, "Far ultraviolet surgical and dental procedures", issued 1988-10-15

[23] "IBM News Release". IBM. Retrieved 21 December 2012.

[24] R. Linsker; R. Srinivasan; J. J. Wynne; D. R. Alonso (1984). "Far-ultraviolet laser ablation of atherosclerotic lesions". Lasers Surg. Med. 4 (1): 201–206. doi:10.1002/lsm.1900040212.

[25] Li SM, Kang MT, Zhou Y, Wang NL, Lindsley K (2017). "Wavefront excimer laser refractive surgery for adults with refractive errors". Cochrane Database Syst Rev. 6: CD012687. doi:10.1002/14651858.CD012687.

[26] Duarte, F. J. and Hillman, L. W. (Eds.), Dye Laser Principles (Academic, New York, 1990) Chapter 6.

[27] Tallman, C. and Tennant, R., Large-scale excimer-laser-pumped dye lasers, in High Power Dye Lasers, Duarte, F. J. (Ed.) (Springer, Berlin, 1991) Chapter 4.

[28] Uram M. Endoscopic cyclophotocoagulation in glaucoma management. Curr Opin Ophthalmol. 1995;6(2):19–29.

[29] Brian G, Taylor H. Cataract blindness – challenges for the 21st century. Bull World Health Org 2001; 79:249–256. Available at: http://www.ncbi.nlm.nih.gov/pmc/articles/PMC2566371/pdf/ 11285671.pdf. Accessed August 12, 2013

[30] Nagy Z, Takacs A, Filkorn T, Sarayba M. Initial clinical evaluation of an intraocular femtosecond laser in cataract surgery. J Refract Surg 2009; 25:1053–1060.

[31] Schultz T, Conrad-Hengerer I, Hengerer FH, Dick HB. Intraocular pressure variation during femtosecond laser–assisted cataract surgery using a fluid-filled interface. J Cataract Refract Surg 2013; 39:22–27

AD Publications
Sector-3, MP Nagar, Bikaner,
Rajasthan, India
www.adpublications.org, info@adpublications.org